European Commission

JRC SCIENTIFIC AND POLICY REPORTS

Radar Cross Section Measurements of Pedestrian Dummies and Humans in the 24/77 GHz Frequency Bands

Establishment of a Reference Library of RCS Signatures of Pedestrian Dummies in the Automotive Radar Bands

Joaquim Fortuny-Guasch
Jean-Marc Chareau

2013

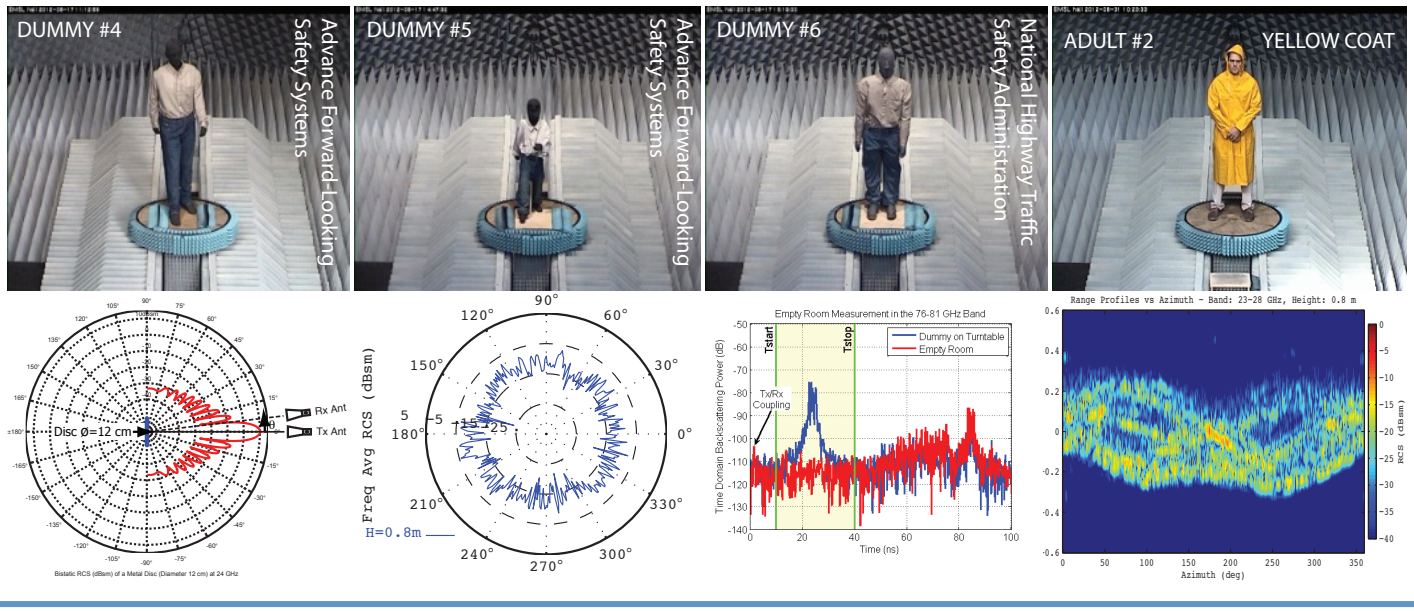

Report EUR 25762 EN

Joint Research Centre

European Commission
Joint Research Centre
Institute for the Protection and Security of the Citizen

Contact information
Joaquim Fortuny-Guasch
Address: Joint Research Centre, Via Enrico Fermi 2749, TP 723, 21027 Ispra (VA), Italy
E-mail: joaquim.fortuny@jrc.ec.europa.eu
Tel.: +39 0332 78 5104
Fax: +39 0332 78 5469

http://ipsc.jrc.ec.europa.eu/
http://www.jrc.ec.europa.eu/

JRC78619

EUR 25762 EN
ISBN 978-92-79-28230-0
ISSN 1831-9424
doi:10.2788/80844

Luxembourg: Publications Office of the European Union, 2013

Printed in Italy

Executive Summary

Road safety has become undoubtedly a major societal issue that needs to be addressed at the policy level. In a recent Communication[1], the Commission has underlined the importance of a European transport policy which should aim at ensuring sustainable mobility for all citizens, "decarbonising" transport and make full use of technological progress. Road safety already plays an important role in a recent White Paper on transport policy 2010–2020[2], as lowering the number of road users' casualties is key to improving the overall performance of the transport system and to meet citizens' and companies' needs and expectations.

In view of achieving the objective of creating a common road safety area, the Commission has proposed to continue with the target of halving the overall number of road deaths in the European Union by 2020 starting from 2010[3]. Achieving this target requires an integrated approach requiring a wide range of actions at different levels, where the protection of vulnerable road users has been identified as a highly relevant issue. The high number of fatalities and serious injuries faced by vulnerable road users such as riders of motorcycles, mopeds, cyclists and pedestrians are significant and in some European States are still increasing. In 2008, they represented 45% of all road deaths and statistics, which clearly shows that they have been given insufficient attention until now. However, at present, a wide range of new technologies, including intelligent speed adaptation and radar-based collision avoidance systems, are being widely deployed to improve road safety levels and reduce these casualties.

Automotive short-range radar (SRR) systems can constantly monitor the area around a vehicle to detect obstacles, such as other vehicles, pedestrians or static obstacles. They aim to warn drivers of potential collisions and alert them to pedestrians or obstacles in blind spots. Depending on the specific application, SRRs also have the potential to automatically trigger active safety measures, such as pre-tensioning of seat belts or automated braking to avoid or mitigate collisions. In recent years, the market penetration of automotive SRRs has been increasing quite rapidly because radar-based assistance functions, which were almost exclusively available in luxury cars, are currently stepping down towards the medium and compact car segments. Furthermore, a recent survey by the European New Car Assessment Programme (Euro NCAP) has decided to include autonomous emergency braking (AEB) systems (e.g., SRR sensors) as part of the overal Euro NCAP star rating from 2014 onwards. Two very important functions of AEB sensors are to detect other vehicles and, more importandly, to detect pedestrians, cyclists, motorcycles and other vulnerable road users.

The development of AEB sensors and also the need to assess quantitatively their detec-

[1] "Europe 2020 – A strategy for smart, sustainable and inclusive growth" COM(2010) 2020, March 2010, Communication from the Commission, Europe 2020.

[2] "Roadmap to a Single European Transport Area – Towards a competitive and resource efficient transport system", March 2011. Commission White Paper COM(2011) 144.

[3] "Towards a European road safety area: Policy orientations on road safety 2011-2020" (SEC(2010) 903), July 2010. European Commission – Communication from the Commission to the European Parliament, the Council, the European Economic and Social Committee and the Committee of the Regions.

tion performance has led to an increasing use of pedestrian dummies (i.e., test targets or surrogates mimicking pedestrians for the AEB sensors). Since a widespread use of these dummies is required to develop and test the AEB sensors, a clear need for harmonized test and evaluation procedures and standards has emerged recently. Today, the availability of SRR signatures of pedestrians, particularly in the 24 GHz and 77 GHz frequency bands, is very limited. The European Commission Joint Research Centre, in the framework of the FP7 ICT Project "More Safety for All by Radar Interference Mitigation" (MOSARIM), has conducted an extensive series of laboratory measurements aimed at establishing a reference library with the SRR signatures of a large collection of pedestrian dummies and a few adult humans in the 24 GHz and 77 GHz frequency bands. About a hundred RCS measurements took place during three entire weeks in August 2012, at the European Microwave Signature Laboratory (EMSL) of the JRC's Institute for the Protection and Security of the Citizen, located in Ispra, Italy. Key aspects such as the influence of the height of the SRR antennas above the ground, height of the dummies, and the effect of the clothing on the measured RCS signatures have been investigated.

A first analysis of the complete set of the various RCS signatures collected on all the pedestrian dummies and humans allows to draw the following qualitative assessments:

- For the first time, it has been proven that the observed global frequency/azimuth RCS averages in the two frequency bands are quite close and they do not show significant differences. This is an important finding given the fact that there is a current trend to manufacture almost exclusively SRR systems at the 77 and 79 GHz bands.
- A first analysis on the impact of the pedestrians' height on the measured RCS signatures has been completed. Results show that, particularly in the higher frequency bands, the height of the pedestrian has a clear effect on the RCS averages observed. In the case of the child dummies, for instance, the observed RCS at the lower antenna height (i.e., aligned with the center of mass of the dummy) was 6 dB above that observed at a position 0.5 m higher.
- A first qualitative comparison of the RCS signatures between dummies and humans was also completed. Results show that the RCS averages of the available dummies are slightly below those of the humans. It has also been observed that some of the dummies showed some peculiar dependence of the average RCS versus azimuth (e.g., a square shape with four clear corners), making them clearly distinguishable and different from all the other targets.
- A dedicated set of the measurements was designed to assess the impact of clothing on the measured RCS signatures. It was found that in most cases clothing did not impact significantly the RCS signatures observed. It was observed, as expected, that the impact is more evident in the high frequency band of 76–81 GHz, in particular, when some very thick clothes were worn.

Finally, it is important to note that a more exhaustive analysis of the data collected in this measurement campaign is currently being carried out. Subjects of interest that need to be

addressed more in detail include the definition of robust RCS signatures that can be used for classification purposes, and the identification of robust techniques to assess quantitatively the degree of similarity between two different targets.

Contents

List of Figures

List of Tables

List of Acronyms

AEB Autonomous Emergency Braking systems

ASPECSS ASsessment methodologies for forward looking integrated Pedestrian and further Extension to Cyclist Safety Systems EC ICT FP7

CEPT Conference of European Postal and Telecommunication Administrations

EC European Commission

ECC Electronic Communications Committee of the CEPT

EMSL European Microwave Signature Laboatory

ETSI European Telecommunications Standards Institute

EU European Union

FCC Federal Communications Commission

FFT Fast Fourier Transform

FP7 7th Framework Programme of the EC

GHz Giga Hertz

HEATCO Developing Harmonised European Approaches for Transport COsting EC FP6 Project

HH receive Horizontal transmit Horizontal polarization

ICT Information and Communications Technologies

ID Identification

IF Intermediate Frequency

IFFT Inverse Fast Fourier Transform

IIHS Insurance Institute for Highway Safety

ISAR Inverse Synthetic Aperture Radar

ISw Initial Swing

JRC European Commission Joint Research Centre

KIT Karlsruhe Institute of Technology

LO Local Oscillator

LRR Long Range Radar

MOSARIM MOre Safety for All by Radar Interference Mitigation EC ICT FP7 Project

MSw Medium Swing

NCAP New Car Assessment Programme

NHTSA National Highway Traffic Safety Administration

OECD Organisation for Economic Co-operation and Development

OEM Original Equipment Manufacturer

PNA Performance Network Analyzer

PVC Poly-Vinyl Chloride

RCS Radar Cross Section

RF Radio Frequency

Rx Receive

SARA Strategic Automotive Radar frequency Allocation group

SEM Singularity Expansion Method

SRR Short Range Radar

TSw Terminal Swing

Tx Transmit

USA United States of America

UWB Ultra-Wide Band

VV receive Vertical transmit Vertical polarization

1 Introduction

Road safety has become a major societal issue that should not be ignored. In 2009, more than 35,000 people died on the roads of the European Union, i.e. the equivalent of a medium town, and no fewer than 1,500,000 persons were injured. The associated costs for society are huge, representing approximately 130 billion Euro in 2009 [1]. A recent OECD Report has evaluated the global impact of these new technologies on road safety, providing recommendations to governments and industry [2]. A recent Communication of the European Commission stated that a wide deployment of SRR systems could help reach the EUs policy goal of halving the number of deaths on the road [3]. Achieving this target requires an integrated approach requiring a wide range of actions at different levels, where the protection of vulnerable road users has been identified as a highly relevant issue. The high number of fatalities and serious injuries faced by vulnerable road users such as riders of motorcycles, mopeds, cyclists and pedestrians are significant and in some European States are still increasing. In 2008, they represented 45% of all road deaths and statistics, which clearly shows that they have been given insufficient attention until now. However, at present, a wide range of new technologies, including intelligent speed adaptation and radar-based collision avoidance systems, are being widely deployed to improve road safety levels and reduce these casualties.

Automotive SRR systems can constantly monitor the area around a vehicle to detect obstacles, such as other vehicles, pedestrians or static obstacles. In fact, radars have been used since decades to measure accurately the distance and relative speed of the target being interrogated [4]. Today's SRR systems are similar to parking assistants but with a longer range. They aim to warn drivers of potential collisions and alert them to pedestrians or obstacles in blind spots. Depending on the specific application, SRRs also have the potential to automatically trigger active safety measures, such as pre-tensioning of seat belts or automated braking to avoid or mitigate collisions [5].

From a pure technology stand point, the main advantage of radar sensors compared to other alternatives such as video cameras, ultrasounds or lidar is its immunity to weather conditions, highly compact housing (i.e., particularly in the 77 GHz frequency band), and potential for low manufacturing costs [6, 7, 8]. In 2009, around 900,000 new 24 GHz SRR radars units have been installed in passenger cars in Europe, including both ultra-wide band (UWB) and narrow band radars. However, the 24 GHz UWB radars are subject to time-limited frequency regulations in Europe due to compatibility issues with radioastronomy, fixed and Earth exploration satellite services allocated in the same band [9, 10], which has led to a significant increase in the number of 24 GHz narrow-band radar sensors. Moreover, in the long term, the 24 GHz UWB sensor technology is planned to be replaced by 79 GHz sensors.

At present, the market penetration of automotive radars is increasing quite rapidly, in particular those operating in the 77 GHz and 79 GHz bands [11]. This is mainly because radar-based assistance functions, which were almost exclusively available in luxury cars, are currently stepping down towards the medium and compact car segments. An important

driver behind this trend in Europe is the fact that a recent survey by the European New Car Assessment Programme (Euro NCAP) has decided to include autonomous emergency braking (AEB) systems (e.g., a forward-looking radar) as part of the overal Euro NCAP star rating from 2014 onwards [12]. Two very important functions of AEB sensors are to detect other vehicles and, more importandly, to detect pedestrians, cyclists, motorcycles and other vulnerable road users. The development of AEB sensors and also the need to assess quantitatively their detection performance has led to an increasing use of pedestrian dummies (i.e., test targets or surrogates mimicking pedestrians for the AEB sensors). Since a widespread use of these dummies is required to develop and test the AEB sensors, a clear need for harmonized test and evaluation procedures and standards has emerged recently.

In this context, it is very important to make sure that the SRR signatures of pedestrian dummies match those of humans with a high degree of accuracy. However, the availability of this kind of test targets is rather new and, consequently, there is a limited knowledge on the radar signatures they show, particularly in the 24 GHz and 77 GHz frequency bands [13]. The available radar signatures of humans are in the USA FCC UWB band (i.e., 3.1–10.6 GHz) [14] and in the mm-Wave bands above 100 GHz. As an example, one of the key aspect in the tests of SRR sensors is to prove that a pedestrian is detected at a certain distance, which requires the definition of a threshold or minimum radar cross section (RCS) the radar must be able to measure. Therefore it is extremely important to have precise estimates of the typical RCS values of pedestrians and, more precisely, of pedestrian dummies that are required in the tests of AEB sensors.

This report presents the results of an extensive series of RCS laboratory measurements on pedestrian dummies and humans. The measurements took place in August 2012, at the European Microwave Signature Laboratory (EMSL) [15] of the European Commission Joint Research Centre, Ispra, Italy. This measurement campaign was carried out in the context of the EC FP7 ICT Project MOSARIM [16] and was aimed at establishing a reference library with the RCS signatures of pedestrian dummies and humans in the 24 GHz and 77 GHz bands. To this end, issues such as the influence of the height of the SRR antennas above the ground, height of the dummies, and the effect of the clothing on the measured RCS signatures are investigated. The definition of a proper metric that could be used to quantify the degree of similarity between two RCS signatures is also addressed and some examples are given.

This report is organized as follows. A description of the measurement set-up and, including a detailed description of the test set-up, the control software, the frequency bands selected for the tests, the calibration procedure and an assessment of the test set-up repeatibility are given given in Section 2. Section 3 includes a complete description of the RCS signatures selected to characterize the pedestrians, and a discussion on the results that have been obtained in this campaign, along with some key parameters that influence the characteristics of the RCS signatures. Finally, the conclusions drawn from the analysis of the measurement results are summarized in Section 4.

2 Measurement Set-up

All the radar cross section (RCS) measurements subject of this report were performed in the anechoic chamber of the European Microwave Signature Laboratory (EMSL). This chamber has a hemispherical shape with a diameter of 20 m and a height of 15 m, and is equipped with a computer-controlled 5 ton capacity turntable mounted on a movable platform that can be brought in and out for load/unload operations, as shown in Figure 1. The goal of the measurement campaign was twofold: firstly, to collect the RCS signatures of pedestrian dummies in the SRR frequency bands at 24/77 GHz, and secondly, to assess their similarity with the RCS signatures of humans. It is important to note that pedestrian dummies are not exclusively designed for the testing of SRR systems, and they are also used to test other automotive forward looking safety systems such as infrared cameras. The dummies were placed on the computer-controlled turntable of the anechoic chamber. A stepper motor with very high step accuracy and resolution (i.e., both below 0.01°) controlled the rotation axis position of the turntable. For safety reasons, the height of the target holder inside the chamber was lowered down to a position 1 m above the ground. The turntable could be rotated from 0 to 360°, and brought outside the chamber when the dummy had to be replaced. Some of the dummies had to be suspended with a thin Nylon rope attached to the chamber ceiling to have them standing stably during the tests. The control of the instruments and the rotation axis of the turntable were performed remotely from the laboratory control room. A view of the anechoic chamber with a dummy under test standing on the turntable and the instrumentation installed inside the chamber is shown in Figure 2.

The RCS measurements were performed in the bands 23–28 GHz and 76–81 GHz simultaneously using two Vector Network Analyzers with a common trigger input signal. The two network analyzers were installed inside the anechoic chamber, with the antennas and

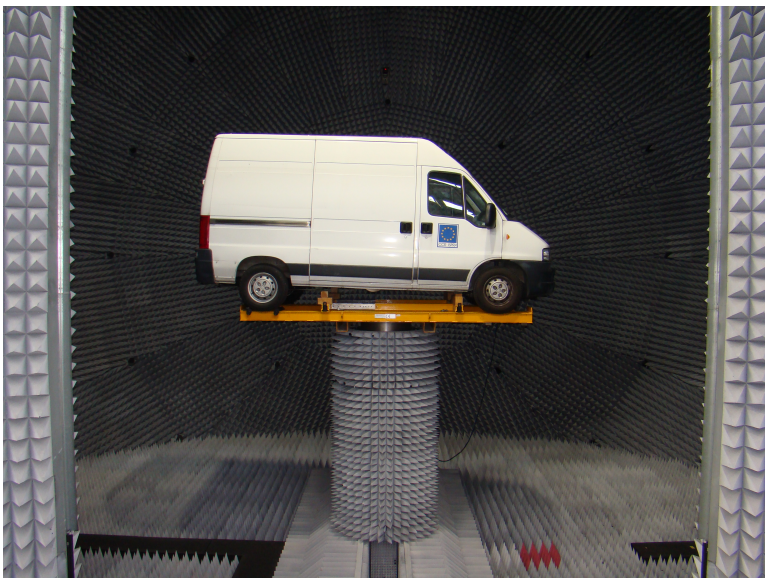

Figure 1: View of the anechoic chamber showing a van loaded on the computer-controlled turntable.

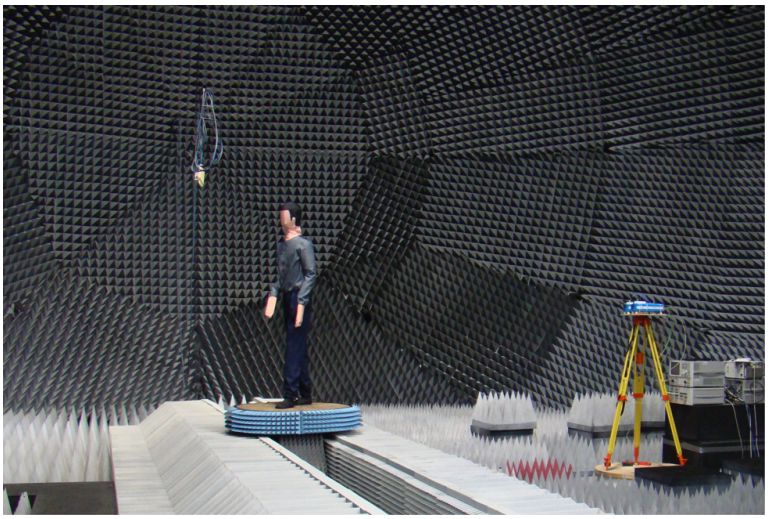

Figure 2: View of the test setup inside the anechoic chamber of the EMSL.

millimeter wave extension heads being mounted on a tripod with adjustable height, as shown in Figure 3. One can distinguish the two horn antennas in the E-band (60–90 GHz) attached to the mm-Wave extension heads (i.e., the blue boxes) and the Ka-band (26.5–40 GHz) horn antennas mounted on top. A quasi-monostatic configuration was used, with Tx and Rx antennas colocated along the horizontal cross-range axis. The horizontal separation between the two sets of Tx/Rx antennas was 15 cm. The range distance between the antenna apertures to rotation axis of the turntable was 3.4 m. The gain of the antennas in the 24 GHz and 77 GHz frequency bands was in both cases approximately 20 dB. The half-power beamwidth in the E-plane (i.e., the vertical plane) for both sets of Tx/Rx antennas was about 20°, which is basically enough to guarantee a quasi-uniform illumination of a pedestrian or human standing on the turntable, as illustrated in Figure 3. The polarization was vertical both for Tx and Rx antennas, simply because that is the polarization currently used by automotive SRRs. The laboratory equipment used for the RCS measurements subject of this report is summarized in Table 1.

2.1 Millimeter-Wave Frequency Extension

The solution adopted to carry out the measurements in the 77 GHz band has been to use a vector network analyzer in combination with a frequency extension for the E-Band, both from Agilent Technologies [17]. The frequency extension for the Vector Network Analyzer PNA-X consists of a millimeter wave controller and two millimeter wave heads. The controller provides the RF and local oscillator (LO) signals to the millimeter wave heads and receives the IF of the reference and test channels. The block diagram of an Agilent N5256 mm-wave extension head that can operate alternatively in the Tx or Rx modes is shown in Figure 4. In Tx mode, the frequency of the RF input signal in the band 10 to 15 GHz is multiplied by a factor 6 using an active frequency doubler followed by a tripler. The waveguide output of the tripler in the band 60 to 90 GHz feeds the Tx antenna connected to the test port through

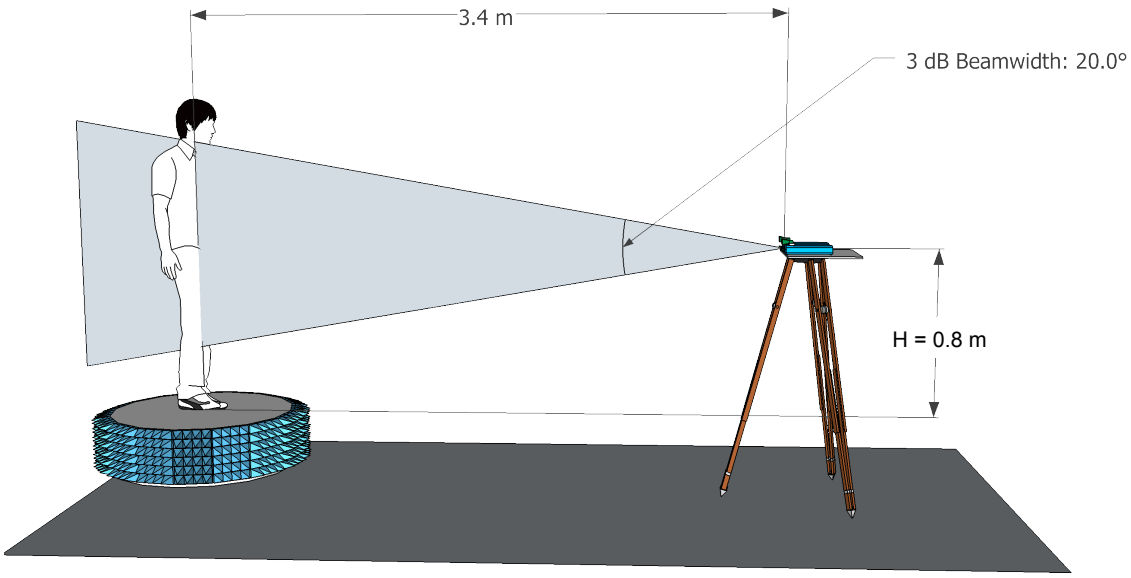

(a)

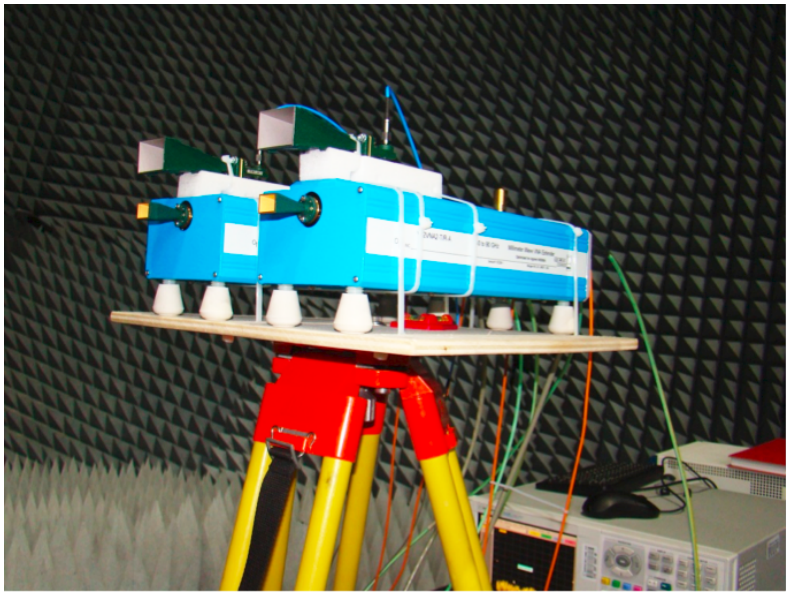

(b)

Figure 3: (a): Sketch showing the measurement set-up used in the RCS measurements (left); (b) Close view of the mm-Wave frequency extension heads and the two sets of Tx/Rx antennas at 24 (upper) and 77 GHz (lower).

23–28 GHz Frequency Band

Description	Model	Manufacturer
Network Analyzer	E8364B	Agilent Technologies
Std Gain Horn	22240-20	Flann Microwave
Coax-to-Waveguide Adaptors	22093-KF 20	Flann Microwave

76–81 GHz Frequency Band

Description	Model	Manufacturer
Network Analyzer	N5247A	Agilent Technologies
Millimeter Wave Controller	N5262A	Agilent Technologies
E-Band T/R mm-Wave heads	N5256AW12	Agilent Technologies
Std Gain Horn	26240-20	Flann Microwave

Table 1: Summary of the laboratory equipment used for the RCS measurements in the 24 GHz and 77 GHz frequency bands.

a directional coupler, with one part of the signal going to the reference channel mixer. In Rx mode, the RF input is absent. The wave received by the antenna connected to the test port is routed to the test channel mixer using a directional coupler. This mixer works at the 5*th* harmonic of the LO frequency, which is in the 12 to 18 GHz band to produce a fixed intermediate frequency (IF).

2.2 Control Software

A measurement control software written in Microsoft Visual C# .NET was used to control the rotation of the turntable and acquire the RCS data from the vector network analyzer working at 77 GHz at every aspect angle of a given measurement scenario. Since a simultaneous acquisition of the backscattering data in two frequency bands was needed, a second stand-alone measurement control software was developed to acquire the backscattering data in the 24 GHz frequency band, this time using a National Instruments Labview Script. The solution that was adopted to synchronize the two measurements was to configure the PNA-X, which was doing the measurements at 77 GHz, such that it was giving a trigger signal to the second PNA at the start of every frequency sweep. The swept times (i.e., the IF bandwidth) of the two measurements were configured such that the measurement in the 77 GHz band finished slightly after that in the 24 GHz band. A flowchart of the control and acquisition software is shown in Figure 5. The left part of the chart represents the main steps of a standard EMSL measurement cycle. After initialization, the program enters in a loop in which the angular position is set, the 76–81 GHz frequency sweep is started and the RCS data is streamed to the hard disk in binary format.

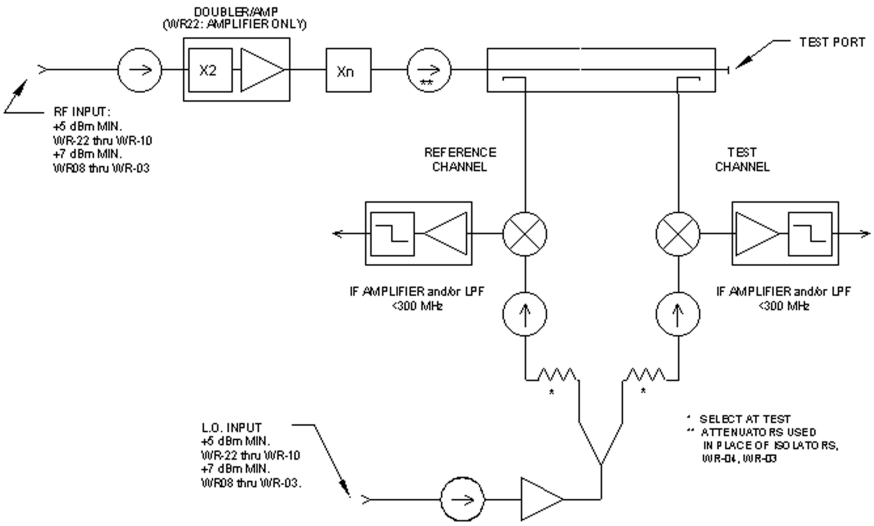

Source: Agilent Technologies N5256/7/8A Millimeter-wave Modules Users Guide [17]

Figure 4: Block diagram of the mm-Wave frequency extension heads for the E-Band RCS measurements.

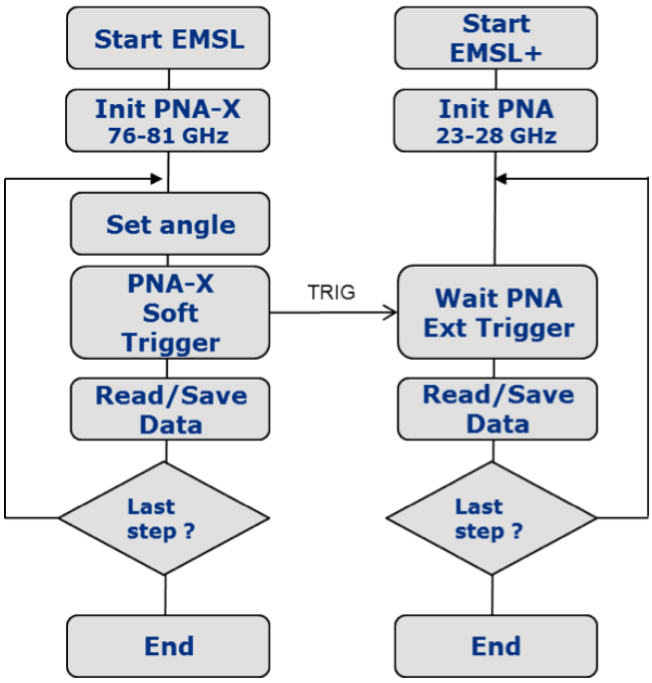

Figure 5: Flowchart of EMSL measurement control software with an extension for two simultaneous RCS measurements.

2.3 Frequency Bands for Automotive Radar

The choice of the frequency bands used in the RCS measurements was made in accordance to the current status of the European spectrum regulation for automotive radar. The first regulatory decisions on the 24 GHz band for short range automotive radars started in 2002. A Consortium formed by more than 30 car manufacturers and OEM suppliers was created (i.e., the SARA Group) to support the UWB regulation for automotive radar in the 24 GHz band in Europe. In 2005, a Commission Decision was adopted and the 21.65–26.65 GHz band was allocated for UWB SRRs. Recently, authorisation to use the 24 GHz frequency band for anti-collision SRR in cars has been extended until 2018 by a European Commission Decision [18]. This temporary extension will ensure that SRR systems remain available on the market until manufacturers develop technology using the 79 GHz band.

The choice of the two frequency bands of the RCS measurements was as follows. The horn antennas used in the 24 GHz band were designed for operation in the Ka band (26.5–40 GHz). Since the waveguide cutoff frequency of the flange was about 21 GHz, the center frequency of the RCS measurements at 24 GHz was slighly shifted up and the 23–28 GHz band was finally used.

Regarding the E-band frequency allocation, the band range 76–77 GHz was allocated to long range automotive radars (LRR) in 2002, following the CEPT Electronic Communications Commitee Decision ECC/DEC/(02)01. This Decision led subsequently to a European Standard for automotive radars [19]. In 2004, the frequency band 77–81 GHz was allocated to automotive SRR, following the Commission Decision 2004/545/EC [20, 21]. Bearing these two regulatory decisions in mind, the frequency band chosen for the present study on the RCS measurements of pedestrian dummies was finally 76–81 GHz.

Having a bandwidth of 5 GHz in the two RCS measurement bands provided an extremely high range resolution in the time domain (i.e., $\Delta R \simeq 3$ cm), which means that one can apply time gating techniques to isolate the backcatter from the target and effectively remove unwanted contributions such as the Tx/Rx coupling, noise and background clutter. A vector network analyzer can be programmed to acquire the complex backscattering data in the frequency domain at a selected number of uniformly spaced frequency points. The network analyzer in this case becomes a stepped frequency radar [22, 23]. A range profile of the radar backscatter can be simply obtained through a Fourier transform of the frequency domain backscatter data. The number of frequency points used in the measurements was 2001 in the two bands. This resulted in an unambiguous range of about 60 m, which was far beyond the dimensions of the anechoic chamber. The choice of the bandwidth of the intermediate frequency (IF) filter directly affects the signal-to-noise ratio of the measurement, leading to a trade-off between the sweep time and the measurement uncertainty. Short measurement sweeps are needed in order to be able to collect RCS signatures of humans standing on a turntable. On the other hand, sweep times should not be too short since this would increase significantly the uncertainty and noise in the measurement. Bearing this in mind, and after a series of laboratory tests, it was decided to set the IF bandwidth in the 24 GHz and 77 GHz bands to, respectively, 15 and 10 kHz. This choice represents a rea-

Parameter	Frequency Band	
	24 GHz	**77 GHz**
Start Frequency (GHz):	23.0	76.0
Stop Frequency (GHz):	28.0	81.0
IF Bandwidth (kHz):	15.0	10.0
Sweep Time (ms):	200.0	250.0
Number of Frequency Points:	2001	2001
Acquired Traces:	A/R1 and B/R1	A/R1

Table 2: Summary of the settings programmed on the two vector network analyzers in the 24/77 GHz frequency bands.

sonable compromise that guarantees a high accuracy of the RCS measurements on both pedestrian dummies and humans. A summary of the settings that were programmed on the two vector network analyzers is given in Table 2.

2.4 RCS Data Calibration

The raw RCS backscatter data collected in the two frequency bands are not calibrated and include unwanted terms such as the Tx/Rx direct coupling, Tx/Rx antenna gains, cable losses, free-space propagation losses, and the possible impedance mismatch and insertion loss at the various connectors and waveguide flanges in the RF chain. Therefore, an additional measurement using a reference or canonical target with known RCS in the frequency range of the measurement is needed to calibrate the backscatter data and obtain a precise estimate of the RCS [24, 25]. The target RCS as a function of the frequency is the exclusive characteristic signature of interest in these measurements.

Since just a single polarization was used in all measurements (i.e., VV), a single reference target with known RCS in this polarization is needed. In indoor RCS measurements, in addition to the calibration measurement, it is common to apply a background substraction or empty room measurement. This is an additional measurement made exactly under the same conditions as the RCS measurements but with no target present on the turntable. The set-up used in the measurements was designed to ensure an extremely low RCS within the range window enclosing the turntable. This was largely achieved and the measured average power of the empty room measurement was at least 35 dB below that of the target that was being characterized, which means that a background substraction was not needed. An example range profile of the backscattered power measured both with and without a dummy present on the turntable is shown in Figure 6. These range profiles have been obtained prior to the calibration and therefore the round trip travel times from the Tx/Rx antennas to the turntable (i.e., region coloured in light yellow) in the two frequency bands are different. Anyway, it can be clearly seen that the peak RCS of the dummy is significantly higher than the average RCS of the empty room backscatter within the region occupied by the turntable. More specifically, the peak RCS of the dummy is about 45 dB and 35 dB above that of the average background RCS, respectively, in the 24 and 77 GHz frequency bands. The

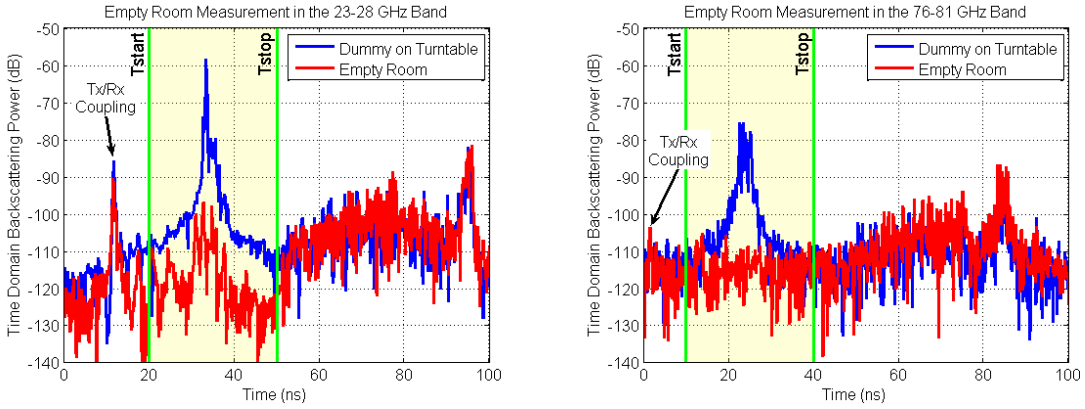

(a) **(b)**

Figure 6: Range profiles of the backscattered power measured both with and without a dummy present on the turntable in the 23–28 GHz (left) and 76–81 GHz (right) frequency bands.

background noise in the 77 GHz measurements was slightly higher because of the E-band frequency extension, which has some active elements that raise the noise floor of the receiver. It must also be noted that the direct coupling between the Tx and Rx antennas is present in both range profiles and is effectively filtered out after a time gating. The coupling level observed in the 77 GHz band is significantly lower than that in the 24 GHz band. This is because in both bands the separation distance between the Tx and Rx antennas was exactly the same and the sidelobes of the horn antennas at 77 GHz were significantly lower.

The calibration of the measurement data has been carried out in four steps, namely. Firstly, a one-dimensional inverse FFT along frequency is applied to get the time domain backscatter data. Secondly, a time gating is applied to filter out the backscatter falling outside the region of interest centered at the turntable time bin. Thirdly, a one-dimensional FFT along the time dimension to get the gated frequency domain backscatter data. Fourthly, a frequency domain calibration of the backscatter data using the theoretical and measured backscatter from a canonical target located at the center of the turntable. A mathematical expression that formulates the calibration technique that has been used can be given as follows:

$$\mathrm{S_{cal}[f,\phi]} = \frac{\mathrm{C_{theo}[f]}}{\mathrm{C_{msr}[f]}} \times \int_{\mathrm{T_{start}}}^{\mathrm{T_{stop}}} \left\{ \int_{\mathrm{F_{start}}}^{\mathrm{F_{stop}}} \mathrm{S_{uncal}[f,t]} \exp\left[+\mathrm{j}\frac{2\pi \mathrm{ft}}{\mathrm{c}}\right] \mathrm{df} \right\} \exp\left[-\mathrm{j}\frac{2\pi \mathrm{ft}}{\mathrm{c}}\right] \mathrm{dt} \quad (1)$$

where $C_{\mathrm{theo}}[f]$ and $C_{\mathrm{msr}}[f]$ denote, respectively, the theoretical and actually measured backscatter from a reference target as a function of the frequency, $S_{\mathrm{uncal}}[f,\phi]$ denotes the frequency domain raw data to be calibrated, F_{start} and F_{stop} are the start and stop frequencies of the RCS measurement, T_{start} and T_{stop} are the start and stop times enclosing the region occupied by the turntable, c is the speed of light, f is the RF frequency variable, and t denotes the time variable.

The coding of the calibration given in Eq. (1) using a mathematical toolkit such as Matlab is straightforward. First, the equation has to be re-written in discrete form based on the fact that the radar backscatter was measured at a set of frequency and azimuth aspect angles

both uniformly spaced. Then, the two integrals in Eq. (1) shall be calculated using FFT codes, which reduces drastically the computational cost. In fact, the calibration basically reduces a sequence of an inverse FFT followed by an FFT and a complex product. Thus, Eq. (1) in discrete form can be written as follows:

$$\mathrm{S_{cal}[f_n, \phi_m]} = \frac{\mathrm{C_{theo}[f_n]}}{\mathrm{C_{msr}[f_n]}} \times \mathbf{FFT}_{\mathrm{time}}[\mathrm{W_t^n}\ \mathbf{IFFT}_{\mathrm{freq}}[\mathrm{S_{uncal}[f_n, \phi_m]}]] \tag{2}$$

where $n = 0, \ldots, N_f - 1$ denotes the index of the frequency sweep, $m = 0, \ldots, M_\phi - 1$ is the index of the 360° azimuth scan of the turntable, W_t^n is a time gating weighting function that is null at all the time bins except those within the time window $[T_{\mathrm{start}}, T_{\mathrm{stop}}]$, where it equals one.

The measurement set-up used for the calibration of the RCS data using a metal sphere is shown in Figure 7. The calibration was performed in two steps. A first coarse calibration was achieved using a conducting circular disc of 12 cm diameter precisely located at the center of the turntable. The disc was carefully aligned pointing towards the middle point of a line segment between the Tx and Rx antennas using a laser distometer. A planar surface such as a disc has the advantage of showing a very high RCS that increases steadily as the frequency increases. However, at the frequencies used in the measurements, a disc of 12 cm shows a very high directivity and it is practically not possible to have a precise simultaneous aligment with the two sets of Tx/Rx antennas because of the small height separation distance (i.e., about 7 cm). Still, the use of a small circular disc is useful to get a precise calibration of the phase of the backscatter data using a reference target with very high RCS. The effect of the small misalignment will be that the calibration will introduce a slight amplitude offset that can be corrected using a second reference target not requiring a careful alignment. In this case, a metallic sphere of diameter 3 in was used to estimate the amplitude offset and calibrate the RCS accordingly. A metal sphere shows the nice property of having a rather constant RCS for small bistatic angles that can be easily predicted using the Mie's solution, as described in Appendix A. In the set-up used in the RCS measurements, the bistatic angle was approximately 2.5°.

The first calibration with the circular disc was made using the theoretical RCS response for normal incidence, which can be simply expressed as follows [26]:

$$\sigma_{\mathrm{disc}}(f) = \frac{4\,\pi\,A^2 f^2}{c^2} \tag{3}$$

where A denotes the physical area of the circular disc and λ is the wavelength at the frequency of the measurement. The theoretical complex backscattering that needs to be used in Eq. (1) is:

$$C_{\mathrm{theo}}^{\mathrm{disc}}(f) = \frac{j2\sqrt{\pi}A\,f}{c} \tag{4}$$

The precise magnitude of the amplitude offsets that may be introduced when using a circular disc as the reference target has been estimated using a second calibration measurement with a metal sphere of 3 in diameter. The results of this second calibration measurement are shown in Figure 8. The estimated amplitude offsets to be added to the RCS data calibrated using the circular disc were 1.41 dB and 2.70 dB, respectively, in the 24 GHz and

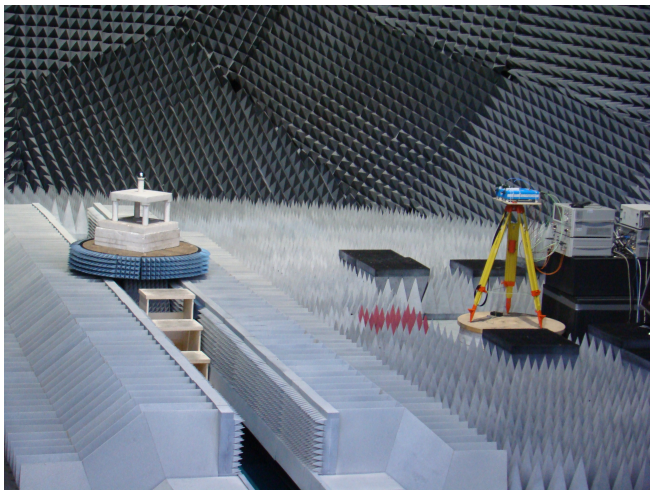

Figure 7: Laboratory setup with the calibration sphere mounted on the turntable at a distance of 3.4 m from the radar antennas.

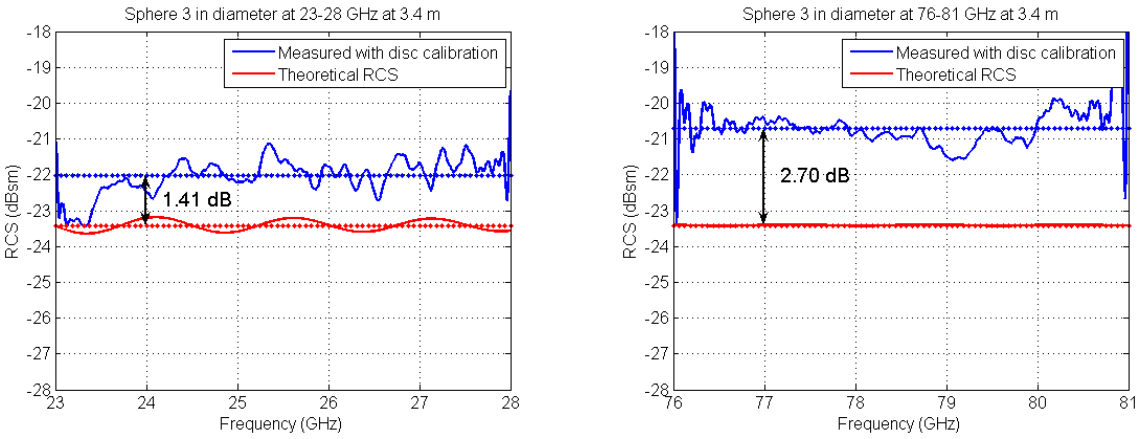

(a) **(b)**

Figure 8: Results of the calibration measurements using a metal sphere to estimate the amplitude offsets in the 24 GHz (left) and 77 GHz (right) frequency bands.

77 GHz frequency bands. The rms error after the compensation of the amplitude offsets in the measurement of the calibration sphere in these two bands were 0.41 dB and 0.38 dB. This result is considered to be good enough and the proposed two-steps calibration using the metal disc and the compensation for the amplitude offsets will be used in all the RCS measurements subject of this report.

2.5 Test Setup Repeatibility

The repeatibility of the test setup used in the RCS measurements was assessed in two different conditions. First, the short-term repeatibility was estimated by conducting two consecutive measurements on the very same pedestrian dummy. In this repeatibility test, the second measurement was carried out right after the first one without touching the dummy on

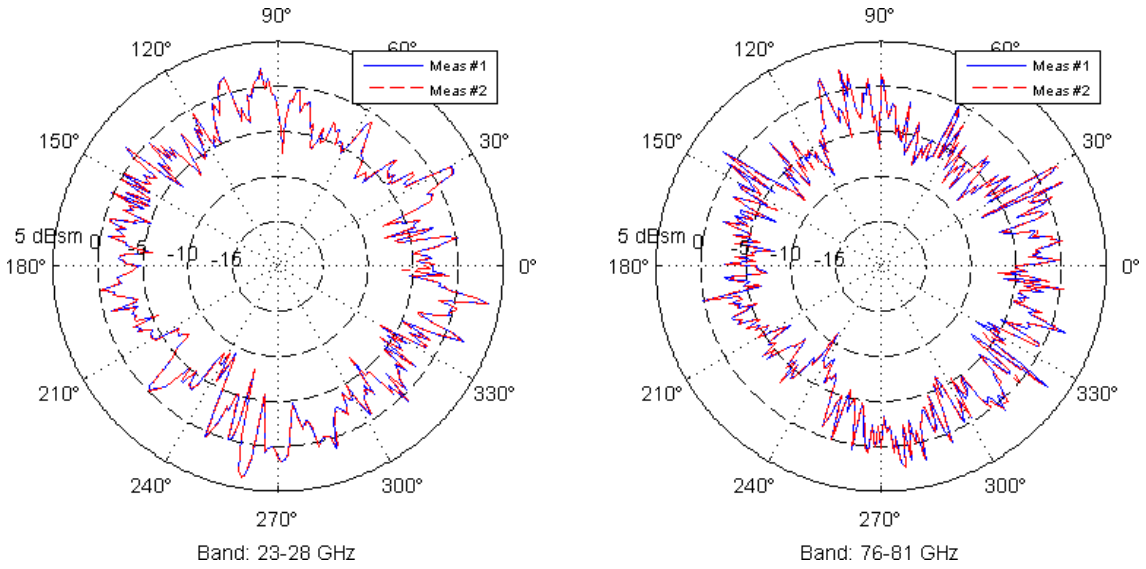

Figure 9: Results of the short term repeatibility measurement at the 24 (left) and 77 GHz (right) frequency bands.

the turntable. The backscatter data was collected in two frequency bands 23–28 GHz and 76–81 GHz, at a total of 360 azimuth positions spaced 1 deg, just as in all the other tests on the pedestrian dummies. A possible way to assess the repeatibility of the measurement is, for instance, to compare the polar plots of the frequency average of the measured RCS as a function of the azimuth rotation angle, which in discrete form can be expressed as:

$$\sigma_{\text{avg}}^{\text{freq}}[\phi_m] = \frac{1}{N_f} \sum_{n=0}^{N_f-1} |S[f_n, \phi_m]|^2 \tag{5}$$

where $S[f_n, \phi_m]$, as defined in Eq. (2), denotes the calibrated backscatter data of the dummy under test, as a function of the frequency and azimuth position of the turntable.

The result of this comparison for the two frequency bands measured is shown in Figure 9. It can be observed that the RCS values from the two consecutive measurements are almost indistinguishable. This confirms a very high short term repeatibility and stability of the entire test setup, which is an important requirement for the long series of RCS measurements subject of this report.

Similarly, an assessment of the long term repeatibility of the setup was completed. This test consisted of two measurements on the very same dummy carried out three days apart. After the first measurement, the turntable was brought out of the anechoic chamber and the dummy was removed. In between the two measurements, a series of other tests on various dummies was completed. The dummy used in the first measurement was placed back on the turntable and a second RCS measurement was completed. The comparison of the results of these two measurements is shown in Figure 10. It can be seen that the observed differences are minimal, particularly taking into account the fact that the precise position of the dummy was not exactly the same in the two tests. The overall agreement is

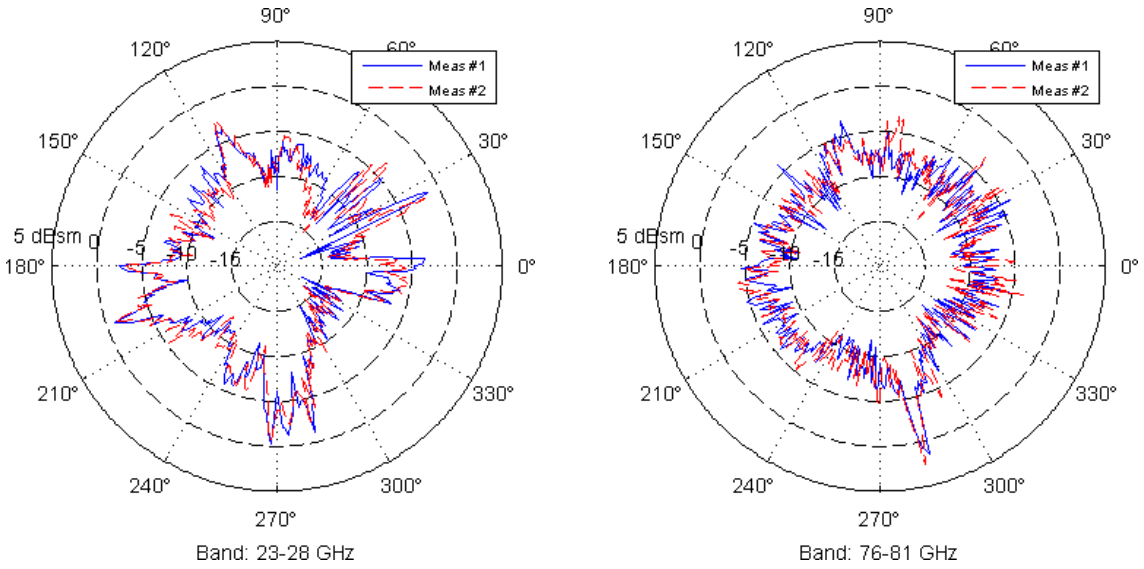

(a) **(b)**

Figure 10: Results of the long term repeatibility measurement at the 24 (left) and 77 GHz (right) frequency bands.

good enough and shows that the procedure to mount and remount the dummy guarantees a reasonable repeatibility.

3 RCS Measurement Results

In collaboration with members of the ASPECSS (Assessment methodologies for forward looking Integrated Pedestrian and further extension to cyclist safety systems) EC FP7 Project Consortium [27], a representative selection of pedestrian dummies was made. Among the various activities organized within the framework of the ASPECSS project, a series of measurement campaigns requiring a representative selection of pedestrian dummies has been planned. Therefore, it was agreed to share use as much as possible of the very same dummies in both measurement campaigns. As a result, a total of 11 pedestrian dummies were kindly made available for this measurement campaign during August 2012. The complete list of the dummies, along with its identification names and the provider/manufacturer is shown in Table 3. The precise details on the material composition of the dummies were not made available and, consequently, cannot be provided in the present report.

In addition to the RCS measurements on pedestrian dummies, a series of tests collecting the RCS of humans under the same conditions was also carried out. The purpose of these additional measurements was twofold. Firstly, for comparison purposes, to assess the degree of similarity between the typical RCS signatures of pedestrian dummies and those of real humans. Secondly, to investigate the impact of different types of clothing on the measured RCS in the two frequency bands, respectively, at 24 and 77 GHz.

ID #	Identification Name	Dummy Provider/Manufacturer
1	KIT Dummy	Karlsruhe Institute of Technology, Germany
2	4a Dummy	4a engineering GmbH, Austria
3	Audi Bicycle and 4a Dummy	Audi AG, Germany / 4a engineering GmbH, Austria
4	vFSS Adult Dummy	Advance Forward-Looking Safety Systems, Germany
5	vFSS Child Dummy	Advance Forward-Looking Safety Systems, Germany
6	NHTSA Adult Dummy	National Highway Traffic Safety Administration, USA
7	NHTSA Child Dummy	National Highway Traffic Safety Administration, USA
8	TRL/innovITS Advance Adult Dummy	Transport Research Laboratory, United Kingdom
9	TRL/innovITS Advance Child Dummy	Transport Research Laboratory, United Kingdom
10	IDIADA Dummy	Applus IDIADA Group, Spain
11	IIHS Dummy	Insurance Institute for Highway Safety, USA

Table 3: List of pedestrian dummies used in the RCS measurement campaign.

3.1 RCS Signatures

Establishing the degree of similarity among different types of pedestrian dummies or between humans and pedestrian dummies is not a trivial task. The collected backscatter datasets are multi-dimensional and as such they can be treated in many different forms. One could use, for instance, the radar backscatter in the time domain and try to classify the target based on its late time response using the so-called singularity expansion method (SEM) [28, 29]. The RCS measurements subject of this report have been carried out using a very wide frequency bandwidth (i.e., 5 GHz), which provides a very high resolution in the time domain. The SEM technique exploits the fact that late time response of a given target can be modelled as a sum of exponentially decaying sinusoids. Under the assumption that the late time response is an exclusive characteristic signature of the target, the loci of the associated complex frequency poles of this sum of sinusoids has been used to classify the targets. Alternatively, one could also use the time domain backscatter as a function of the aspect angle or azimuth position of the turntable, also known as the B-scan or sinogram, as the key characteristic signature to classify the targets. In some cases, targets can be modelled as an ensamble of point-like scatterers that are clearly distinguisable in the range profile. As the target rotates through the 360°, the loci of these point scatterers in the B-scan determines a characteristic pattern that can also be used for classification purposes. This feature could be further exploited if the RCS measurement is made with a sufficiently fine angular sampling such that:

$$\Delta\phi_{\min} \leq \frac{\lambda_c}{2\ D_{\max}} \tag{6}$$

where λ_c denotes the wavelength at the center frequency and $D_{\max}$ is the diameter of the smallest cylinder enclosing completely the target under test. Collecting the frequency domain backscatter using an angular sampling satisfying Eq. (6), allows the formation of a radar image using inverse synthetic aperture radar (ISAR) techniques [23, 30]. The spatial resolution of ISAR images can be extremely high, i.e., with $\Delta x = \Delta y \simeq \lambda_c/5$ in the case of an azimuth aperture synthesis spanning 360° [31].

Another interesting alternative to classify and compare quantitatively the RCS signatures of pedestrians is based on the micro-Doppler signatures, which are particularly useful when there is a relative movement between the SRR and the pedestrian being characterized [32]. The use of the micro-Doppler and time-frequency signatures has been suggested to classify pedestrians and effectively extract characteristic features of their gait [33, 34, 35].

Finally, it is worth mentioning that in addition to the above feature extraction techniques, one could also attempt to classify the pedestrians RCS signatures from an statistical viewpoint. For instance, the probability density function of the frequency-domain RCS at each azimuth position of the turntable is expected to show some characteristic features. Thereby, pedestrians may be classified based on the boxplots of the RCS as a function of the aspect angle [36, 13]. However, this statistics-based classification technique does not exploit the information present in the phase of the frequency-domain backscatter data, which might pose some limitations in certain cases.

The main objective of the present report is to present a wide range of typical RCS sig-

natures of pedestrians measured in the two SRR frequency bands at 24 and 77 GHz. However, an in-depth study on the suitability of the characteristic signatures that can be extracted from the data collected in this measurement campaign falls beyond the scope of this report. Therefore, in the present report, three main classes of signatures are suggested to characterize the pedestrians (i.e., both the pedestrian dummies and humans) will be used. A brief description of these three signatures is next.

3.1.1 Frequency average RCS versus azimuth

The calibrated backscatter data defined in Eq. (2) can be averaged within a given sub-band within the measured frequency band. Noting that the frequency span of the RCS measurements both at 24 and 77 GHz was 5 GHz, it has been decided to split both frequency bands into five sub-bands spanning 1 GHz each. Then, one can define the following six frequency averages of the backscatter RCS versus azimuth and use them as the characteristic signatures of a given pedestrian. The frequency average of the backscatter RCS can be expressed as follows:

$$\mathrm{RCS}_{\mathrm{iband}}^{\phi-\mathrm{avg}}[\phi] = \frac{1}{\mathrm{B}_{\mathrm{avg}}} \int_{\mathrm{f}_{\mathrm{istart}}}^{\mathrm{f}_{\mathrm{istop}}} |\mathrm{S}_{\mathrm{cal}}[\mathrm{f}, \phi]|^2 \, \mathrm{df} \tag{7}$$

where B_{avg} is 1 GHz, and $f_{\mathrm{istart}}/f_{\mathrm{istop}}$ denote the start/stop frequencies of the i*th* sub-band, which have been defined as shown in Table 4. A sub-band spanning the entire measured

	Frequency Band			
	24 GHz		**77 GHz**	
Sub-band	**Start Freq (GHz)**	**Stop Freq (GHz)**	**Start Freq (GHz)**	**Stop Freq (GHz)**
1st	23.0	24.0	76.0	77.0
2nd	24.0	25.0	77.0	76.0
3rd	25.0	26.0	78.0	79.0
4th	26.0	27.0	79.0	80.0
5th	27.0	28.0	80.0	81.0
6th	23.0	28.0	76.0	81.0

Table 4: Start and stop frequencies of the six frequency sub-bands used average the backscatter RCS versus the azimuth angle.

frequency range of 5 GHz has been defined in view of the fact that some of the planned SRR radars in the 77 GHz band may occupy such a wide portion of spectrum. An example of the polar plots of the average backscatter RCS in the six sub-bands that have been defined is shown in Figure 11. The frequency band of these example polar plots is 23–28 GHz. The target under test was the dummy #1 (i.e., KIT dummy). Four snapshots of this dummy on the turntable corresponding to the front, rear, left, and right azimuth positions are also shown. In this example, the radar antennas height above the turntable was 0.8 m.

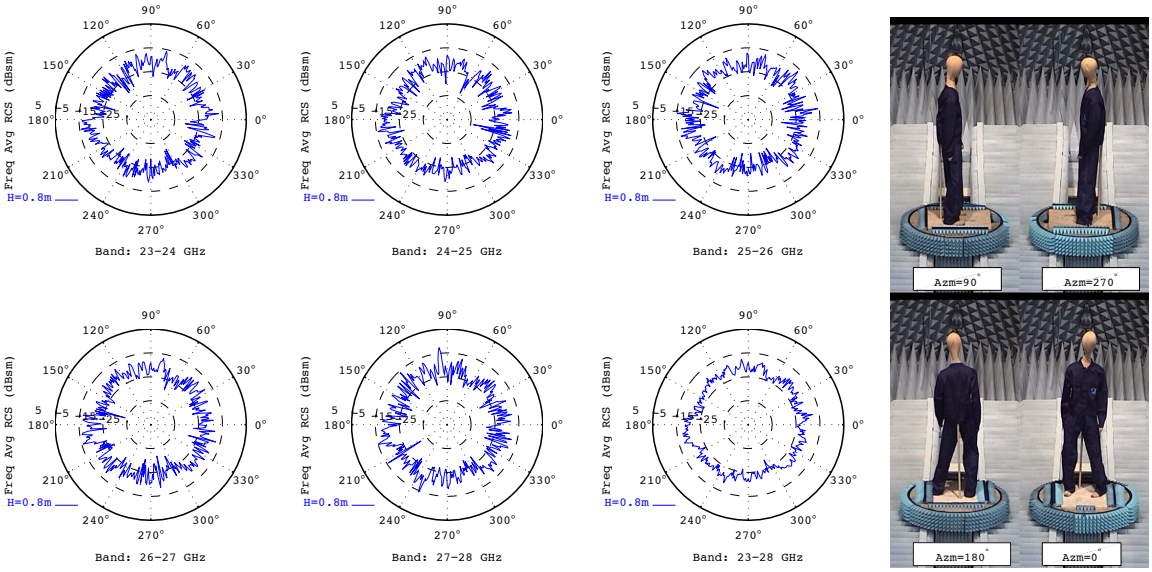

Figure 11: Example polar plots of the average backscatter RCS in the six sub-bands in the 23–28 GHz frequency range (left), and four snapshots of the dummy #1 on the turntable.

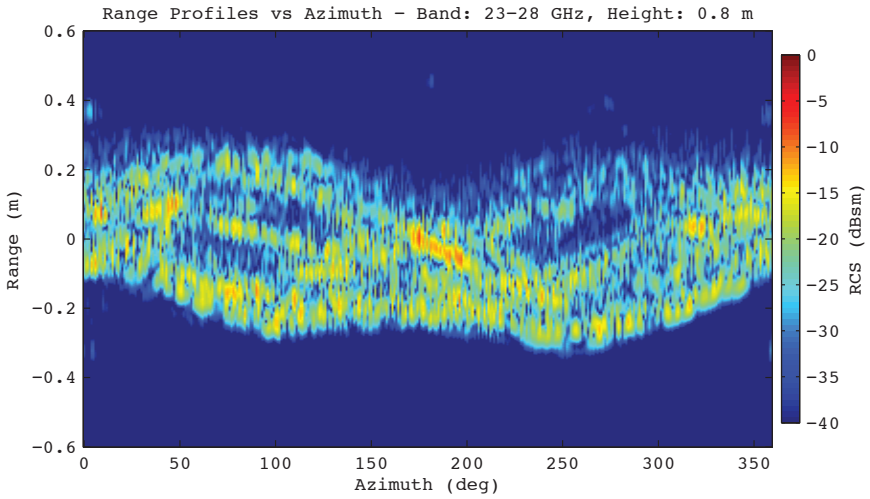

Figure 12: Example backscatter RCS versus azimuth integrating the entire frequency band 23–28 GHz for the dummy #1.

3.1.2 Backscatter RCS range profiles versus azimuth

The backscatter RCS range profiles versus azimuth have been selected as a characteristic signature of the pedestrians. The range profiles of the backscatter RCS can be computed from the frequency domain calibrated backscatter as follows:

$$\mathrm{S_t}[\mathrm{t},\phi] = \int_{\mathrm{f_{istart}}}^{\mathrm{f_{istop}}} \mathrm{S_{cal}}[\mathrm{f},\phi]\ \mathrm{W_f}[\mathrm{f}]\ \exp\left[+\frac{\mathrm{j}\,2\pi\mathrm{ft}}{\mathrm{c}}\right]\mathrm{df} \tag{8}$$

where $W_f[f]$ denotes a windowing function used to lower the sidelobes of any scatterer present in the range profile [37]. At this point, the backscatter RCS can be expressed as:

$$\mathrm{RCS_t}[\mathrm{t},\phi] = |\mathrm{S_t}[\mathrm{t},\phi]|^2 \tag{9}$$

The calculation of the backscatter RCS range profiles in Eq. (8) is rather straightforward and can be implemented very efficiently using FFT codes. An elegant implementation of the Fourier integral in Eq. (8) can also be made using the Chirp-Z transform [38], which allows a flexible definition of the extent and number of points in the time window where the backscatter is calculated. It is important to note that the backscatter RCS profiles can be obtained integrating the frequency domain data in a given sub-band or, alternatively, using the entire frequency band of the measurement. An example of backscatter RCS profiles versus azimuth for the dummy #1 is shown in Figure 12. This backscatter RCS has been calculated integrating the entire frequency band of the measurement 23–28 GHz. A Hamming frequency window has been applied in order to reduce the sidelobes in the range profiles down to 42 dB. From this result, one can conclude that the backscatter of this dummy can be modelled as an ensemble of dominant scattering centers. The sinusoidal paths that are distinguishable in the figure are associated to these scattering centers and can be used as a characteristic feature of the dummy for classification purposes. However, it must be noted that the identification of the position of the dominant scattering centers is not a simple task. The scattering centers are located at different heights and, unfortunately, the radar viewing geometry was such that it provided almost no resolution along the vertical axis.

3.1.3 Global frequency/azimuth average RCS

The third characteristic signature of the pedestrians that has been selected was the global frequency/azimuth average of the calibrated backscatter RCS. This average can be expressed as follows:

$$\mathrm{RCS}_{\mathrm{iband}}^{\mathrm{avg}} = \frac{1}{\mathrm{B_{avg}}}\frac{1}{2\pi}\int_0^{2\pi}\int_{\mathrm{f_{istart}}}^{\mathrm{f_{istop}}} |\mathrm{S_{cal}}[\mathrm{f},\phi]|^2\,\mathrm{df}\,\mathrm{d}\phi \tag{10}$$

where it can be observed that one can obtain a global average RCS at the six frequency sub-bands defined in Table 4. As an example, the global frequency/azimuth average RCS at all the sub-bands for the dummy #1 are summarized in Table 5.

Dummy Type: KIT Dummy with Clothes Frequency/Azimuth Average RCS (dBsm)						
Band (GHz)	23–24	24–25	25–26	26–27	27–28	23–28
Height=0.8m	−11.60	−11.73	−11.67	−11.44	−11.19	−11.53

Table 5: Global frequency/azimuth average RCS for the measurement on the dummy #1 at the 24 GHz band.

ID #	Identification Name	Antenna Height (m)		
		0.5 m	0.8 m	1.0 m
2	4a Dummy	X	X	X
3	Audi Bicycle and 4a Dummy	X	X	X
4	vFSS Adult Dummy	X	X	X
5	vFSS Child Dummy	X	X	X
6	NHTSA Adult Dummy	X	X	X
7	NHTSA Child Dummy	X	X	X
8	TRL/innovITS Advance Adult Dummy		X	X
9	TRL/innovITS Advance Child Dummy		X	
11	IIHS Dummy	X	X	X

Table 6: List of dummies and antenna heights of the measurement group I.

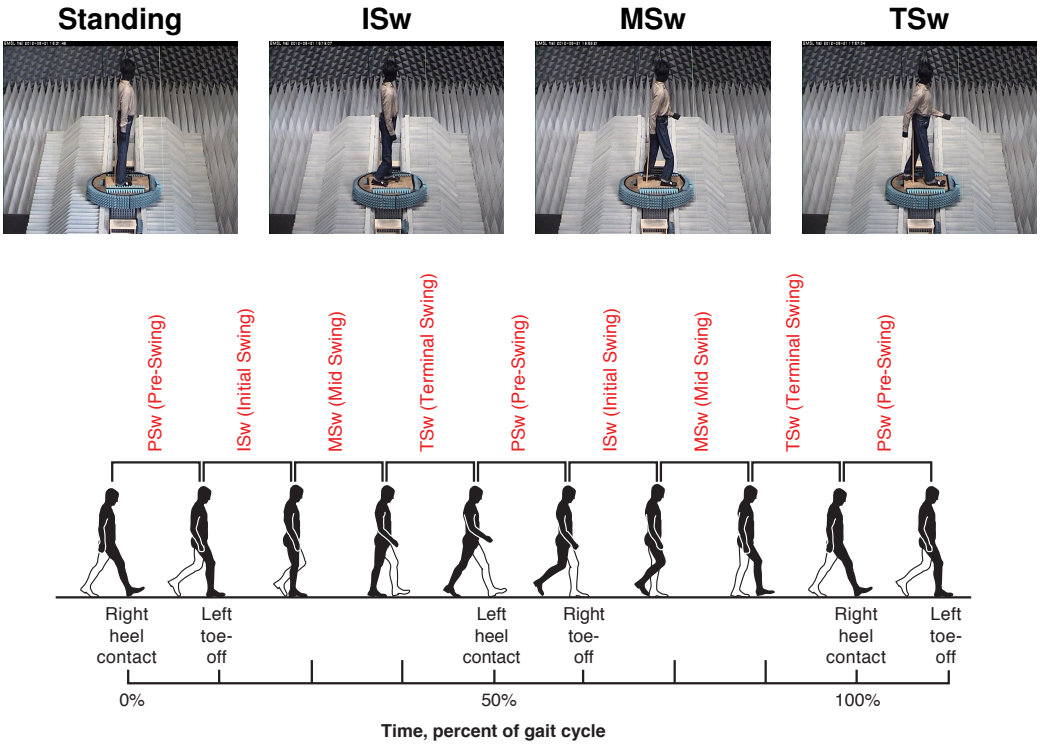

Figure 13: Pictures of the IDIADA dummy at the four positions measured (upper), and phases of the human gait with the corresponing gate cycle times (lower).

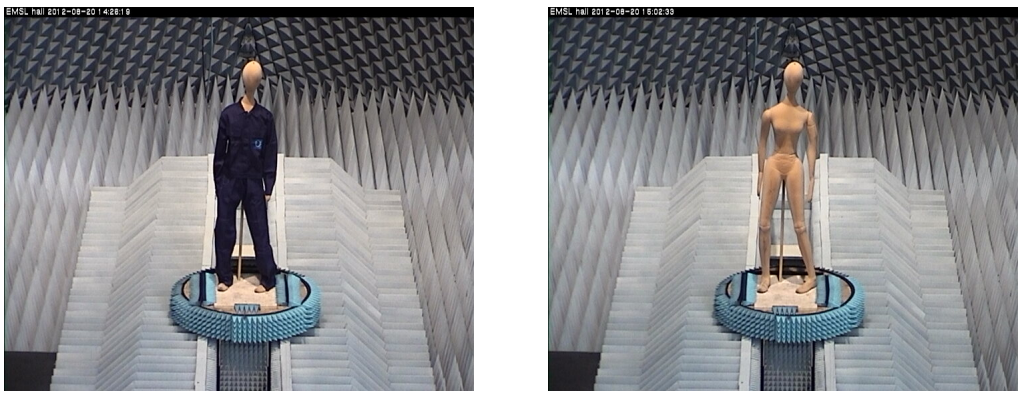

(a) **(b)**

Figure 14: Pictures of the dummy #1 on the turntable with (left) and without (right) JRC working clothes.

3.2 RCS Measurements on Pedestrian Dummies and Humans

The RCS measurements that have been selected for the present report have been divided into three different groups, namely:

Group I: In this group of measurements a selection of the available dummies were characterized at different heights of the radar antennas above the turntable. The objective of these tests was twofold: firstly, to collect the RCS signatures of the dummies under test and, secondly, to have measurements on the same dummy at different antenna heights. A sketch showing how the height of the antennas was measured is shown in Figure 3. More precisely, there was a total of seven dummies (i.e., dummies ID #2, 3, 4, 5, 6, 7, and 11 of Table 3) that were characterized at three antenna heights (i.e., H=0.5, 0.8, and 1.0 m). The dummy #8 (i.e., TRL/innovITS Advance Adult Dummy) was also measured but just at the middle and upper position (i.e., H=0.8 and 1.0 m). The complete set of results corresponding to this group of measurements is given in Appendix B. The last measurement included in this group was that of the dummy #9 (i.e., TRL/innovITS Child Dummy). The RCS signatures of this child dummy were collected only at the middle antenna position of H=0.8 m. A detailed list of the dummies and the antenna height positions actually used in the measurements is shown in Table 6.

Group II: This second group of measurements included the tests made on IDIADA dummy, which has been specifically design to assess the impact of the movement on measured RCS. The objective of these tests was to assess how the RCS signatures of a given dummy change depending the phase of the human gait cycle. This dummy was measured in five different positions at a fixed antenna height of H=0.8 m, corresponding to specific phases of the human gait [39]. A sketch showing the phases of the human gait and the corresponding gait cycle time is given in Figure 13. The five positions that were characterized were: standing, ISw (initial swing), MSw (medium swing), and the TSw (terminal swing), which was measured twice in a sequence. The complete set of results corresponding to this group of measurements is given in Appendix C.

Group III: The last group of measurements was devoted to assess the impact of clothing on the RCS signatures of pedestrian dummies and humans. This group of measurements included a series of eight tests with two humans and four different types of clothing (as shown in Figure 16), plus two additional tests on the dummy #1 with and without JRC working clothes, as illustrated in Figure 14. The complete set of results corresponding to this group of measurements is given in Appendix D.

3.2.1 Influence of Antenna Height

The series of tests conducted in the first group of measurements have been useful to assess the influence of the height of the antennas above the ground on the observed RCS signatures. Looking at the results presented in Appendix B, one can conclude that in the case

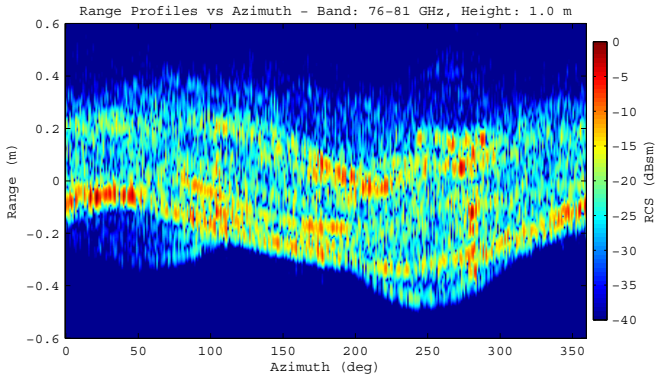

Dummy Type: vFSS Adult

Frequency/Azimuth Average RCS (dBsm)

Band (GHz)	76-77	77-78	78-79	79-80	80-81	76-81
Height=0.5 m	-8.29	-8.33	-8.55	-7.99	-7.94	-8.22
Height=0.8 m	-7.80	-8.27	-7.53	-7.33	-7.26	-7.63
Height=1.0 m	-7.25	-7.34	-7.25	-6.77	-6.70	-7.06

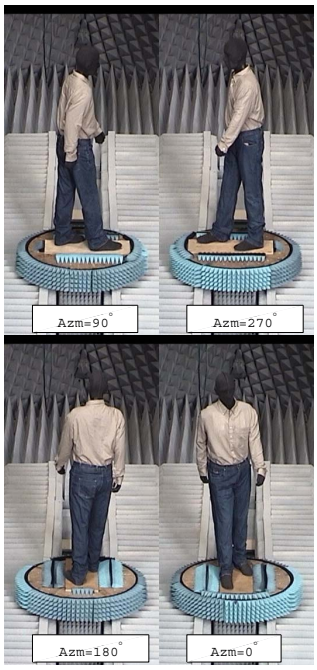

(a)

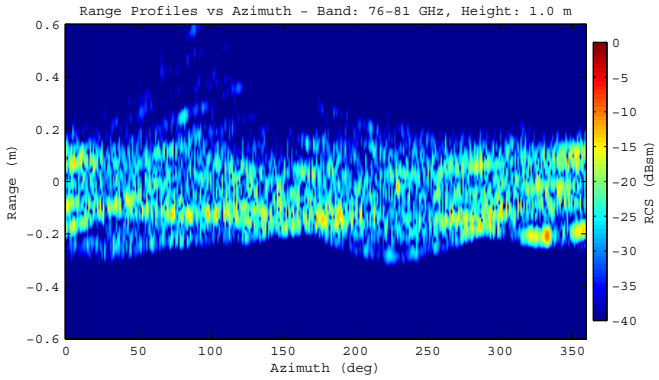

Dummy Type: vFSS Child

Frequency/Azimuth Average RCS (dBsm)

Band (GHz)	76-77	77-78	78-79	79-80	80-81	76-81
Height=0.5 m	-8.80	-8.96	-8.57	-8.31	-8.15	-8.55
Height=0.8 m	-11.97	-12.11	-11.68	-11.33	-11.20	-11.65
Height=1.0 m	-14.47	-14.57	-14.17	-13.81	-14.14	-14.22

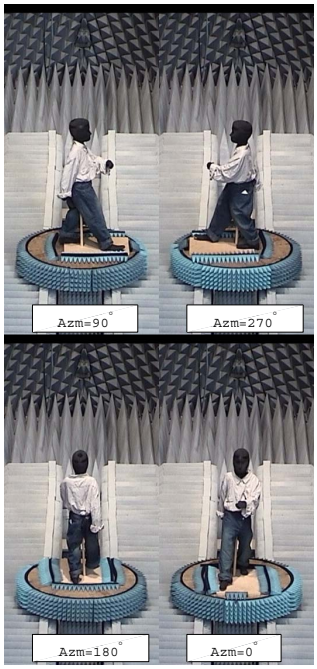

(b)

Figure 15: Measured RCS signatures at three different heights for the adult (upper) and child dummy (lower) in the 76–81 GHz frequency band.

of the adult dummies the highest RCS is normally observed at the middle antenna position (i.e., H=0.8 m). The influence of the antenna heigth seems to be more evident on the global frequency/azimuth average RCS, where differences in the range 1-2 dB can be seen. The polar plots of the frequency average RCS versus azimuth show some similar patterns at the three height positions. On the contrary, some very significant changes of the RCS signatures have been observed in the case of the measurements on the child dummies when the antenna height was changed. In fact, the measured RCS on the child dummy has been significantly higher at the lowest position of the antennas. Assuming one can model the human body as a vertical cylinder of finite length, it is clear that the measured RCS shall be maximum when the incidence is normal to the center position of the cylinder. Slightly oblique incidence angles will lower the RCS because of the fact that the reflected electromagnetic wavefront will be located in the specular direction. Noting that the adult and child dummy show a clear height offset of their center of gravity, one can therefore expect a higher RCS at the lower antenna position on the child dummy and, on the contratry, a higher RCS at the middle position for the adult dummy. This is clearly illustrated in Figure 15, where the RCS signatures of both a child and adult dummies are shown in the 76–81 GHz frequency band. In this example, the average RCS of the child dummy varies significantly as a function of the antenna height, and a difference of almost 6 dB between the RCS at the high and low positions is observed. This clearly proves that the RCS at the lower antenna position is significantly higher. The differences between the RCS at the high and low positions are more significant in the high frequency band, something that was certainly expected.

3.2.2 Influence of Clothing

A dedicated series of tests was carried out to assess the effect of different types of clothes on the observed RCS of pedestrians. As in the previous measurements, the RCS backscatter data was collected in the frequency bands at 24 and 77 GHz. Results did not show significant variations of the frequency average of the RCS of a human wearing cotton shirt, laboratory coat or a woolen jacket. A possible explanation for this result is that all these clothes are electrically thin (i.e., thickness is much smaller than the wavelength) and dry, which makes them almost transparent to the electromagnetic waves. Consequently, in the case of these three clothes, the observed RCS will be basically that of the pedestrian body and will not depend on the clothes worn. However, it is expected that this might not be the case with other types of clothes. Clothes that are electrically thick and show smooth planar facets pointing towards the radar that may have a signficant contribution to the observed RCS at some specific aspect angles. In order to investigate this assumption, a second series of experiments was performed, in this occasion using clothes of larger sizes. In addition to thin summer shirts, clothes consisted of a 250 μm thick PVC coated polyester rain coat (yellow coat), a 150 μm thick PVC coated nylon rain coat (blue coat) and a multilayered parka worn by two adults of different size, as illustrated in the snapshots shown in Figure 16. Results show that the RCS observed on the taller adult (i.e., adult #1) is slighly higher than that of adult #2. The influence of the clothing observed on the taller adult is minor in the 23–28 GHz band, with just a slight increase when he was wearing the multilayered parka. The variability

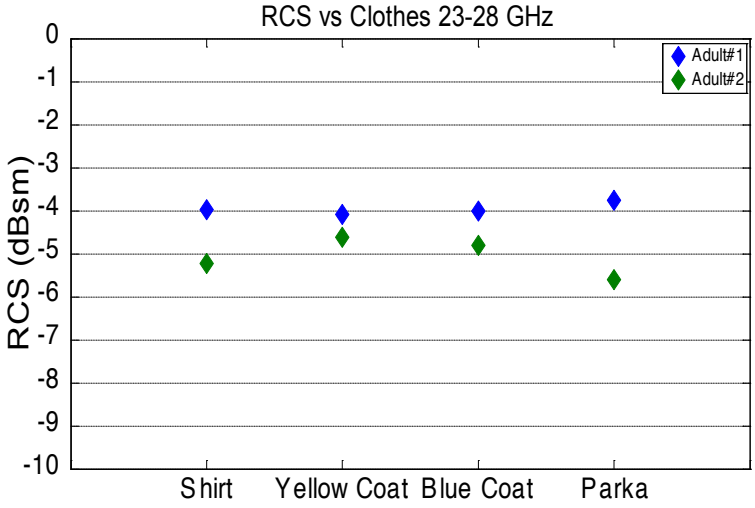

(a)

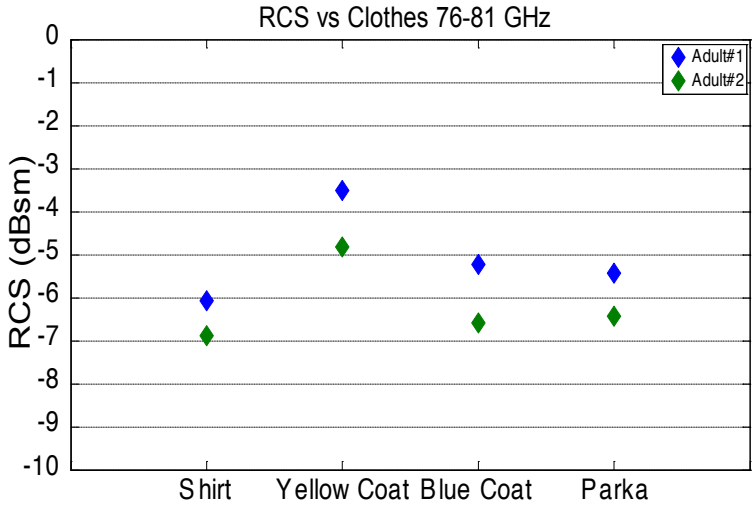

(b)

Figure 16: Summary of the results of the measurements to assess the impact of clothing on the RCS at the 24 (a) and 77 GHz (b) frequency bands.

Item #	Item Name	Manufacturer	Fibre Composition	Size	Picture
1	Working shirt	Textil GOR http://www.textilgor.it	100 % Cotton	T46	
2	Working shirt	Textil GOR	100 % Cotton	T50	
3	Working shirt	Textil GOR	100 % Cotton	T54	
4	Trouser	Professional Serio	Canvas 100 % Cotton	M	
5	Trouser	Professional Serio	Canvas 100 % Cotton	L	
6	Trouser	Professional Serio	Canvas 100 % Cotton	XXL	
7	Laboratory Coat	N.A.	100% Cotton	M	
8	Laboratory Coat	N.A.	100% Cotton	L	
9	Laboratory Coat	N.A.	100% Cotton	XL	
10	Laboratory Coat	N.A.	65% Polyester 35% Cotton	M	
11	Laboratory Coat	N.A.	65% Polyester 35% Cotton	L	
12	Laboratory Coat	N.A.	65% Polyester 35% Cotton	XL	
13	Parka	Industrial Starter http://www.industrialstarter.com	N.A.	L	
14	Yellow Rain Coat	Panoply http://www.deltaplus.fr	PVC/Polyester/PVC	L	
15	Blue Rain Coat	Industrial Starter http://www.industrialstarter.com	PVC Coated Nylon	L	

Table 7: List of clothes used in the RCS measurements with the manufacturer and fibre composition information.

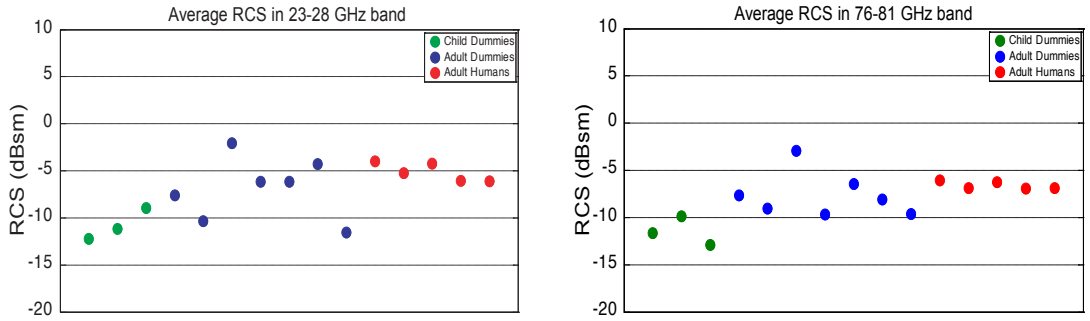

(a) **(b)**

Figure 17: Comparison of the global frequency/azimuth RCS averages of all the dummies and humans characterized: (left) 23–28 GHz band, and (right) 76–81 GHz band.

of the RCS on the second adult in the lower frequency band is slightly higher, showing a small decrease of the RCS when he was wearing the cotton shirt and the multilayered parka. The behaviour of the RCS in the 76–81 GHz frequency band is quite different and a much higher variability due to clothing is observed on both adults. It is also interesting to see that the observed RCS on the two adults is highly correlated. The lowest RCS is observed when the adults were wearing a cotton shirt. On the other hand, the highest RCS was observed with the thick yellow rain coat. In between, a rather similar RCS was observed when the adults were wearing the blue coat and the multilayered parka. The differences between the highest and lowest RCS observed were about 2.5 dB. In short, it can be concluded that the influence of the clothing is more important in the 76–81 GHz band, and particularly when very thick clothes are worn.

A detailed list of the clothes that were used in the various tests described above and some additional ones not reported here is provided in Table 7. On some clothes, the fibre composition information was available and has been included.

3.2.3 Similarity of RCS Signatures of Dummies and Humans

Although the main objective of the RCS measurement campaign was not that of assessing quantitatively the similarity of the RCS signatures from dummies and humans, one can nevertheless complete a qualitative assessment. Having a look to the global frequency/azimuth RCS averages in the two frequency bands, it can be concluded the measured RCS of the two humans are slighly above those of most of the adult dummies. This difference is more evident in the 76–81 GHz band, where the RCS of the adult dummies is about 2-4 dB smaller. In the lower frequency band, the dispersion of the average RCS measured on the adult dummies is larger and therefore a proper comparison cannot be made easily. The RCS averages of the child dummies are smaller than those of the adult dummies and the humans in both frequency bands. This difference has been estimated to be in the order of 5 dB. Overall, it can be said that the RCS averages in the 23–28 GHz and 76–81 GHz frequency bands are quite close and they do not show significant differences. A summary of the measured RCS

averages in the two frequency bands for all the targets that were characterized is shown in Figure 17.

4 Conclusions

An RCS measurement campaign on a wide range of different pedestrian dummies currently used for the testing of automotive short range radar (SRR) sensors was completed in August 2012. This work was carried out in the context of the EC FP7 ICT Project MOSARIM and was aimed at establishing a reference library with the RCS signatures of pedestrian dummies and humans in the 24 GHz and 77 GHz bands. The measurements took place at the EC Joint Research Center in Ispra, Italy, in the hemi-spherical anechoic chamber of the European Microwave Signature Laboratory. A rather unique test set-up acquiring simultaneously the RCS data in the two SRR frequency bands of 23–28 GHz and 76–81 GHz was designed and put in place for this measurement campaign. A total of 11 pedestrian dummies and a few adult humans were used in a extensive series of tests. Some more than 100 measurements lasting for almost three entire weeks were completed.

An important result of this measurement campaign has been that, for the first time, an extensive library of RCS signatures of a wide range of pedestrian dummies has been collected simultaneously in the two main SRR frequency bands, namely, 23–28 GHz and 76–81 GHz. On purpuse, the bandwidth of the twe measurements was set as wide as possible in order to make the collected RCS signatures valuable to test both narrow-band and wide-band SRR sensors. The calibration of the RCS data was a key aspect of this measurement campaign. Following a series of tests, a calibration procedure combining the use of two reference targets (i.e., a metal disc and a sphere) was finally chosen because of its higher accuracy and repeatibility.

A first analysis of the complete set of the various RCS signatures collected on all the pedestrian dummies and humans allows to draw the following qualitative assessments:

- The observed global frequency/azimuth RCS averages in the two frequency bands are quite close and they do not show significant differences. This is an important finding given the fact that there is a current trend to manufacture almost exclusively SRR systems at the 77 and 79 GHz bands.

- A first analysis on the impact of the pedestrians' height on the measured RCS signatures has been completed. Results show that, particularly in the higher frequency bands, the height of the pedestrian has a clear effect on the RCS averages observed. In the case of the child dummies, for instance, the observed RCS at the lower antenna height (i.e., aligned with the center of mass of the dummy) was 6 dB above that observed at a position 0.5 m higher.

- A first qualitative comparison of the RCS signatures between dummies and humans was also completed. Results show that the RCS averages of the available dummies are slightly below those of the humans. It has also been observed that some of the dummies showed some peculiar dependence of the average RCS versus azimuth (e.g., a square shape with four clear corners), making them clearly distinguishable and different from all the other targets.

- A dedicated set of the measurements was designed to assess the impact of clothing on the measured RCS signatures. It was found that in most cases clothing did not impact significantly the RCS signatures observed. It was observed, as expected, that the impact is more evident in the high frequency band of 76–81 GHz, in particular, when some very thick clothes were worn.

Finally, it is important to note that a more exhaustive analysis of the data collected in this measurement campaign is currently being carried out. Subjects of interest that need to be addressed more in detail include the definition of robust RCS signatures that can be used for classification purposes, and the identification of robust techniques to assess quantitatively the degree of similarity between two different targets.

A Bistatic RCS of a Metal Sphere

The problem of the scattering of a monochromatic plane wave by a conducting sphere is well known in the literature [40, 41]. Here we are interested in using a conducting sphere to calibrate precisely the bistatic radar cross section (RCS) measurements made using a vector network analyzer in two different frequency bands, respectively, 23–28 GHz and 76–81 GHz. The radius of the sphere is a and the wavenumber $k = 2\pi/\lambda$, where λ is the wavelength at the working frequency. The two illumination geometries are shown in Figure A.1. The two polarizations that are appropriate for a calibration measurement are HH and VV only, simply because the cross-polar components of the scattered field are too small or null in some cases (e.g., monostatic incidence).

The closed form of the bistatic RCS in the HH and VV cases can be written as follows:

$$\sigma_{\mathrm{HH}}(\theta) = \lim_{r\to\infty}\left[4\pi r^2\frac{|\mathbf{E^s}|^2}{|\mathbf{E^i}|^2}\right] = \frac{\lambda^2}{\pi}|A_\theta(\theta)|^2 \tag{A.1}$$

$$\sigma_{\mathrm{VV}}(\theta) = \frac{\lambda^2}{\pi}|A_\phi(\theta)|^2 \tag{A.2}$$

where $\mathbf{E^i}$ and $\mathbf{E^s}$ denote, respectively, the incident and scattered electric vector fields at the transmit and receive antennas, θ denotes the bistatic angle, $A_\theta(\theta)$ and $A_\phi(\theta)$ are the θ and ϕ components of the vector potential $\mathbf{A}$ in an spherical coordinate system, which can be expressed as follows:

$$A_\theta(\theta) = \sum_{n=1}^{\infty} j^{-n}\left[c_n\frac{P_n'^1(\cos\theta)}{\sin\theta} - b_n\sin\theta\, P_n^1(\cos\theta)\right] \tag{A.3}$$

$$A_\phi(\theta) = \sum_{n=1}^{\infty} j^{-n}\left[c_n\sin\theta\, P_n'^1(\cos\theta) - b_n\frac{P_n^1(\cos\theta)}{\sin\theta}\right] \tag{A.4}$$

where $P_n^1(\cdot)$ and $P_n'^1(\cdot)$ denote, respectively, the associated Legendre functions and its derivative. The coefficients of the spherical wave expansion in Eqs. A.3 and A.4 are given by the following expressions:

$$b_n = -j^{-n}\frac{2n+1}{n(n+1)}\frac{\hat{J}_n'(ka)}{\hat{H}_n'^{(2)}(ka)} \tag{A.5}$$

$$c_n = -j^{-n}\frac{2n+1}{n(n+1)}\frac{\hat{J}_n(ka)}{\hat{H}_n^{(2)}(ka)} \tag{A.6}$$

$$\tag{A.7}$$

with the spherical Bessel and Hankel functions $\hat{J}_n(\cdot)$ and $\hat{H}_n^{(2)}(\dot{})$ expressed as a function of the regular Bessel and Hankel functions as follows:

$$\hat{J}_n(ka) = \sqrt{\frac{\pi ka}{2}}\,J_{n+1/2}(ka) \tag{A.8}$$

$$\hat{H}_n^{(2)}(ka) = \sqrt{\frac{\pi ka}{2}}\,H_{n+1/2}^{(2)}(ka) \tag{A.9}$$

where $\hat{J}'_n(\cdot)$ and $\hat{H}'^{(2)}_n(\cdot)$ denote, respectively, the derivatives of the Bessel and Hankel functions.

The spherical wave expansions of Eqs. A.3 and A.4 have an infinite number of terms. In practice, one has to terminate the serieas after a N terms. A practical rule of thumb is to use a number of terms of the same order of magnitude as ka. This means that the number of spherical modes in the series expansion increases with an increasing electrical size of the sphere. As an example, the minimum number of modes that guarantees an error below 4% is given by [26, 42]:

$$N \simeq 14 + 1.16\, ka \tag{A.10}$$

Since the computation of the RCS by spheres that are electrically large implies the inclusion of high order spherical modes, one must take into account some important implementation aspects. Firstly, the calculation of the coefficients b_n and c_n is a bit tricky even using mathematical toolkits such as Matlab or Mathematica. Numerators and denominators of these coefficients must be generated recursively in order to ensure a proper convergence of the series expansion. In practice, one must use a forward and backward recursions, respectively, for the calculation of the Bessel and Hankel functions in these coefficients. Secondly, the calculation of high order associated Legendre functions should be made using a forward recursion only in order to guarantee the convergence of the series. A direct call to these functions using mathematical toolkits will may not give results with the required accuracy. The details on the implementation of the recursions needed to calculate the spherical Bessel and Hankel functions, and that of the associated Legendre functions may be found in [43].

The conducting sphere used in the calibration measurements subject of this report had a diameter of 3 inches. Both the monostatic and bistatic RCSs of this calibration target were calculated in order to be able to use this sphere as a reference target in our measurements. As an example, the monostatic RCS or Mie solution computed in the two frequency bands used in the measurements are shown in Figure A.2. The number of spherical modes used in the series expansion is 28 and 80, respectively, in the low and high frequency bands, ensuring an error well below 1%. It is important to observe that in both frequency bands we are well within the high frequency region [26], and consequently the monostatic RCS is close to the physical optics solution (i.e., $\sigma \simeq \pi\, a^2$), which corresponds to an RCS of –23.41 dBsm. Interestingly, that means the RCS of our reference target is almost the same in the two frequency bands, showing just some tiny differences. This similarity is kept also in the bistatic case for quite a large angular extent of the bistatic angle, as shown in Figure A.3.

It can be concluded that the use of the physical optics approximation is perfectly valid for the two frequency bands of the measurements. In addition, the fact of using a quasi monostatic configuration of the transmit and receive antennas with a small separation distance, which has associated a small bistatic angle (e.g., about 2.5° in the set-up used in our measurements), does not influence the measured RCS of the calibration sphere, remaining in any case always very close to the physical optics solution (i.e., HH and VV illumination geometries). Noticing that the set-up used in the measurements is designed for the VV po-

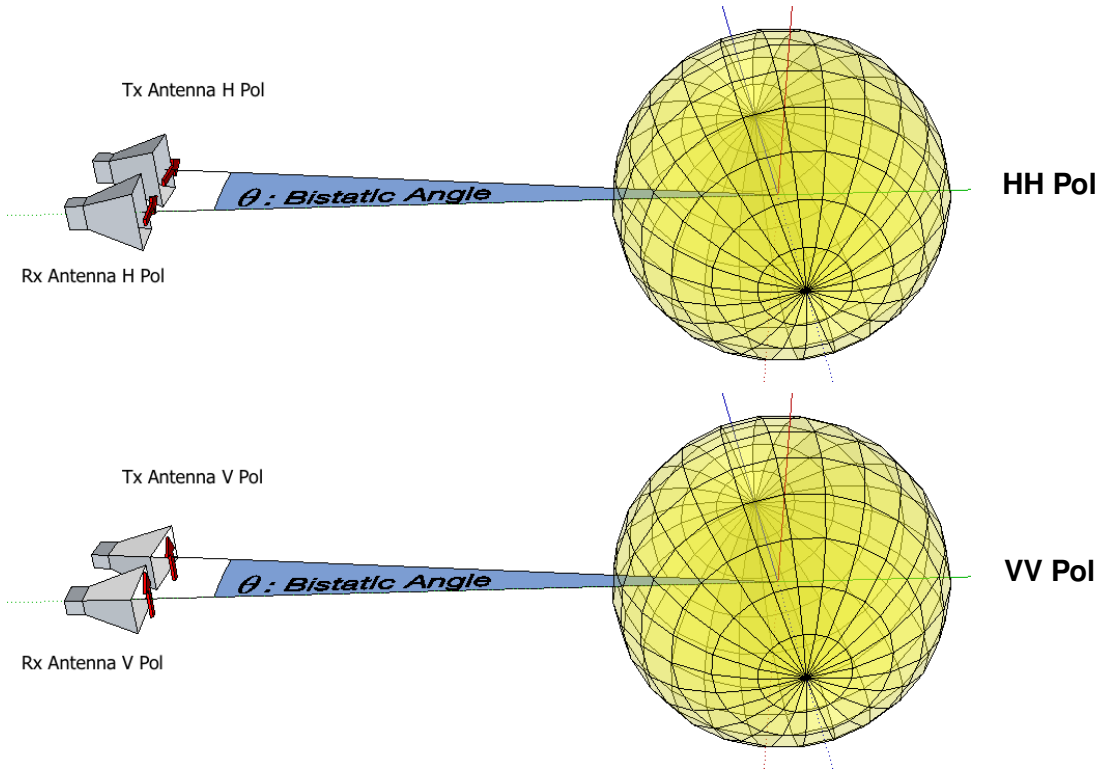

Figure A.1: Bistatic RCS of a metal sphere: illumination geometries for HH (left) and VV (right) polarizations.

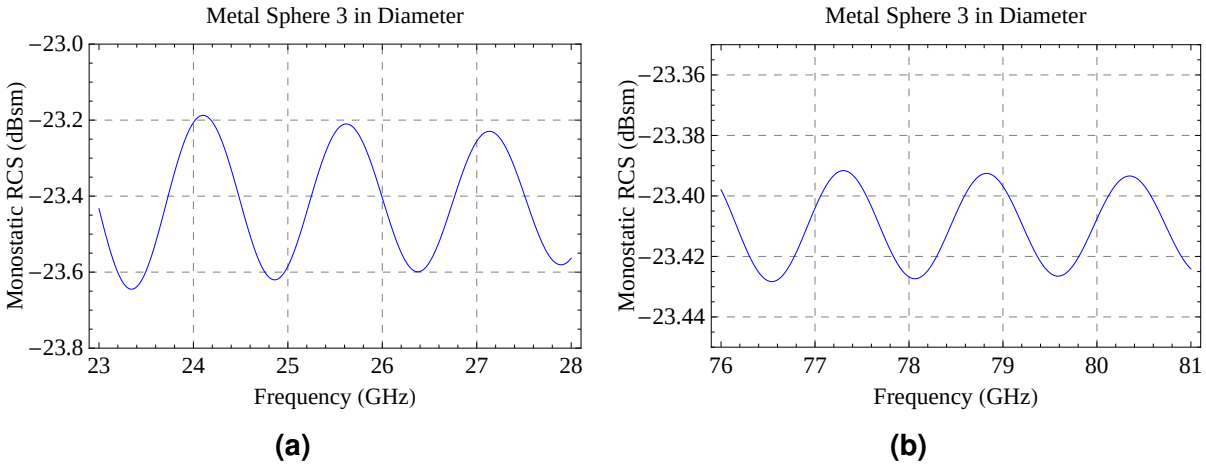

Figure A.2: Monostatic RCS of a 3 in metal sphere in the 23–28 GHz (left) and 76–81 GHz (right) frequency bands.

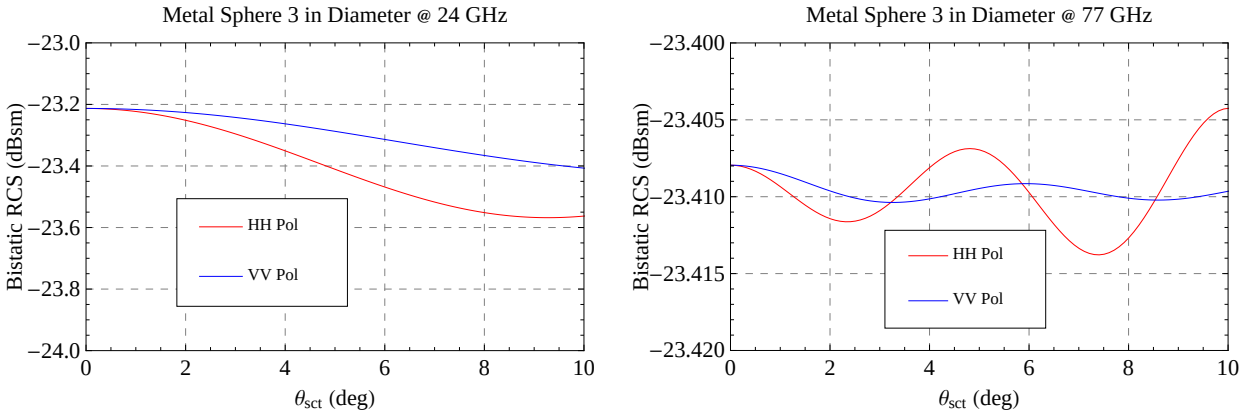

(a) **(b)**

Figure A.3: Bistatic RCS of a 3 in metal sphere, respectively, at 24 (left) and 77 GHz (right) for a bistatic angular extent of 10 deg: HH (red) and VV (blue) polarizations.

larization only, one can conclude that the choice of a conducting sphere to calibrate the RCS data is perfectly adequate and should guarantee a very high accuracy.

B RCS Signatures of Pedestrians: Measurement Group I

The captions of the figures included in this annex is provided here due to formatting constraints. The complete list of captions is shown in Table B.1.

Figure	Caption	Page No.
B.1	RCS Signatures of dummy #2 (4a adult dummy) in the 23–28 GHz band at three antenna heights.	36
B.2	RCS Signatures of dummy #2 (4a adult dummy) in the 76–81 GHz band at three antenna heights.	37
B.3	RCS Signatures of dummy #3 (Audi bike and 4a adult dummy) in the 23–28 GHz band at three antenna heights.	38
B.4	RCS Signatures of dummy #3 (Audi bike and 4a adult dummy) in the 76–81 GHz band at three antenna heights.	39
B.5	RCS Signatures of dummy #4 (vFSS adult dummy) in the 23–28 GHz band at three antenna heights.	40
B.6	RCS Signatures of dummy #4 (vFSS adult dummy) in the 76–81 GHz band at three antenna heights.	41
B.7	RCS Signatures of dummy #5 (vFSS child dummy) in the 23–28 GHz band at three antenna heights.	42
B.8	RCS Signatures of dummy #5 (vFSS child dummy) in the 76–81 GHz band at three antenna heights.	43
B.9	RCS Signatures of dummy #6 (NHTSA adult dummy) in the 23–28 GHz band at three antenna heights.	44
B.10	RCS Signatures of dummy #6 (NHTSA adult dummy) in the 76–81 GHz band at three antenna heights.	45
B.11	RCS Signatures of dummy #7 (NHTSA child dummy) in the 23–28 GHz band at three antenna heights.	46
B.12	RCS Signatures of dummy #7 (NHTSA child dummy) in the 76–81 GHz band at three antenna heights.	47
B.13	RCS Signatures of dummy #11 (IIHS adult dummy) in the 23–28 GHz band at three antenna heights.	48
B.14	RCS Signatures of dummy #11 (IIHS adult dummy) in the 76–81 GHz band at three antenna heights.	49
B.15	RCS Signatures of dummy #8 (TRL/innovITS Advance adult dummy) in the 23–28 GHz band at two antenna heights.	50
B.16	RCS Signatures of dummy #8 (TRL/innovITS Advance adult dummy) in the 76–81 GHz band at two antenna heights.	51
B.17	RCS Signatures of dummy #9 (TRL/innovITS Advance child dummy) in the 23–28 GHz band at two antenna heights.	52
B.18	RCS Signatures of dummy #9 (TRL/innovITS Advance child dummy) in the 76–81 GHz band at two antenna heights.	53

Table B.1: List of captions for the figures with the RCS signatures of measurement group I.

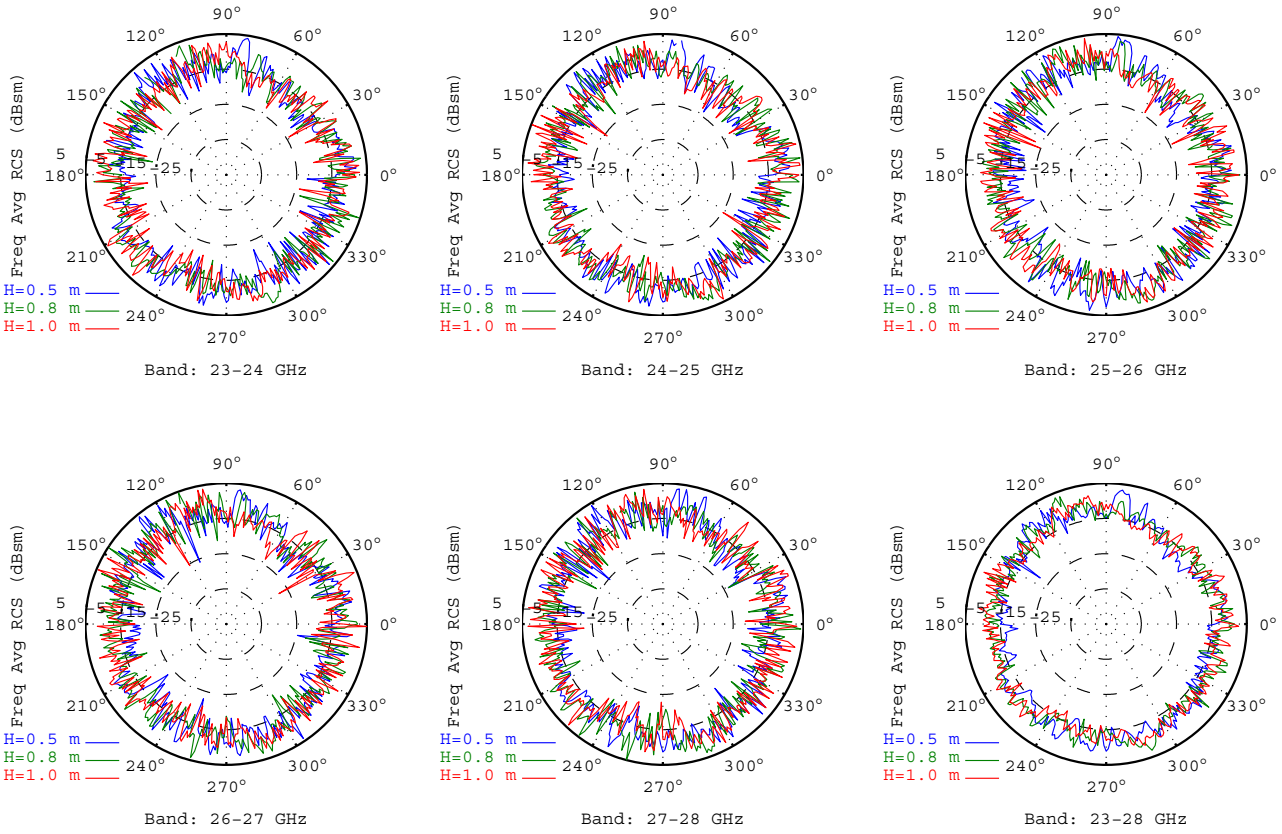

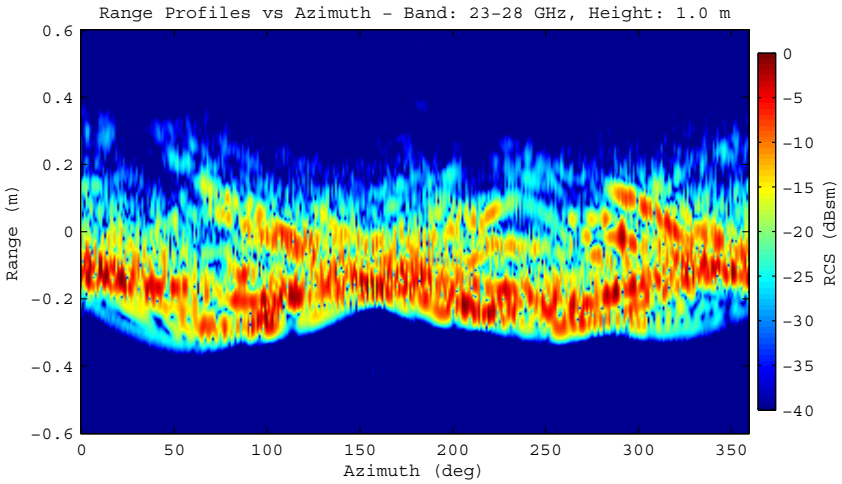

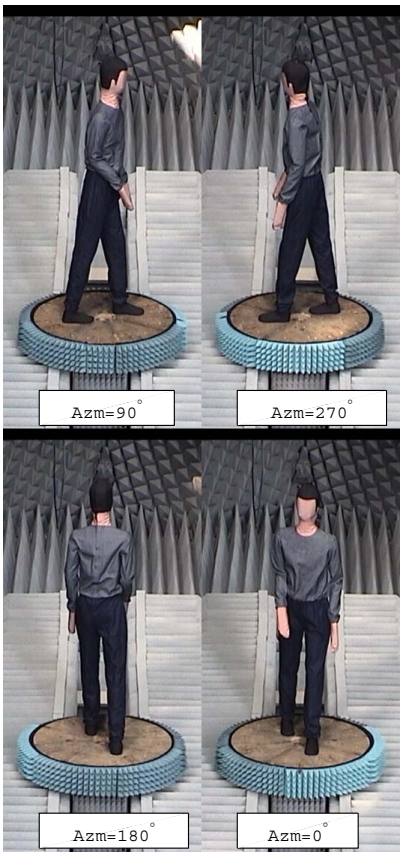

Dummy Type: 4a Adult

Frequency/Azimuth Average RCS (dBsm)

Band (GHz)	23-24	24-25	25-26	26-27	27-28	23-28
Height=0.5 m	-2.71	-2.56	-2.59	-2.77	-2.43	-2.61
Height=0.8 m	-2.15	-2.05	-2.27	-1.96	-2.01	-2.08
Height=1.0 m	-2.32	-2.20	-2.22	-2.25	-1.93	-2.19

Figure B.1

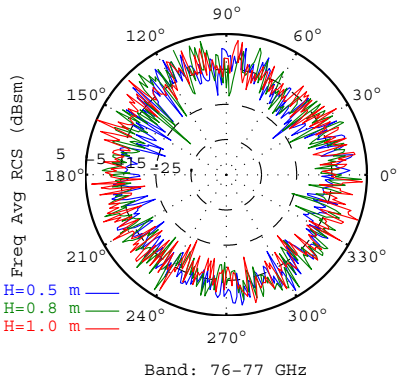

Band: 76-77 GHz

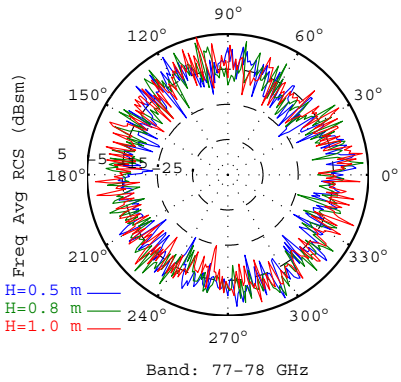

Band: 77-78 GHz

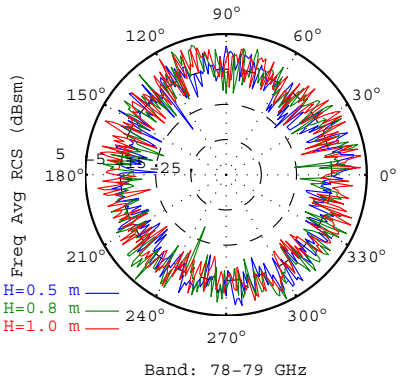

Band: 78-79 GHz

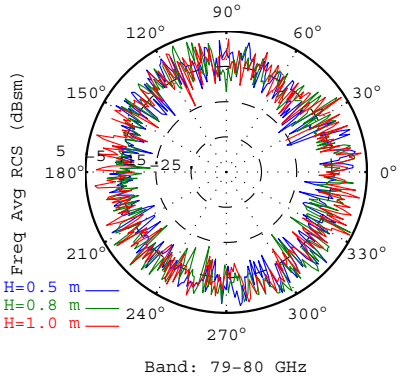

Band: 79-80 GHz

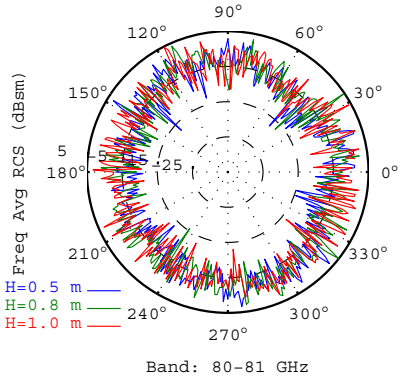

Band: 80-81 GHz

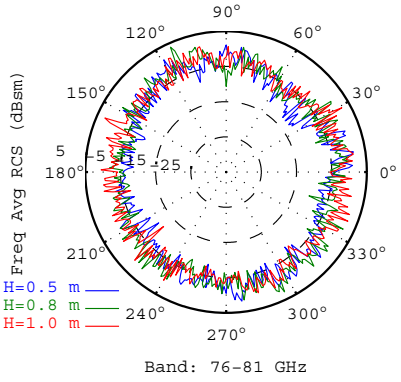

Band: 76-81 GHz

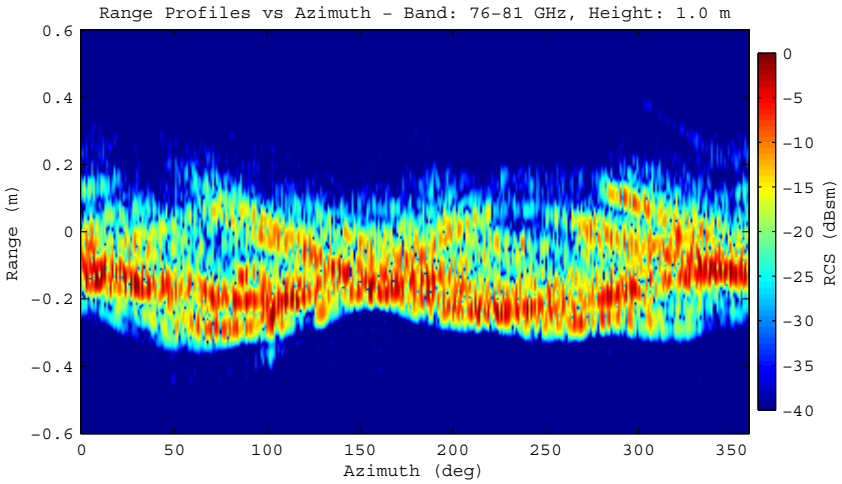

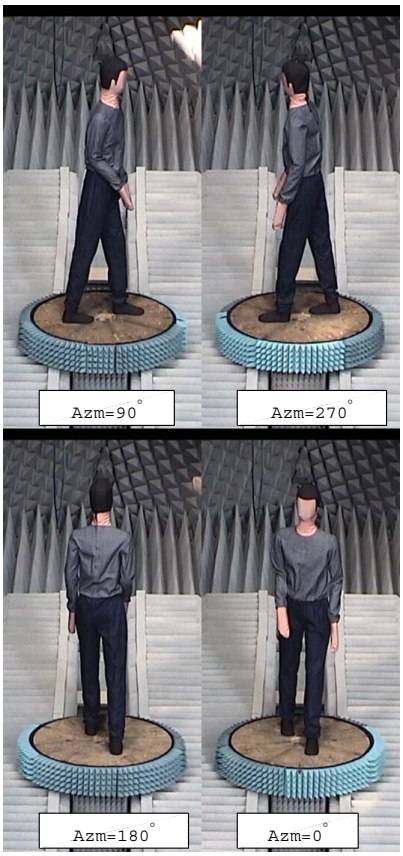

Dummy Type: 4a Adult

Frequency/Azimuth Average RCS (dBsm)

Band (GHz)	76-77	77-78	78-79	79-80	80-81	76-81
Height=0.5 m	-3.97	-4.07	-3.86	-3.32	-3.24	-3.68
Height=0.8 m	-3.05	-3.38	-2.89	-2.56	-2.74	-2.92
Height=1.0 m	-2.78	-3.21	-2.66	-2.31	-2.24	-2.63

Figure B.2

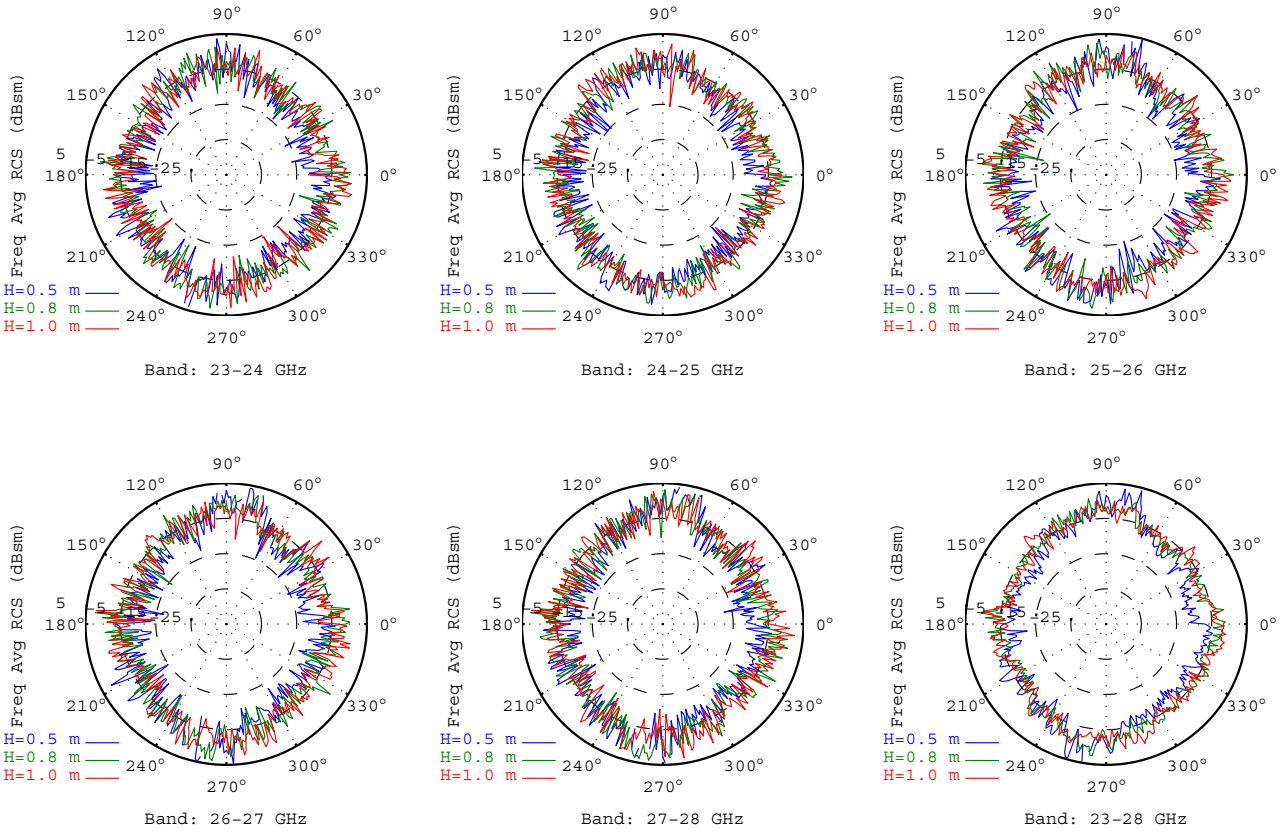

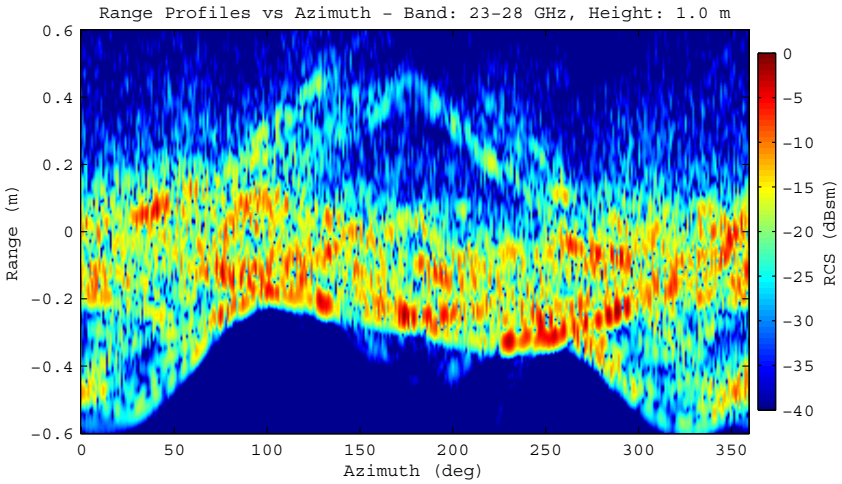

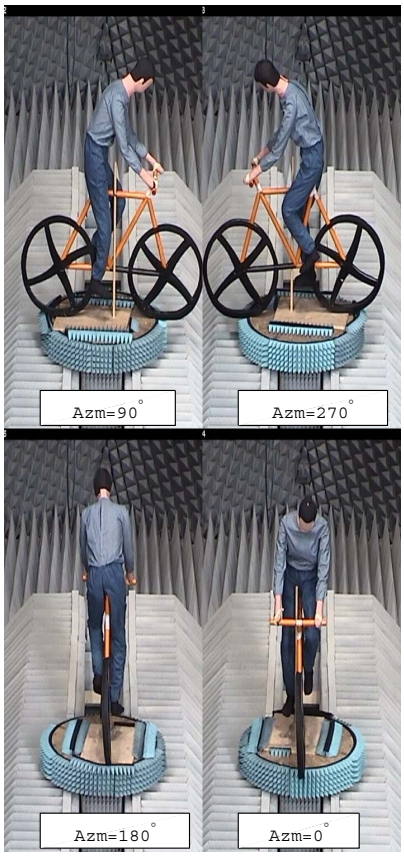

Dummy Type: Audi Bike and 4a Adult

Frequency/Azimuth Average RCS (dBsm)

Band (GHz)	23-24	24-25	25-26	26-27	27-28	23-28
Height=0.5 m	-5.17	-5.63	-4.87	-3.36	-3.06	-4.31
Height=0.8 m	-4.11	-4.16	-4.22	-3.81	-3.39	-3.94
Height=1.0 m	-4.24	-4.04	-4.02	-3.81	-3.49	-3.92

Figure B.3

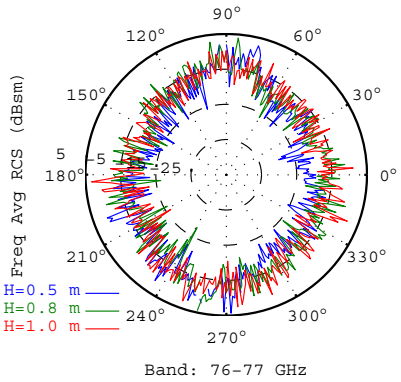

Band: 76-77 GHz

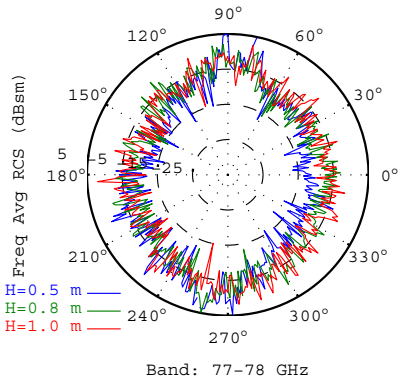

Band: 77-78 GHz

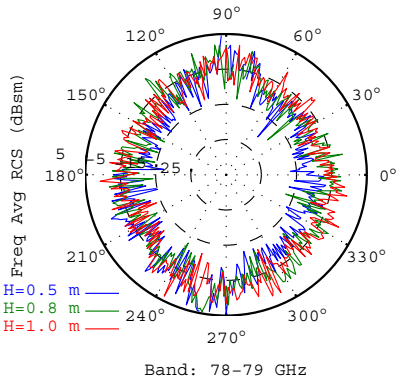

Band: 78-79 GHz

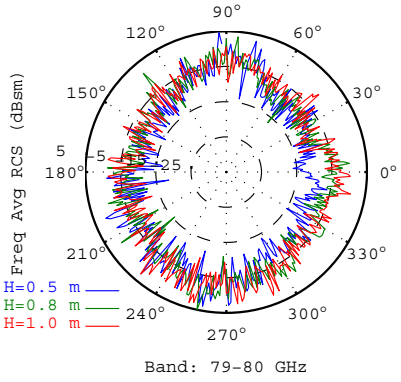

Band: 79-80 GHz

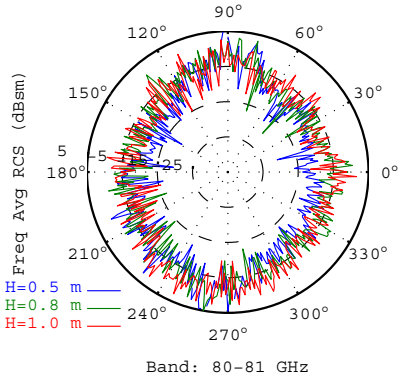

Band: 80-81 GHz

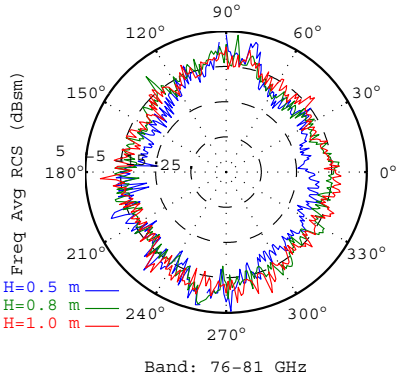

Band: 76-81 GHz

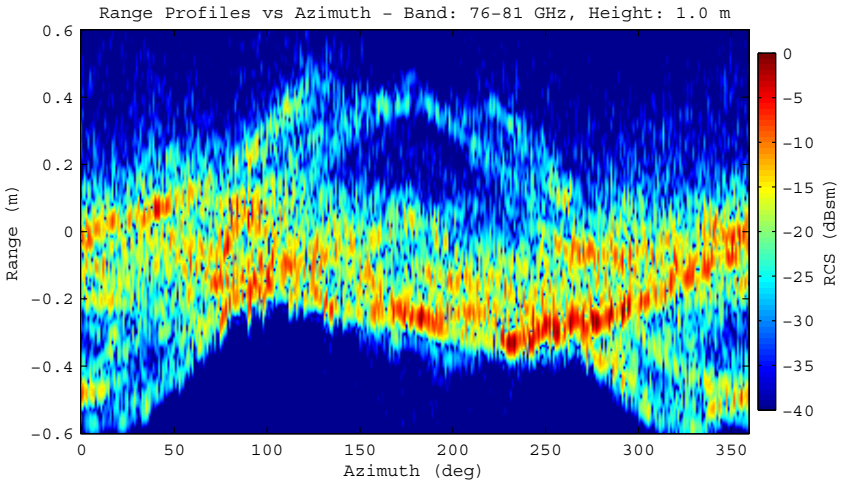

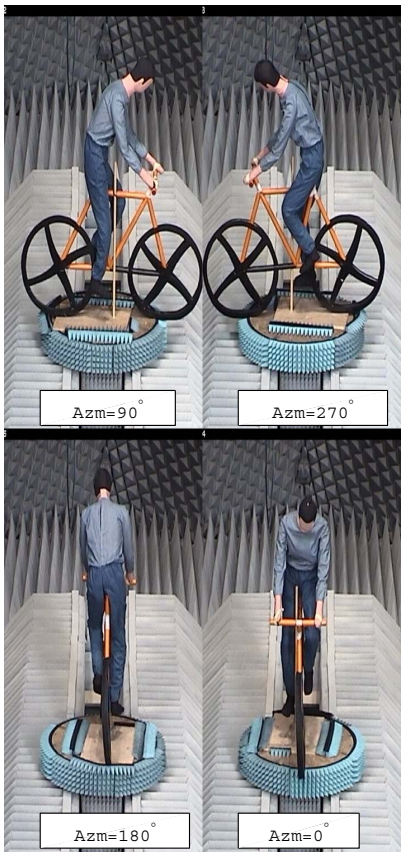

Dummy Type: Audi Bike and 4a Adult

Frequency/Azimuth Average RCS (dBsm)

Band (GHz)	76-77	77-78	78-79	79-80	80-81	76-81
Height=0.5 m	-4.70	-4.75	-4.55	-5.20	-4.74	-4.79
Height=0.8 m	-4.82	-5.08	-4.44	-4.57	-4.35	-4.65
Height=1.0 m	-4.67	-4.74	-4.31	-4.12	-4.02	-4.36

Figure B.4

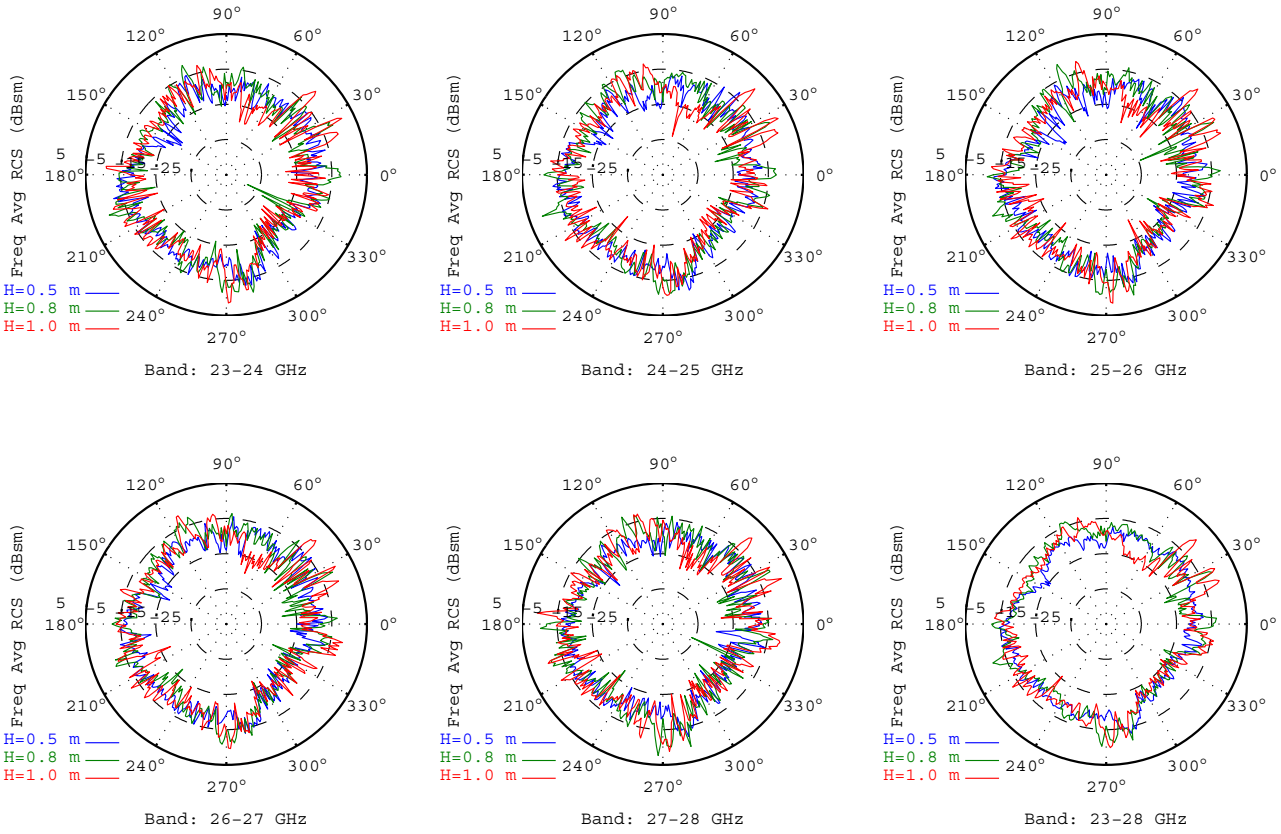

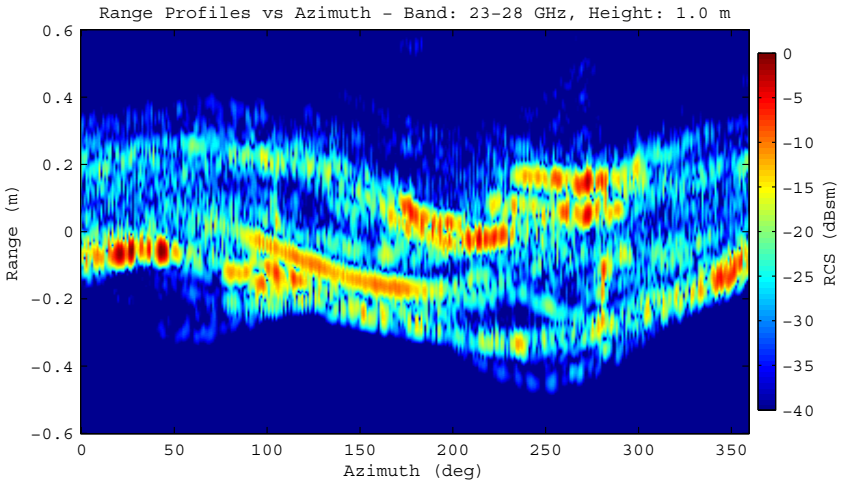

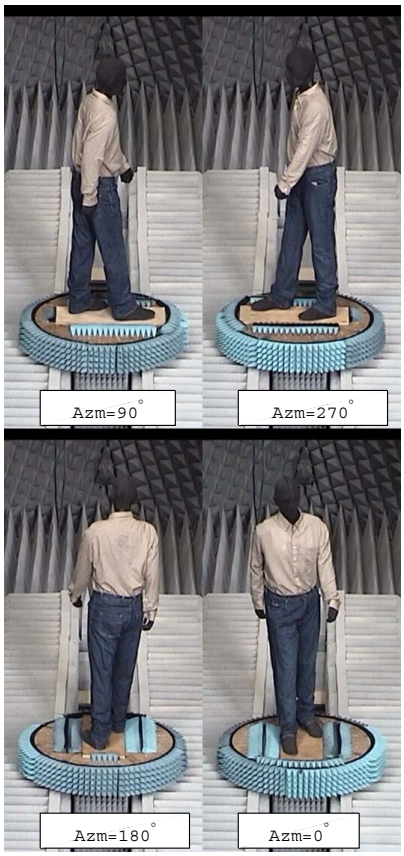

Dummy Type: vFSS Adult

Frequency/Azimuth Average RCS (dBsm)

Band (GHz)	23-24	24-25	25-26	26-27	27-28	23-28
Height=0.5 m	-8.93	-8.69	-8.77	-8.81	-9.08	-8.85
Height=0.8 m	-7.78	-7.50	-7.55	-7.79	-7.45	-7.61
Height=1.0 m	-7.89	-7.76	-7.79	-7.45	-7.14	-7.60

Figure B.5

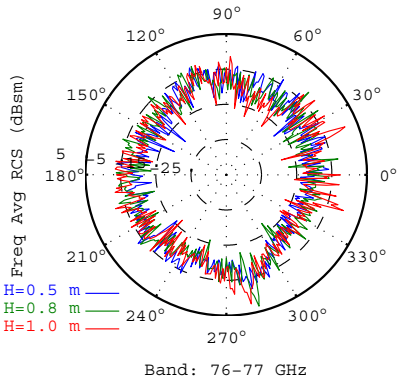

Band: 76-77 GHz

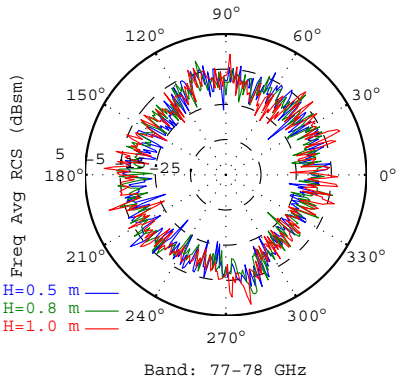

Band: 77-78 GHz

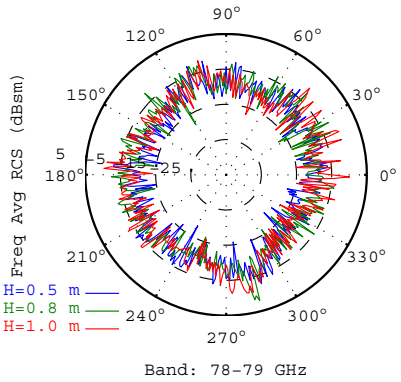

Band: 78-79 GHz

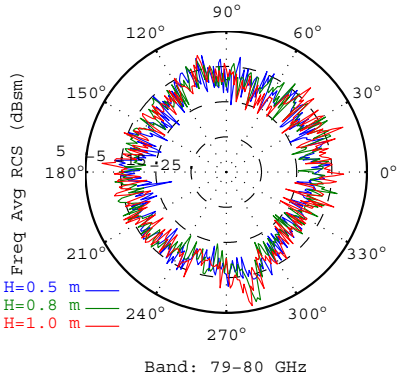

Band: 79-80 GHz

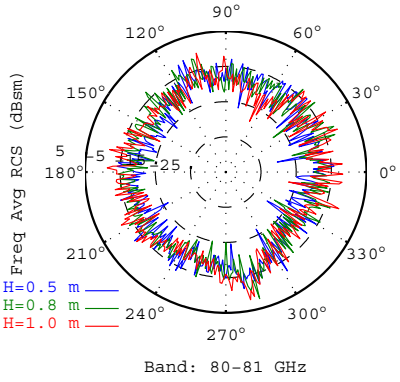

Band: 80-81 GHz

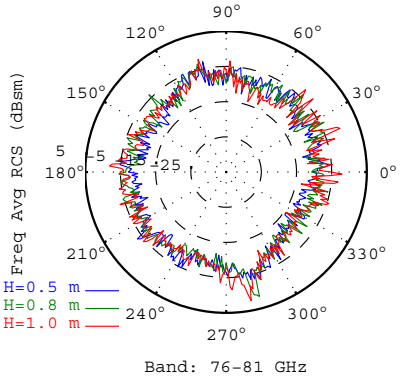

Band: 76-81 GHz

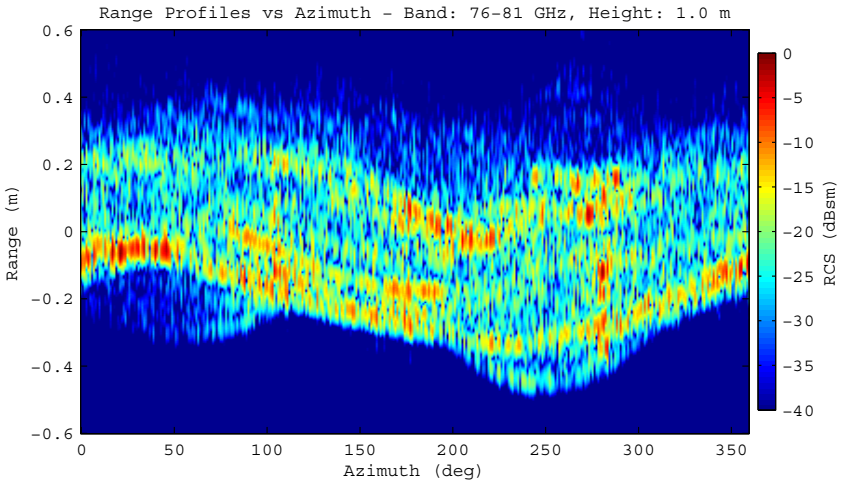

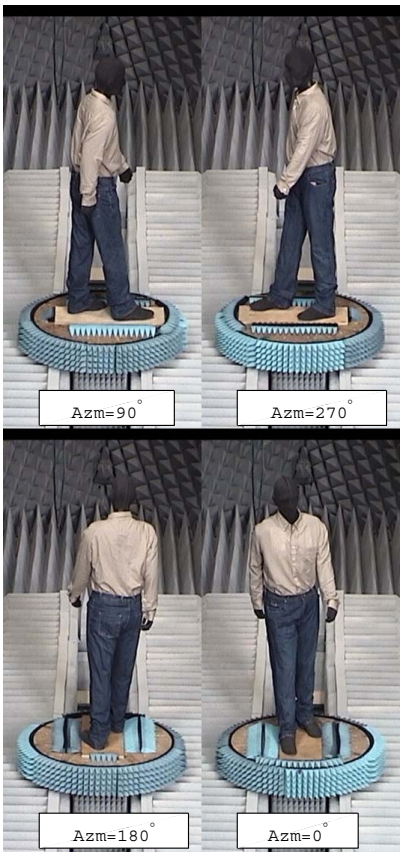

Dummy Type: vFSS Adult

Frequency/Azimuth Average RCS (dBsm)

Band (GHz)	76-77	77-78	78-79	79-80	80-81	76-81
Height=0.5 m	-8.29	-8.33	-8.55	-7.99	-7.94	-8.22
Height=0.8 m	-7.80	-8.27	-7.53	-7.33	-7.26	-7.63
Height=1.0 m	-7.25	-7.34	-7.25	-6.77	-6.70	-7.06

Figure B.6

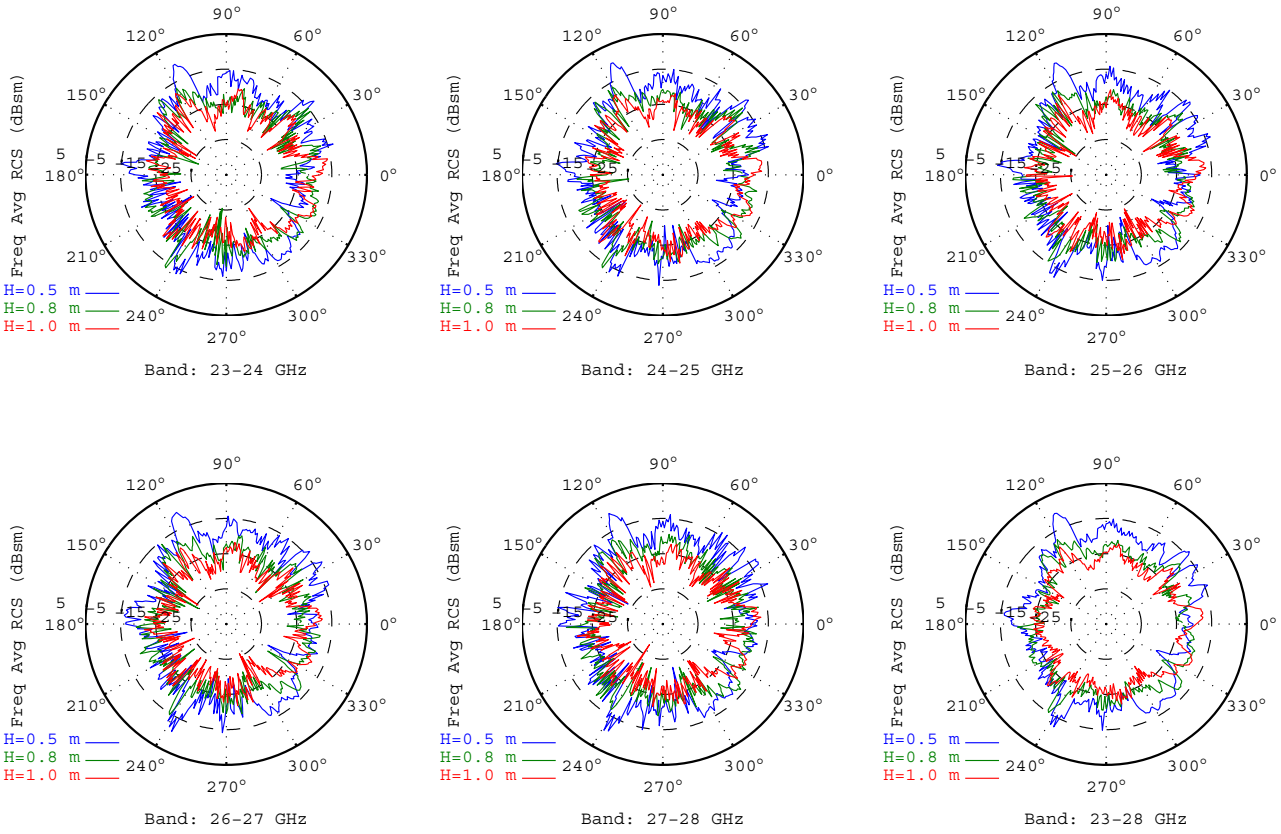

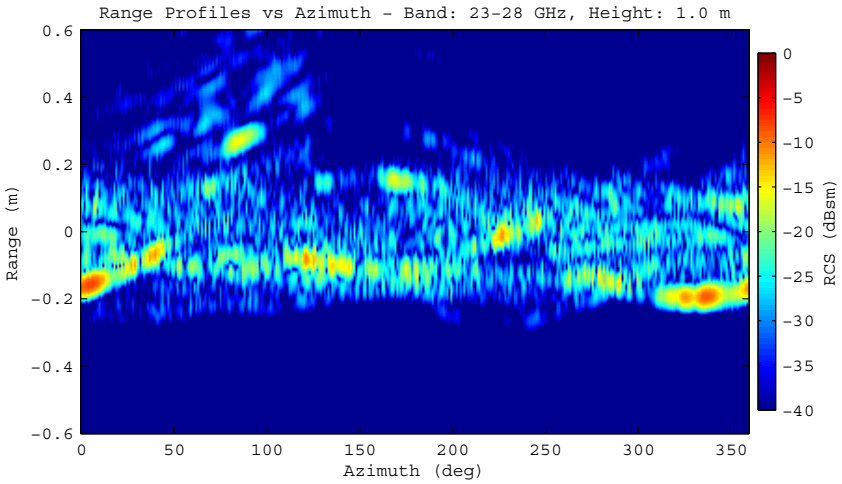

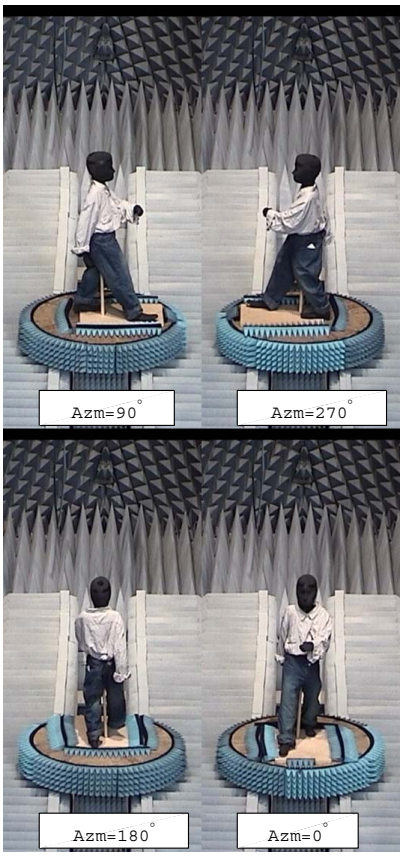

Dummy Type: vFSS Child

Frequency/Azimuth Average RCS (dBsm)

Band (GHz)	23-24	24-25	25-26	26-27	27-28	23-28
Height=0.5 m	-9.25	-9.03	-9.03	-8.58	-8.59	-8.88
Height=0.8 m	-12.01	-12.00	-12.58	-12.47	-12.05	-12.23
Height=1.0 m	-13.56	-13.50	-14.18	-14.60	-14.30	-14.01

Figure B.7

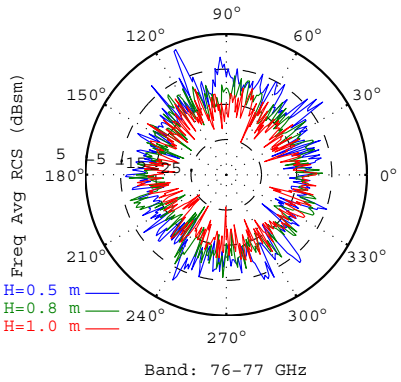

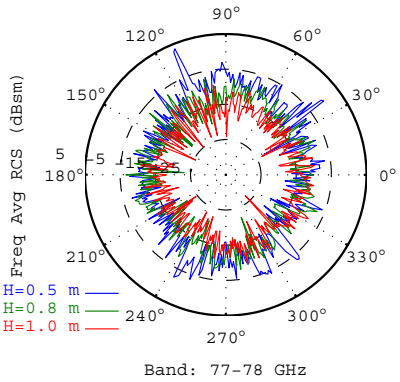

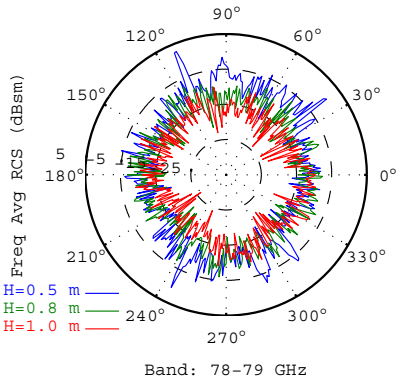

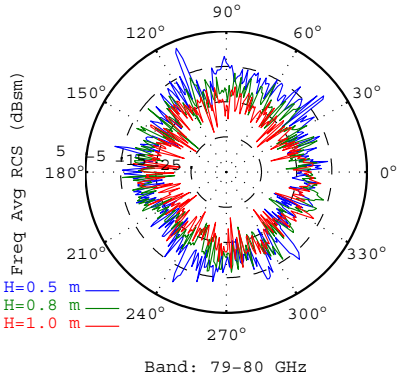

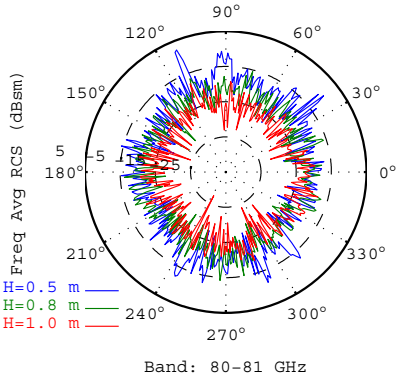

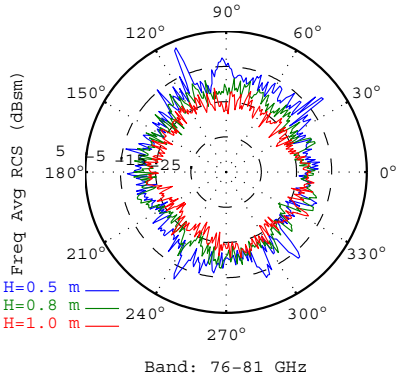

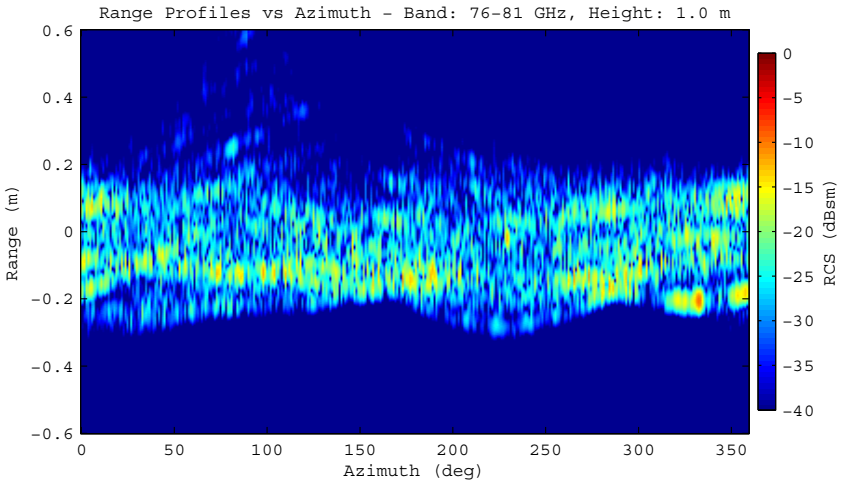

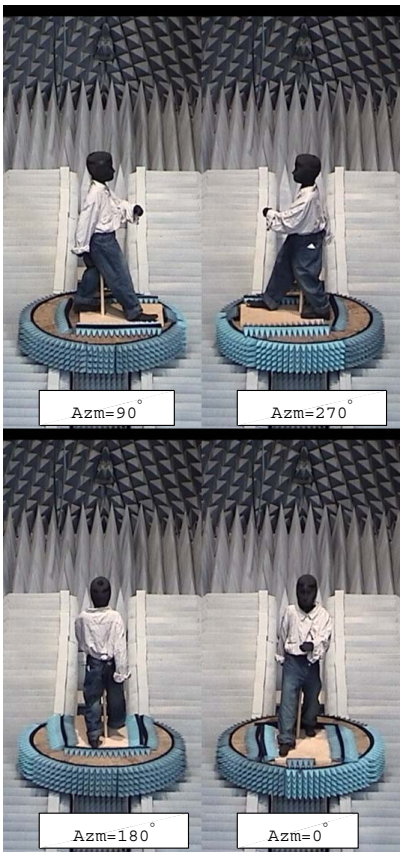

Dummy Type: vFSS Child

Frequency/Azimuth Average RCS (dBsm)

Band (GHz)	76-77	77-78	78-79	79-80	80-81	76-81
Height=0.5 m	-8.80	-8.96	-8.57	-8.31	-8.15	-8.55
Height=0.8 m	-11.97	-12.11	-11.68	-11.33	-11.20	-11.65
Height=1.0 m	-14.47	-14.57	-14.17	-13.81	-14.14	-14.22

Figure B.8

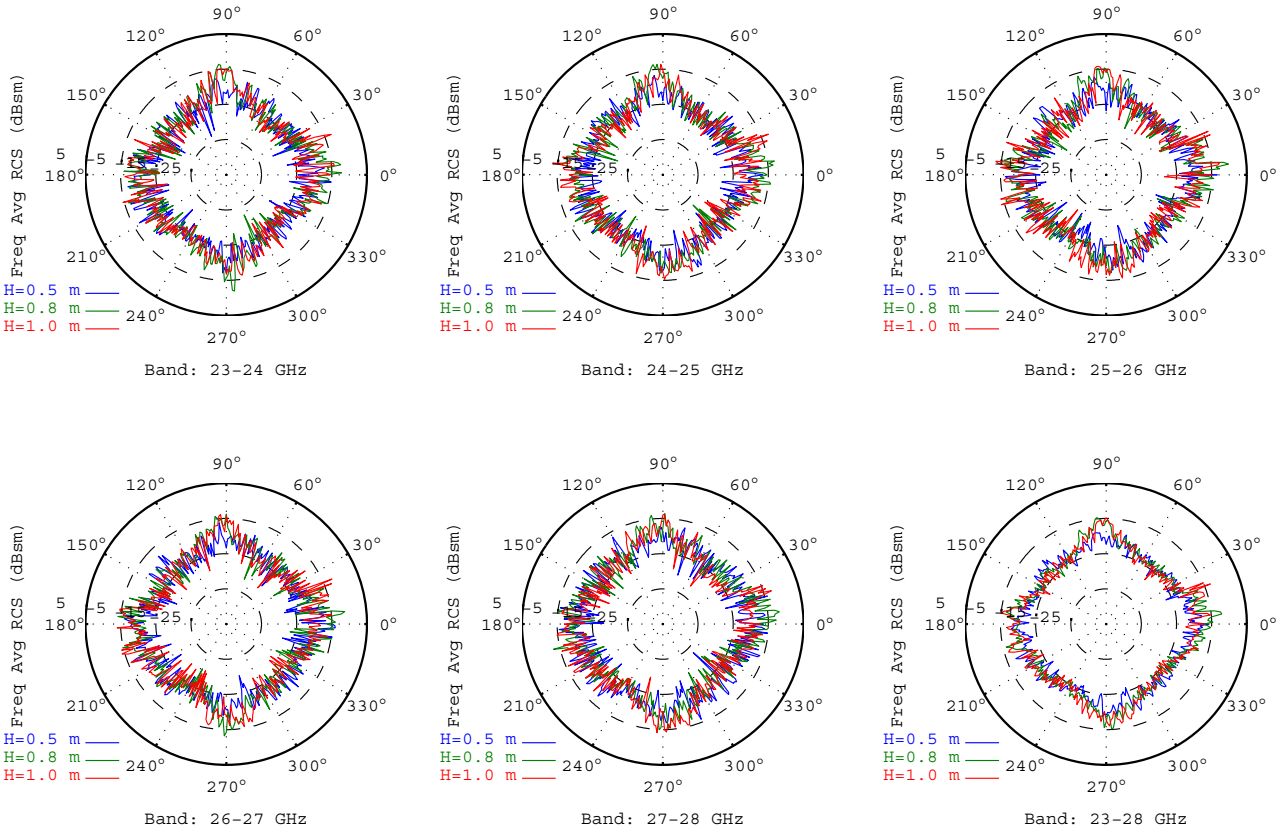

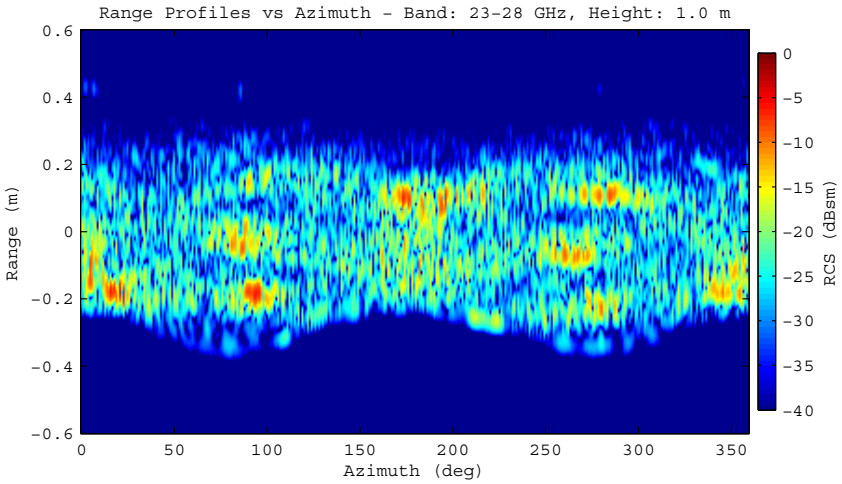

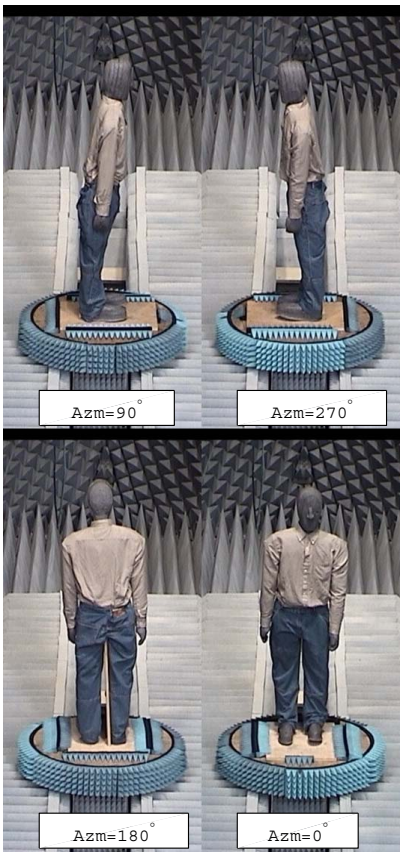

Dummy Type: NHTSA Adult

Frequency/Azimuth Average RCS (dBsm)

Band (GHz)	23-24	24-25	25-26	26-27	27-28	23-28
Height=0.5 m	-12.31	-12.17	-12.19	-11.50	-10.84	-11.78
Height=0.8 m	-10.48	-10.60	-10.55	-10.14	-10.05	-10.36
Height=1.0 m	-11.18	-10.90	-10.43	-10.33	-10.26	-10.60

Figure B.9

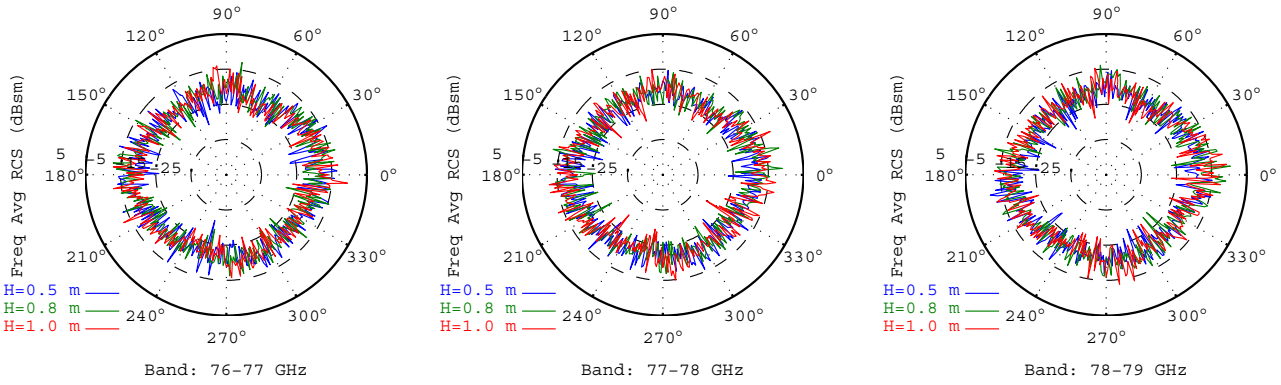

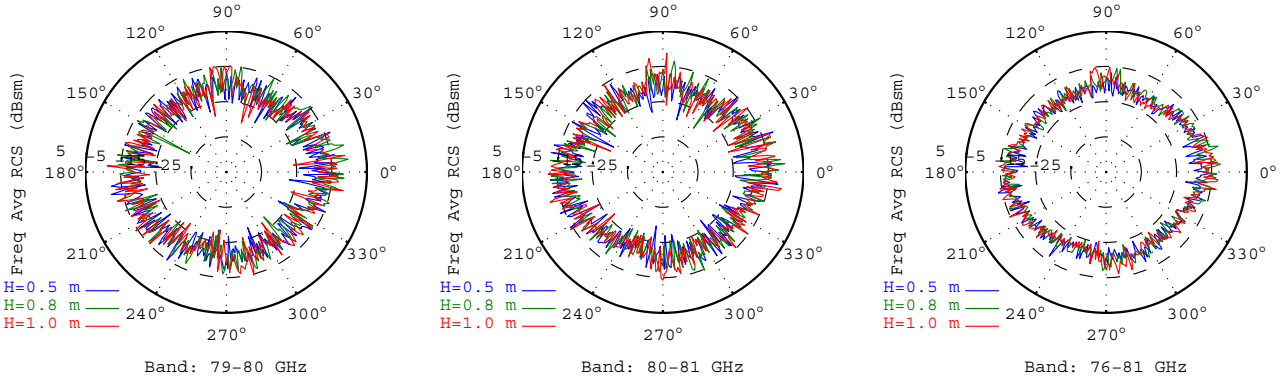

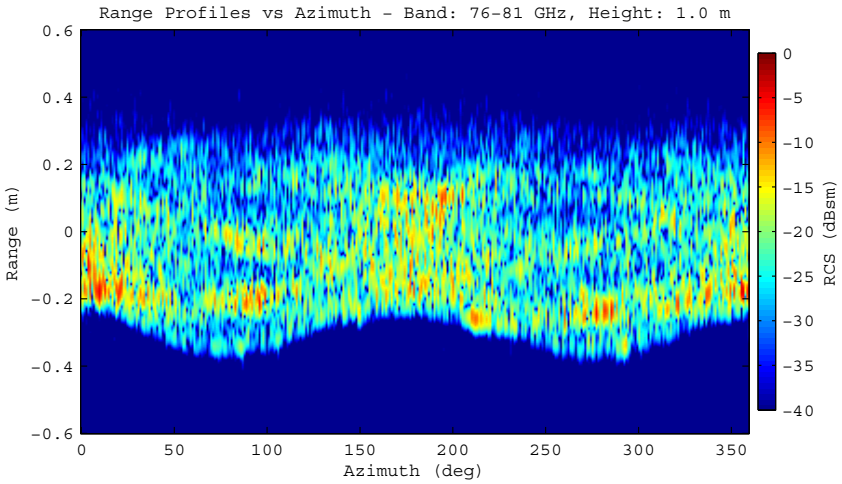

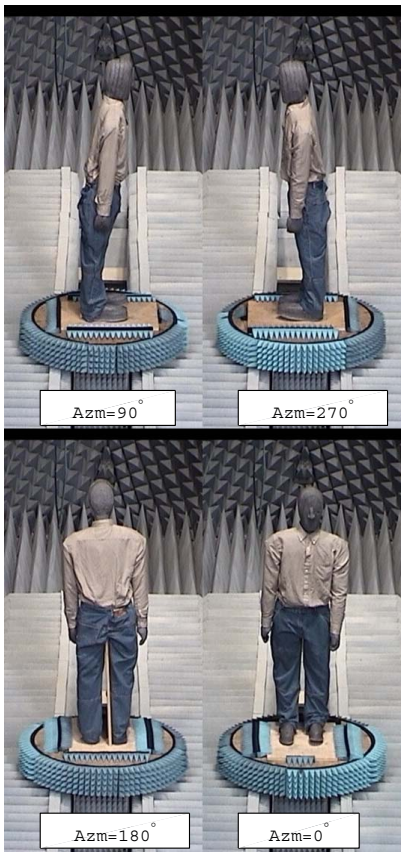

Dummy Type: NHTSA Adult

Frequency/Azimuth Average RCS (dBsm)

Band (GHz)	76-77	77-78	78-79	79-80	80-81	76-81
Height=0.5 m	-9.72	-10.22	-9.90	-9.31	-9.27	-9.68
Height=0.8 m	-9.59	-9.59	-8.84	-8.56	-8.73	-9.04
Height=1.0 m	-9.51	-9.26	-8.89	-8.75	-8.30	-8.92

Figure B.10

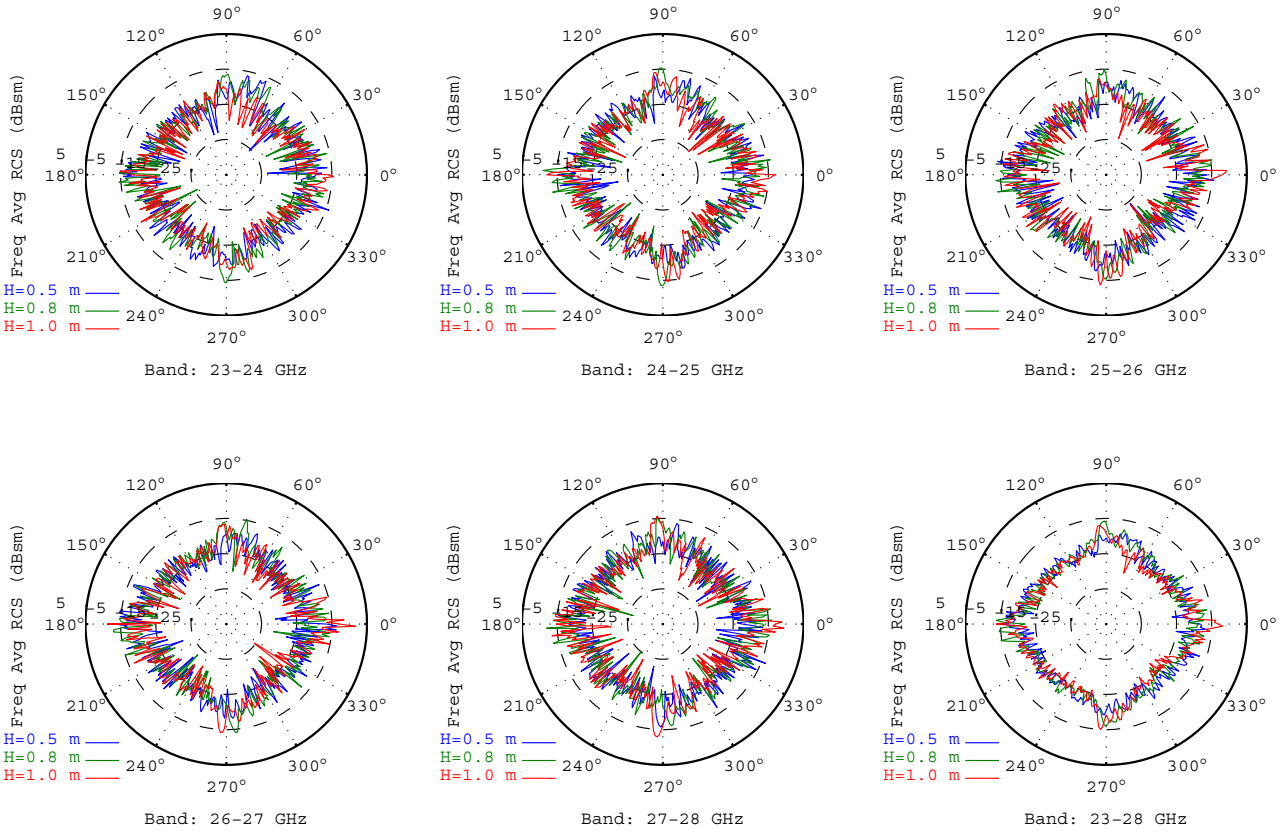

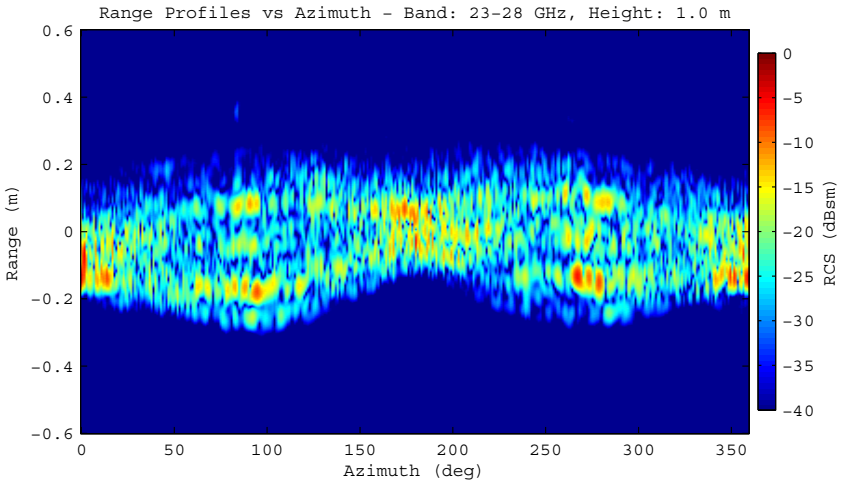

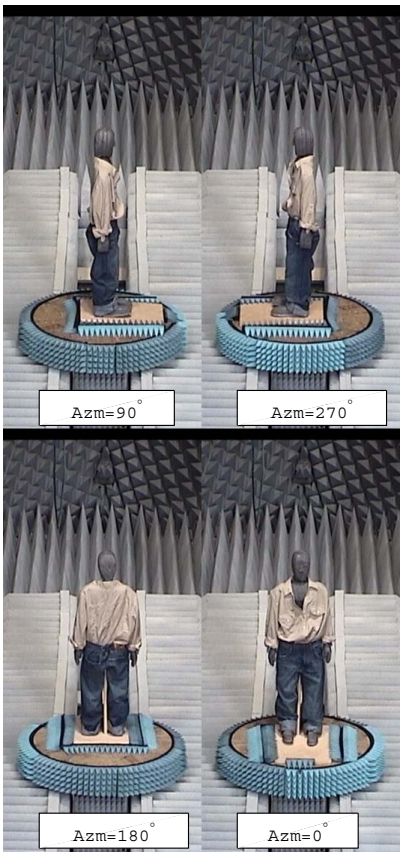

Dummy Type: NHTSA Child

Frequency/Azimuth Average RCS (dBsm)

Band (GHz)	23-24	24-25	25-26	26-27	27-28	23-28
Height=0.5 m	-11.89	-11.75	-11.66	-11.67	-11.62	-11.72
Height=0.8 m	-11.60	-10.99	-11.47	-11.00	-10.86	-11.17
Height=1.0 m	-12.49	-11.46	-11.39	-11.20	-10.75	-11.42

Figure B.11

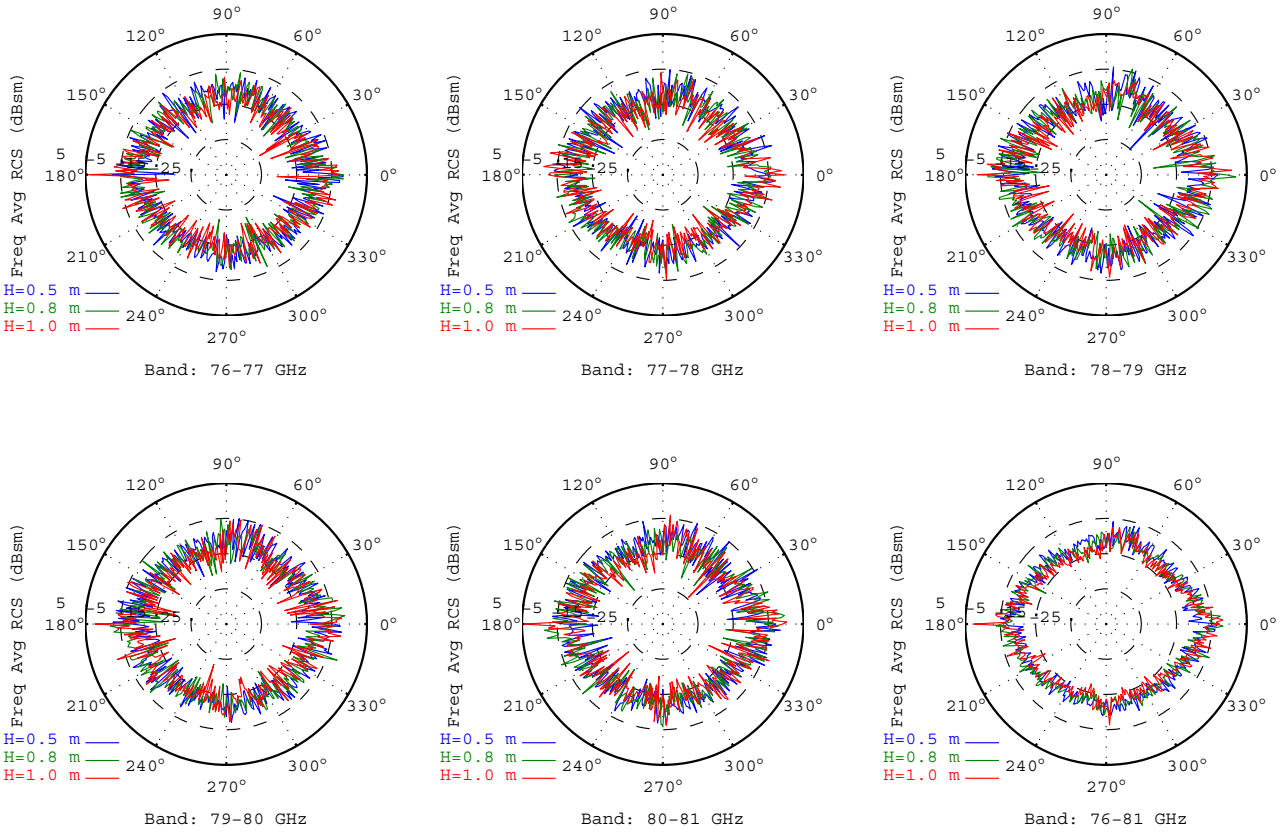

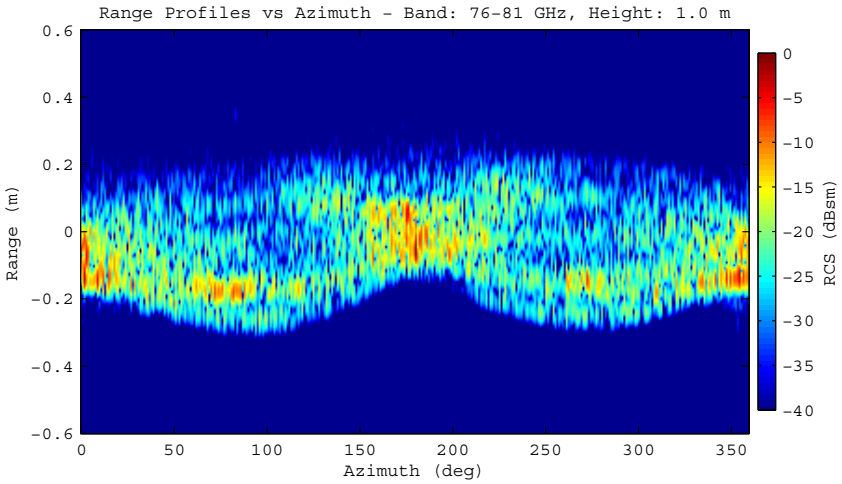

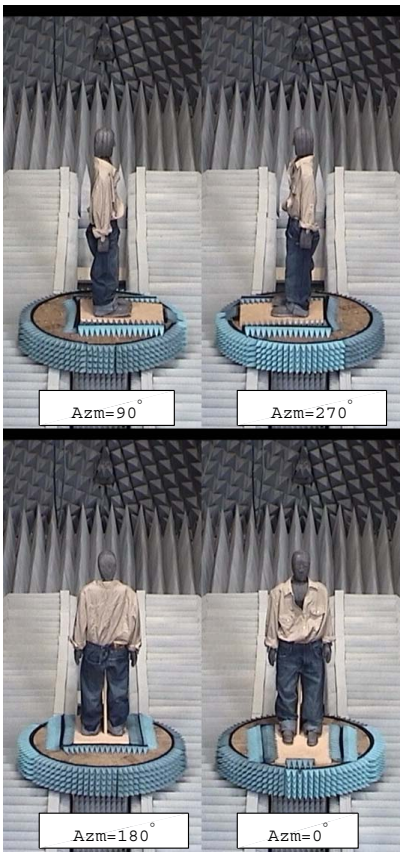

Dummy Type: NHTSA Child

Frequency/Azimuth Average RCS (dBsm)

Band (GHz)	76-77	77-78	78-79	79-80	80-81	76-81
Height=0.5 m	-10.27	-10.35	-9.87	-9.82	-9.74	-10.00
Height=0.8 m	-10.30	-10.57	-9.40	-9.66	-9.51	-9.86
Height=1.0 m	-10.45	-10.64	-10.10	-10.26	-9.82	-10.25

Figure B.12

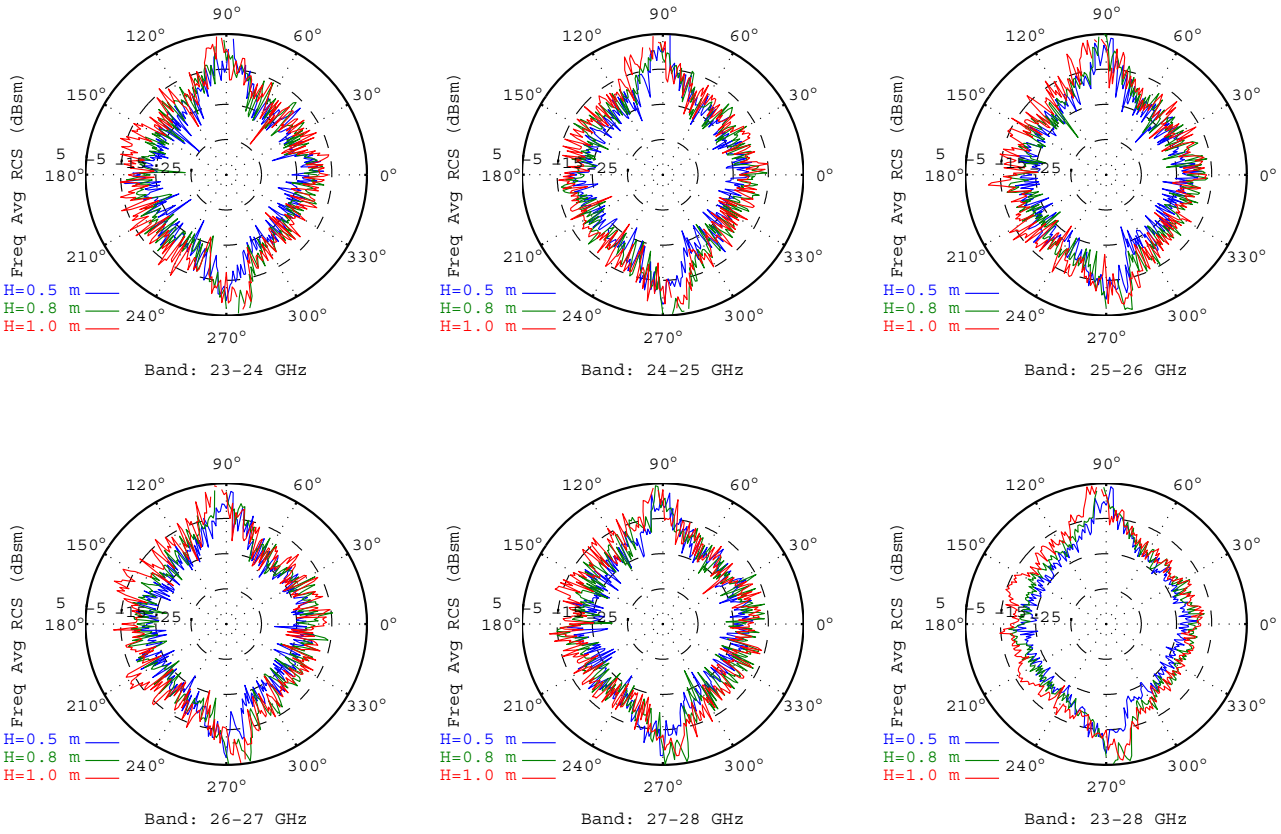

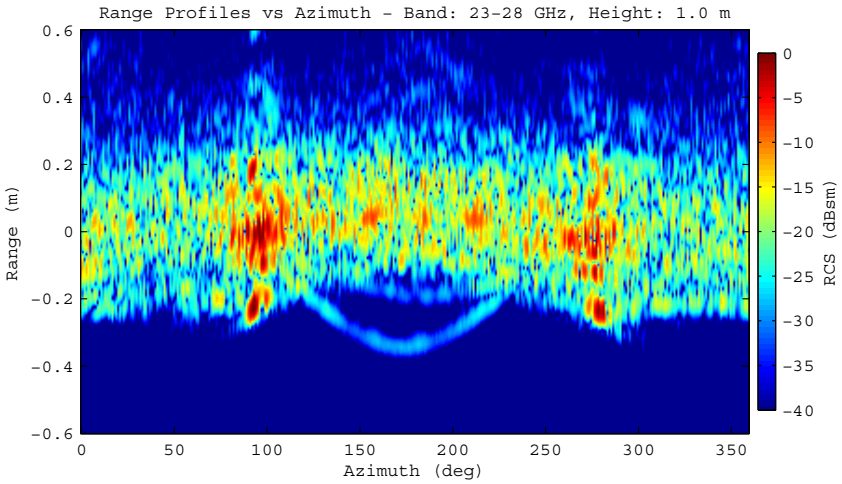

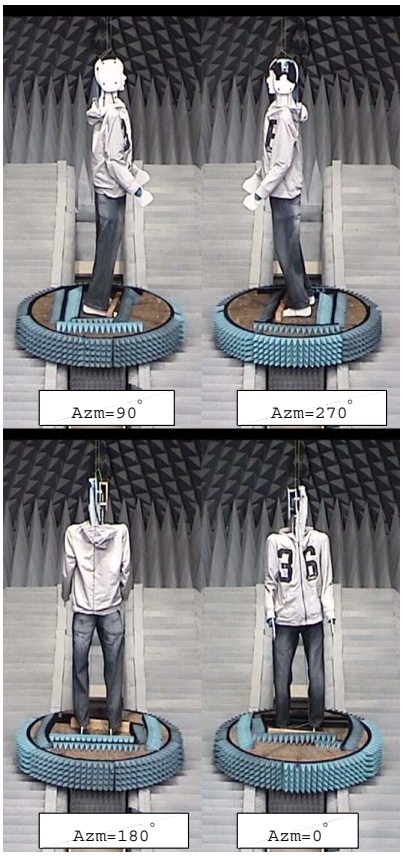

Dummy Type: IIHS Adult

Frequency/Azimuth Average RCS (dBsm)

Band (GHz)	23-24	24-25	25-26	26-27	27-28	23-28
Height=0.5 m	-9.43	-8.61	-8.92	-9.26	-9.06	-9.04
Height=0.8 m	-6.11	-6.05	-5.81	-5.98	-7.06	-6.16
Height=1.0 m	-6.17	-5.75	-5.72	-5.43	-6.52	-5.88

Figure B.13

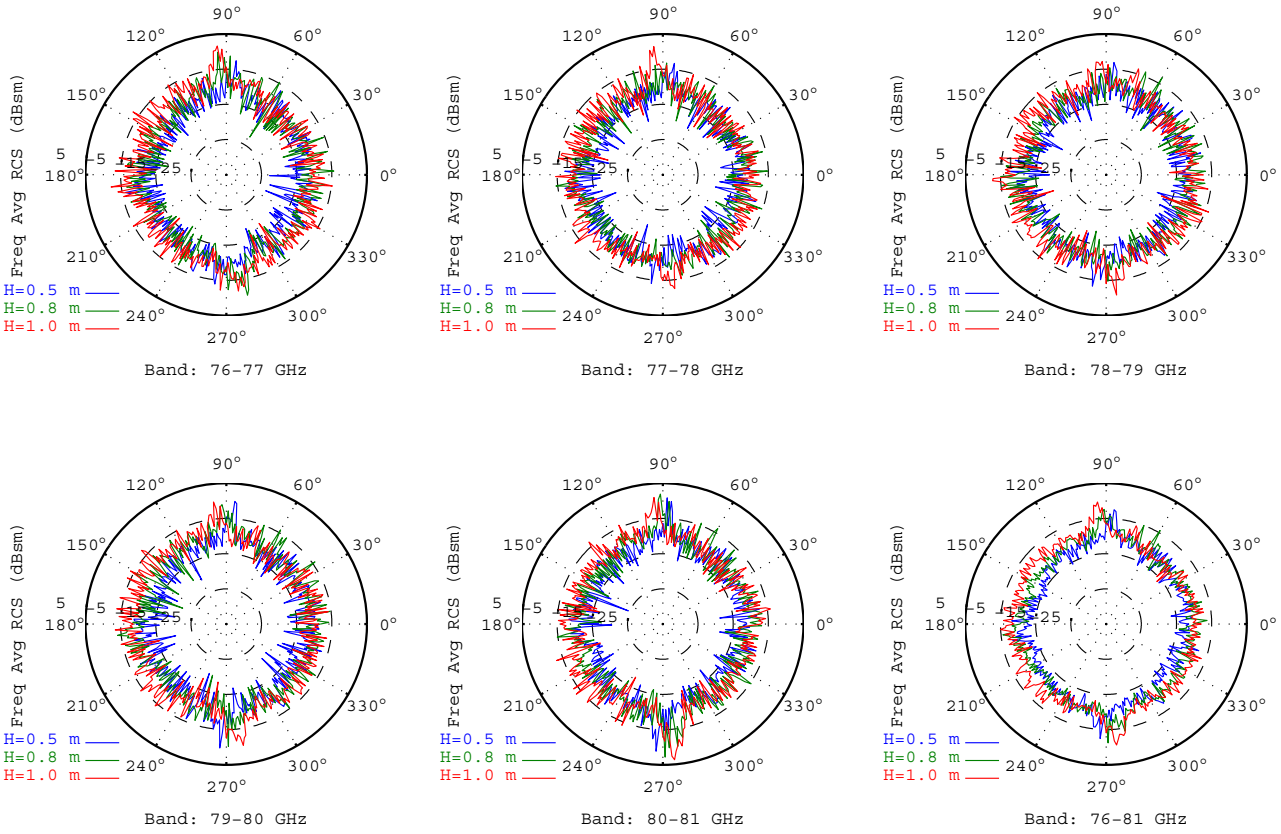

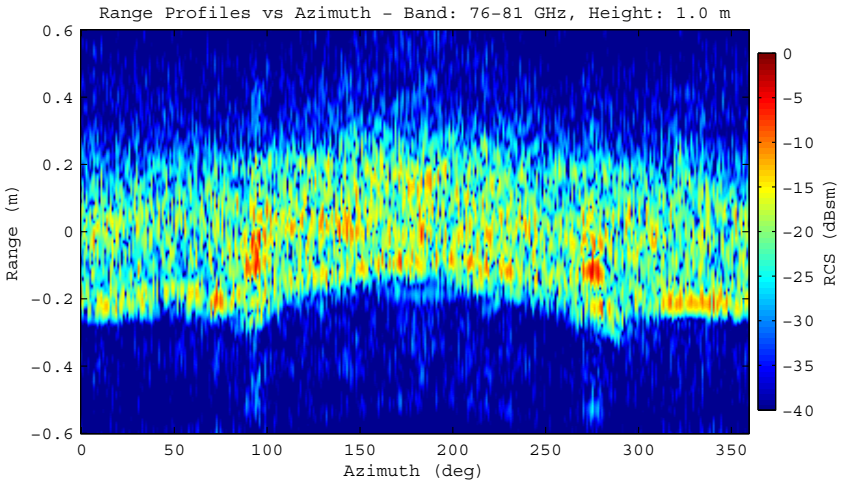

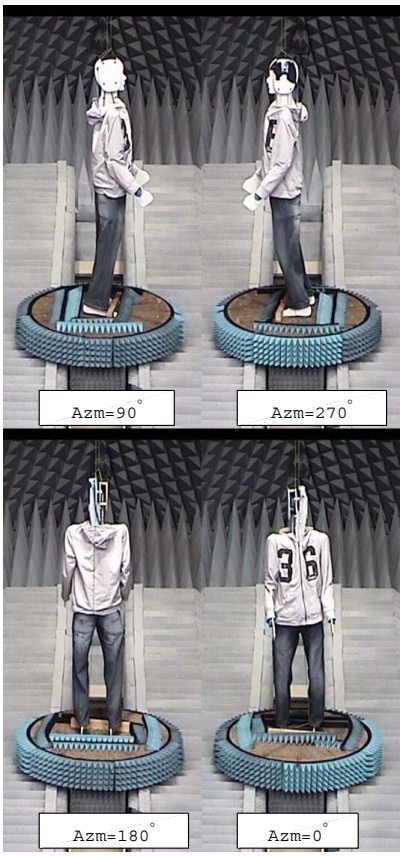

Dummy Type: IIHS Adult

Frequency/Azimuth Average RCS (dBsm)

Band (GHz)	76-77	77-78	78-79	79-80	80-81	76-81
Height=0.5 m	-11.33	-11.69	-11.34	-10.66	-10.47	-11.08
Height=0.8 m	-9.69	-10.43	-10.21	-9.24	-8.89	-9.67
Height=1.0 m	-8.13	-8.76	-8.59	-8.11	-7.81	-8.28

Figure B.14

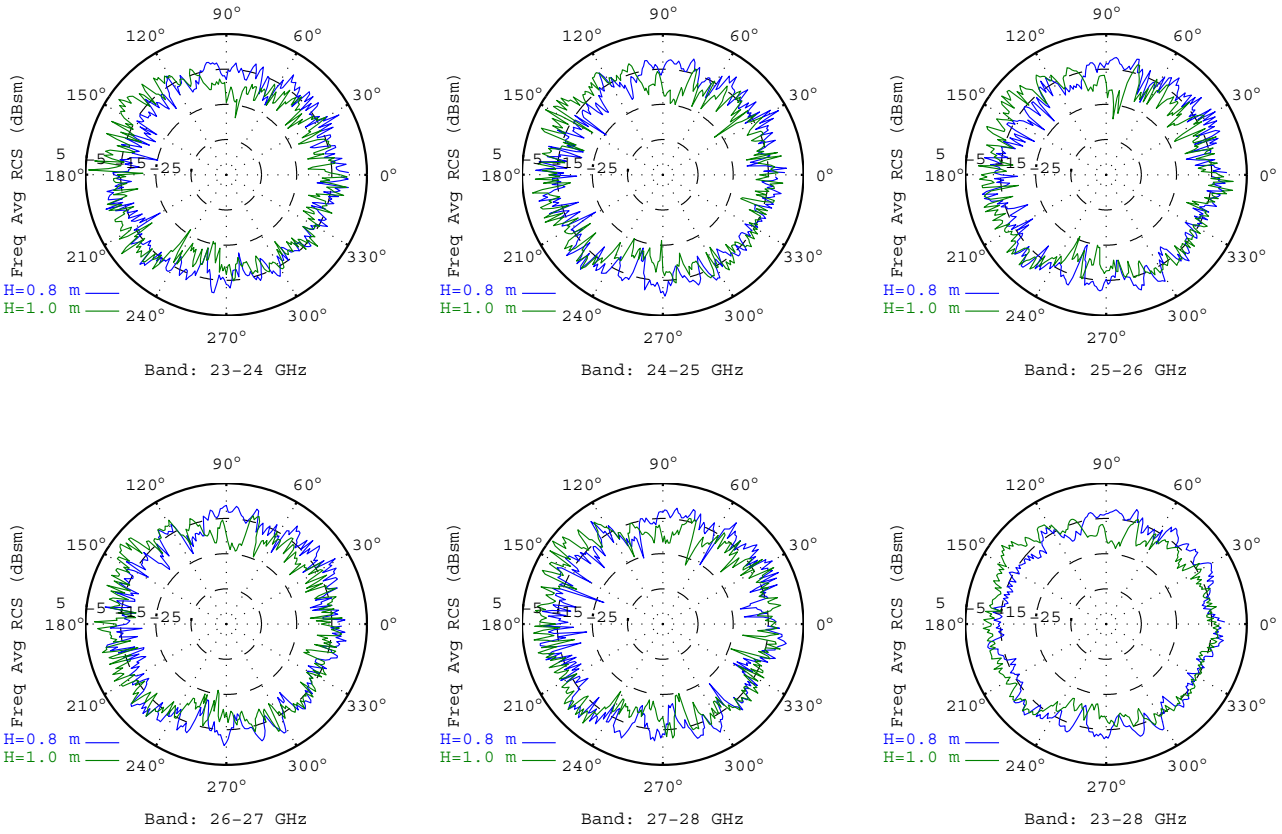

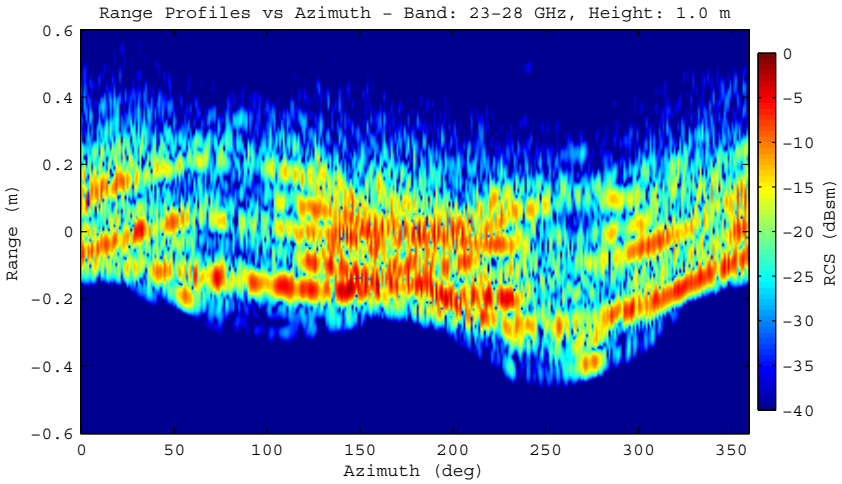

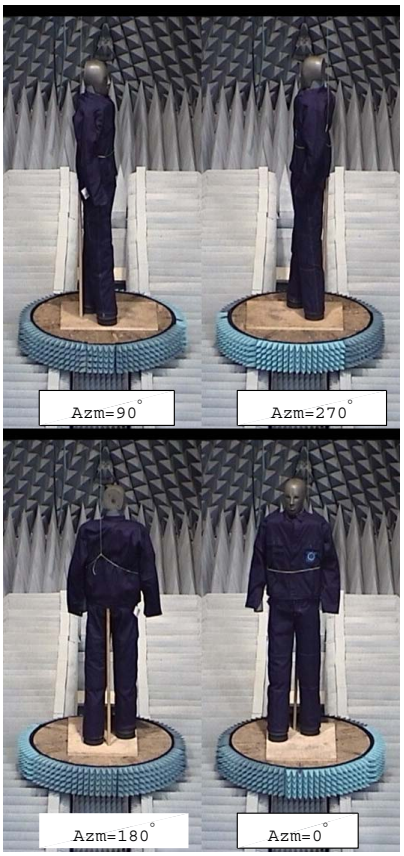

Dummy Type: TRL/innovITS Advance Adult

Frequency/Azimuth Average RCS (dBsm)

Band (GHz)	23-24	24-25	25-26	26-27	27-28	23-28
Height=0.8 m	-4.84	-4.24	-4.12	-4.10	-3.84	-4.21
Height=1.0 m	-4.85	-4.40	-4.12	-4.37	-3.79	-4.29

Figure B.15

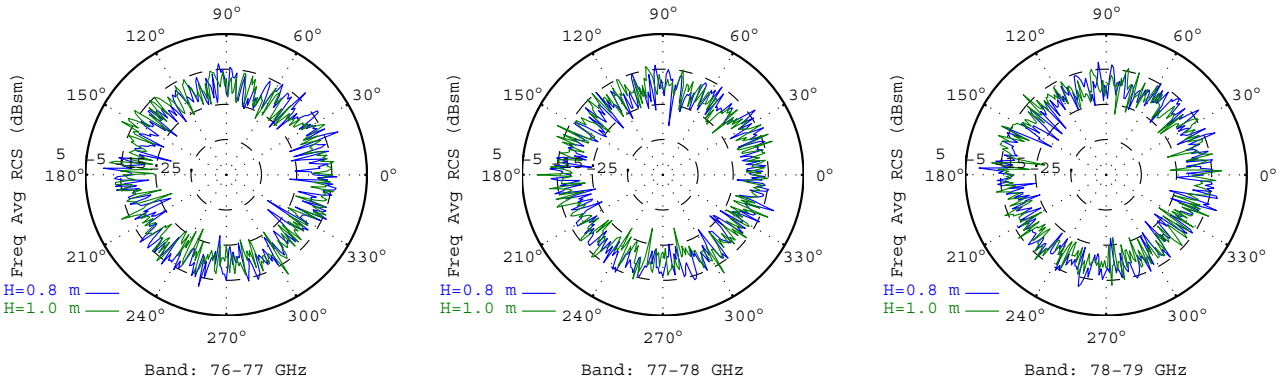

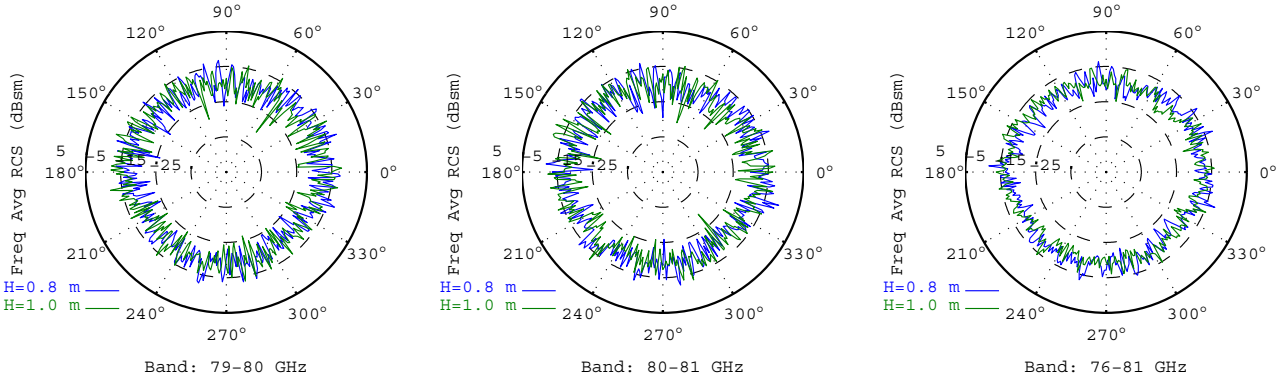

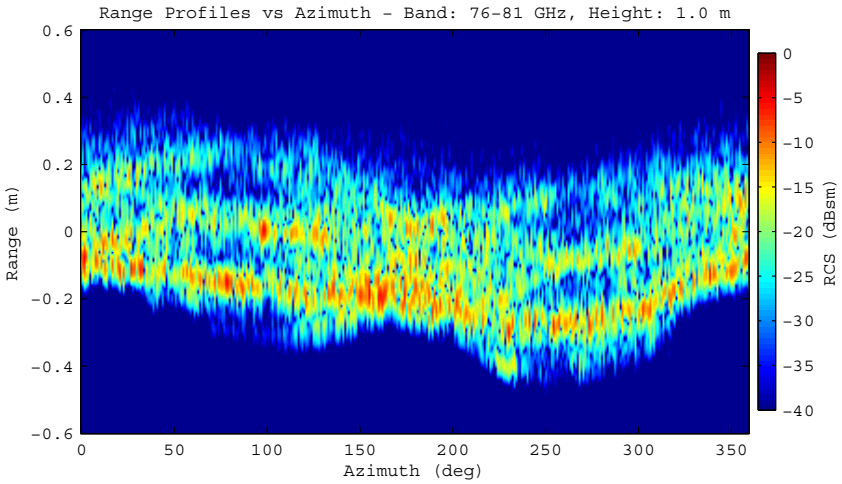

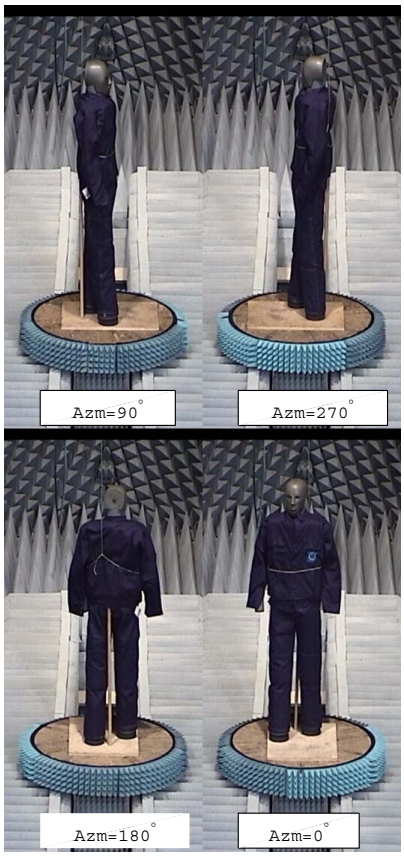

Dummy Type: TRL/innovITS Advance Adult

Frequency/Azimuth Average RCS (dBsm)

Band (GHz)	76-77	77-78	78-79	79-80	80-81	76-81
Height=0.8 m	-8.05	-8.38	-7.86	-7.74	-7.64	-7.93
Height=1.0 m	-8.14	-8.33	-8.09	-7.82	-7.98	-8.07

Figure B.16

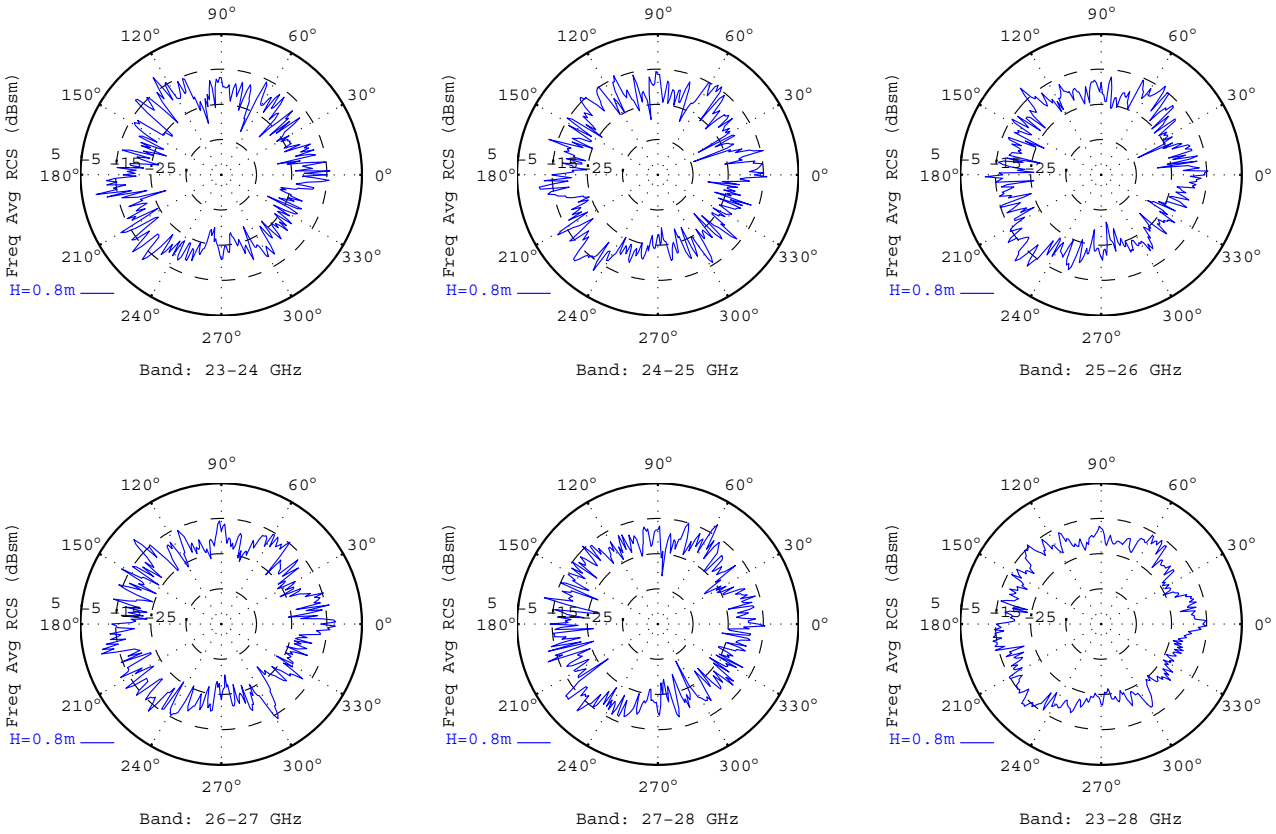

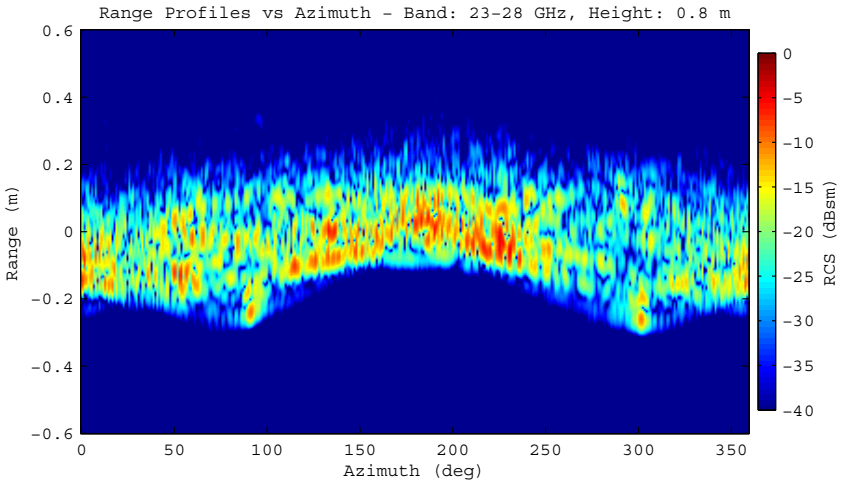

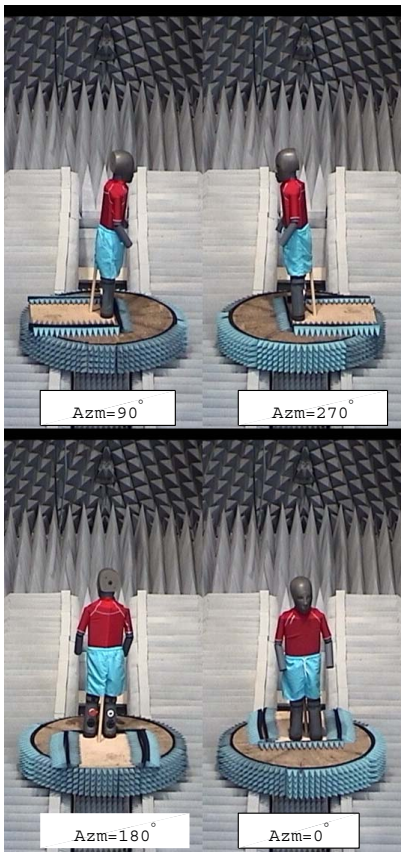

Dummy Type: TRL/innovITS ADVANCE Child

Frequency/Azimuth Average RCS (dBsm)

Band (GHz)	23-24	24-25	25-26	26-27	27-28	23-28
Height=0.8m	-9.35	-8.89	-9.11	-8.47	-8.97	-8.94

Figure B.17

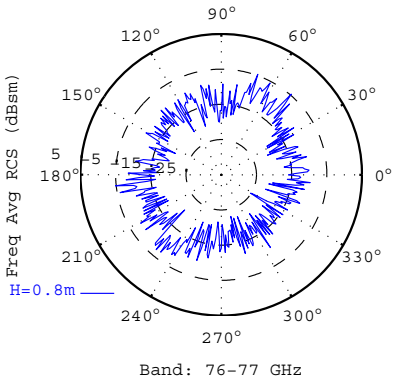

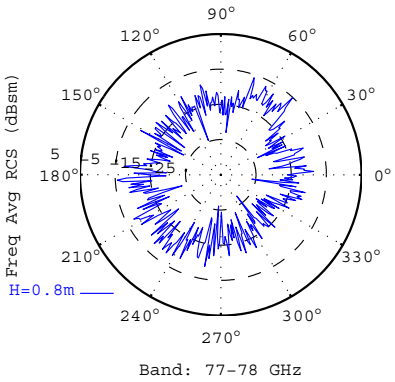

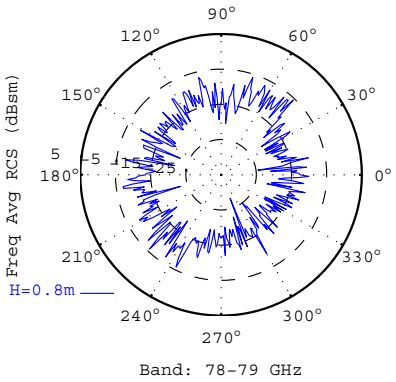

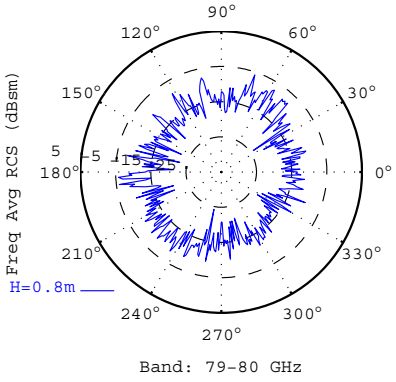

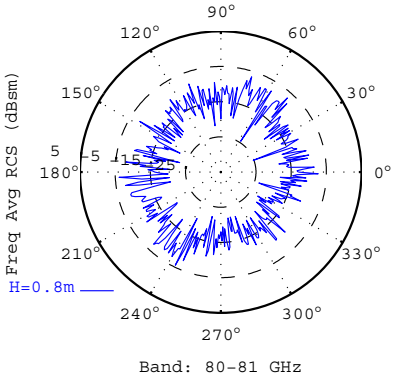

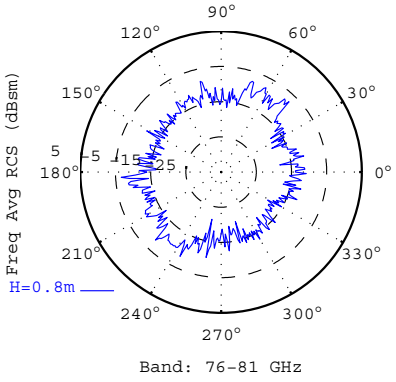

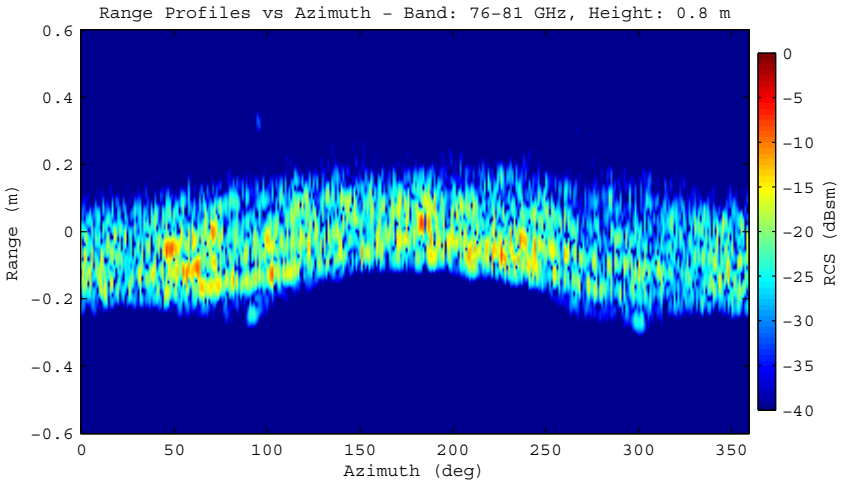

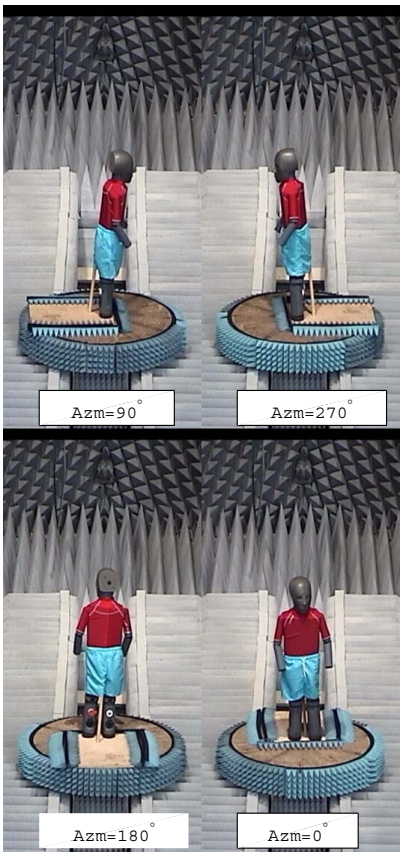

Dummy Type: TRL/innovITS ADVANCE Child

Frequency/Azimuth Average RCS (dBsm)

Band (GHz)	76-77	77-78	78-79	79-80	80-81	76-81
Height=0.8m	-12.74	-13.18	-12.78	-12.95	-12.87	-12.91

Figure B.18

C RCS Signatures of Pedestrians: Measurement Group II

The captions of the figures included in this annex is provided here due to formatting constraints. The complete list of captions is shown in Table C.1.

Table C.1: List of captions for the figures with the RCS signatures of measurement group II.

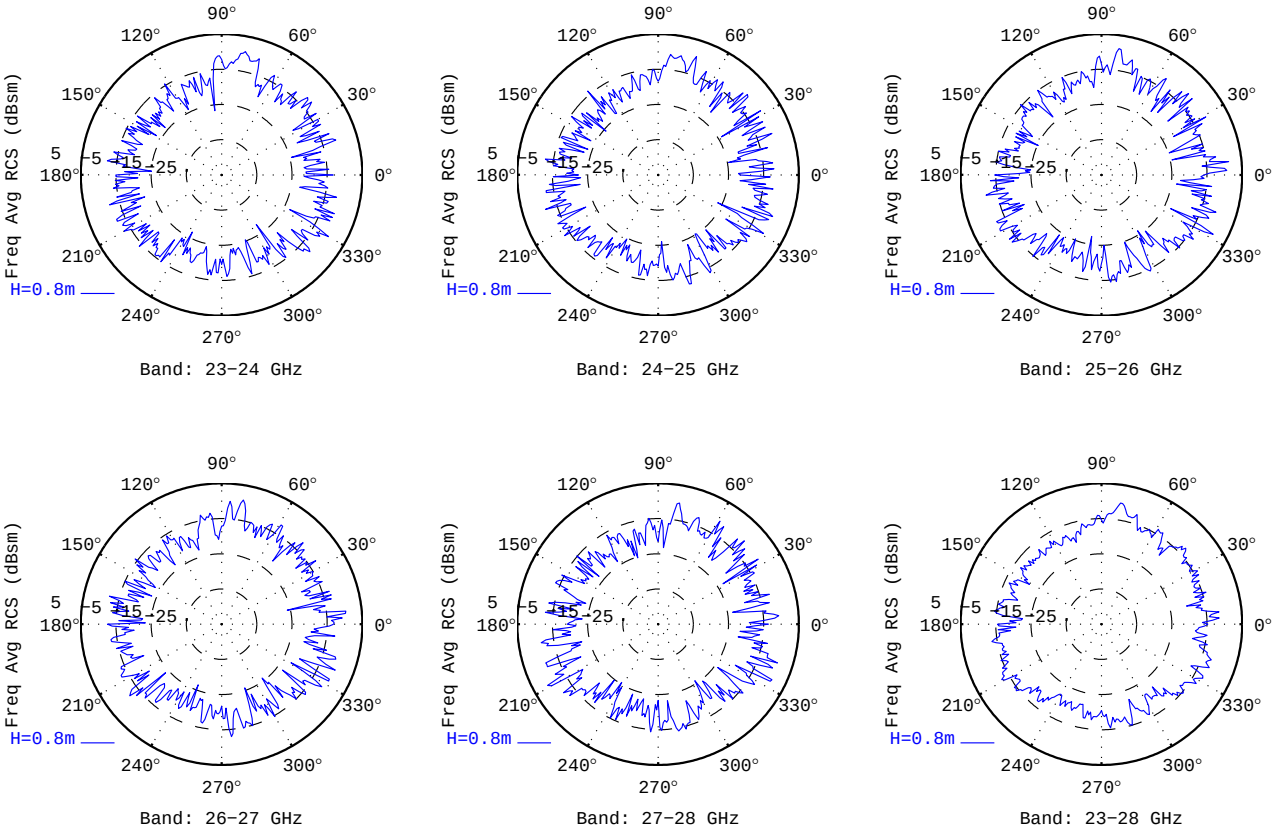

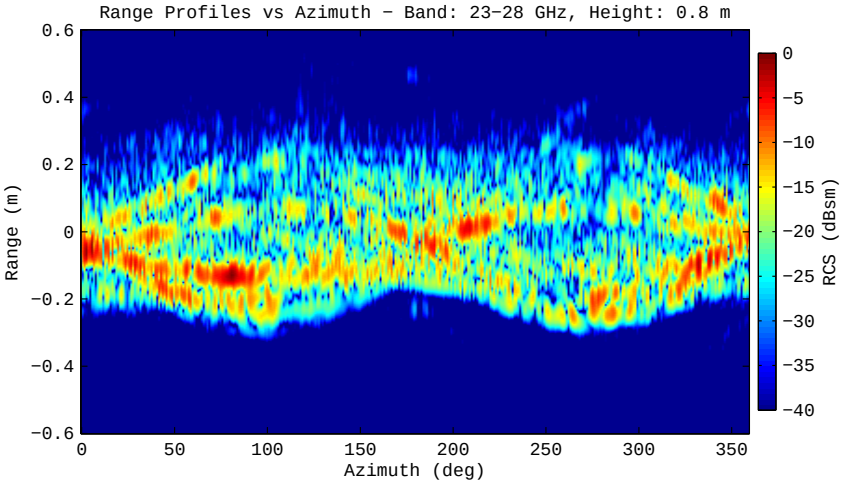

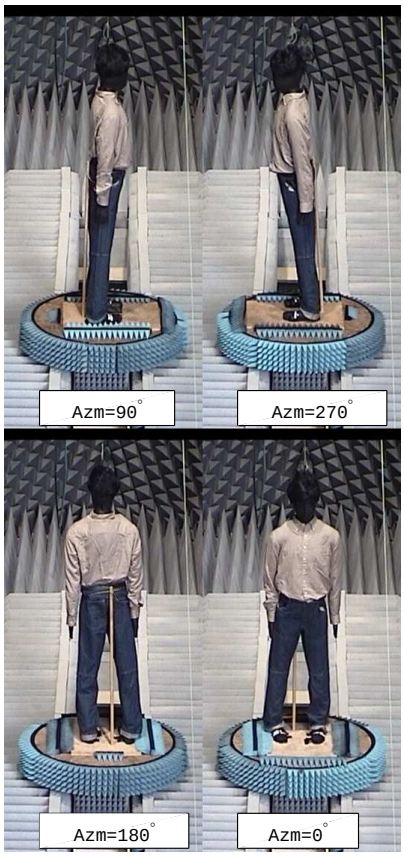

Dummy Type: IDIADA Standing Position

Frequency/Azimuth Average RCS (dBsm)

Band (GHz)	23–24	24–25	25–26	26–27	27–28	23–28
Height=0.8m	-6.21	-6.20	-6.07	-6.13	-6.16	-6.15

Figure C.1

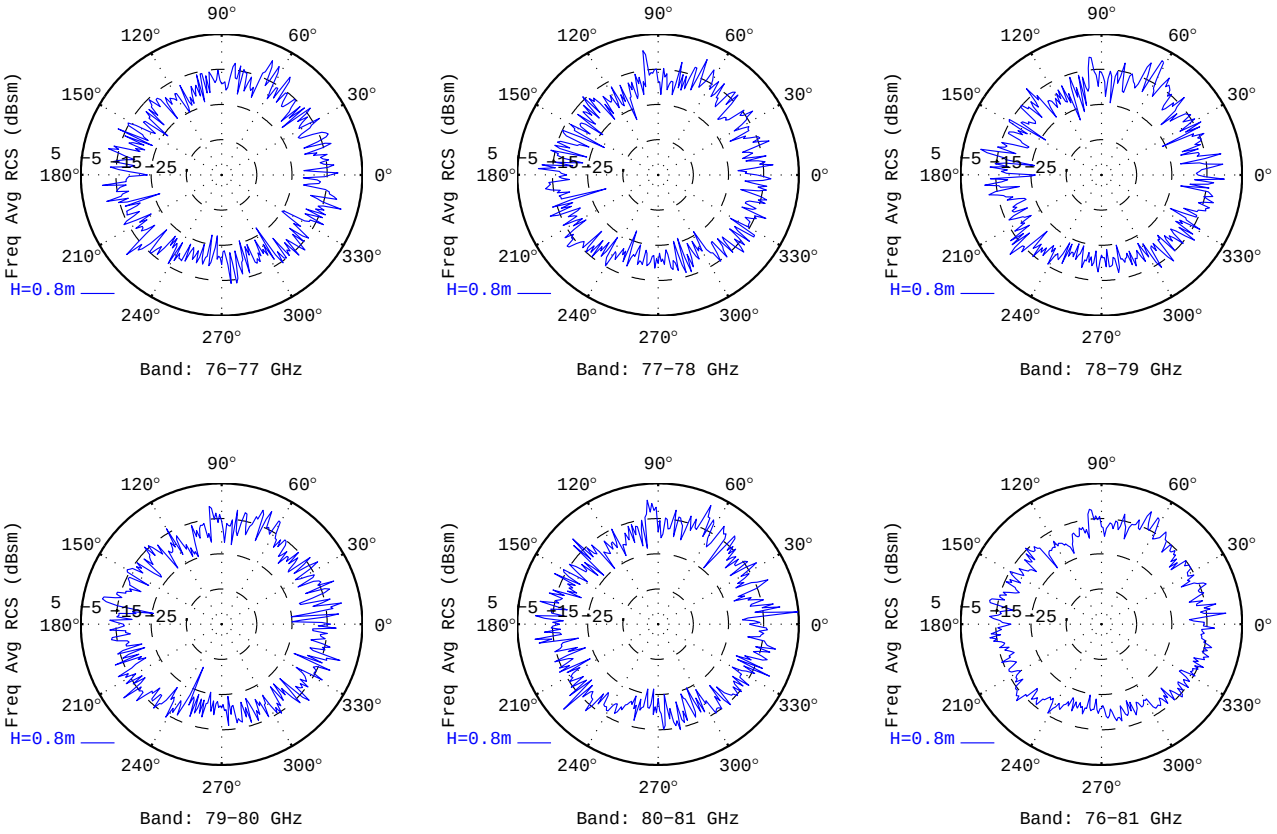

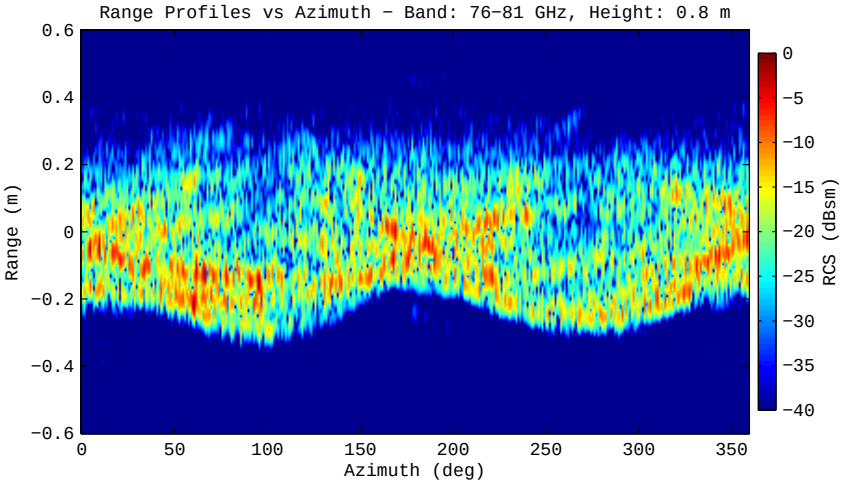

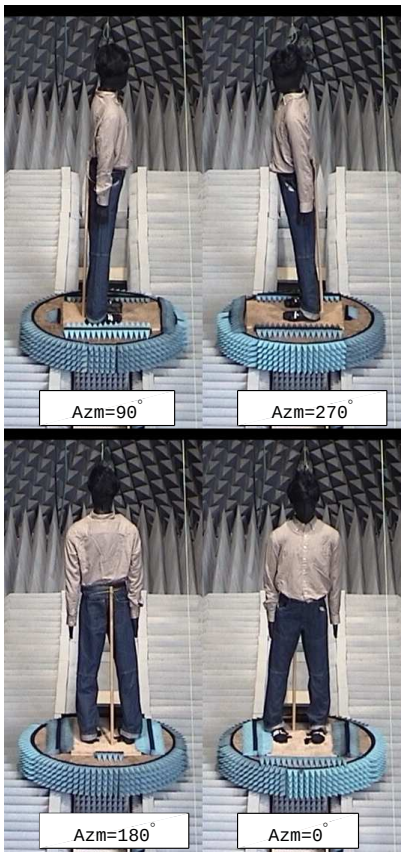

Dummy Type: IDIADA Standing Position

Frequency/Azimuth Average RCS (dBsm)

Band (GHz)	76–77	77–78	78–79	79–80	80–81	76–81
Height=0.8m	-6.81	-6.76	-6.61	-6.27	-5.84	-6.45

Figure C.2

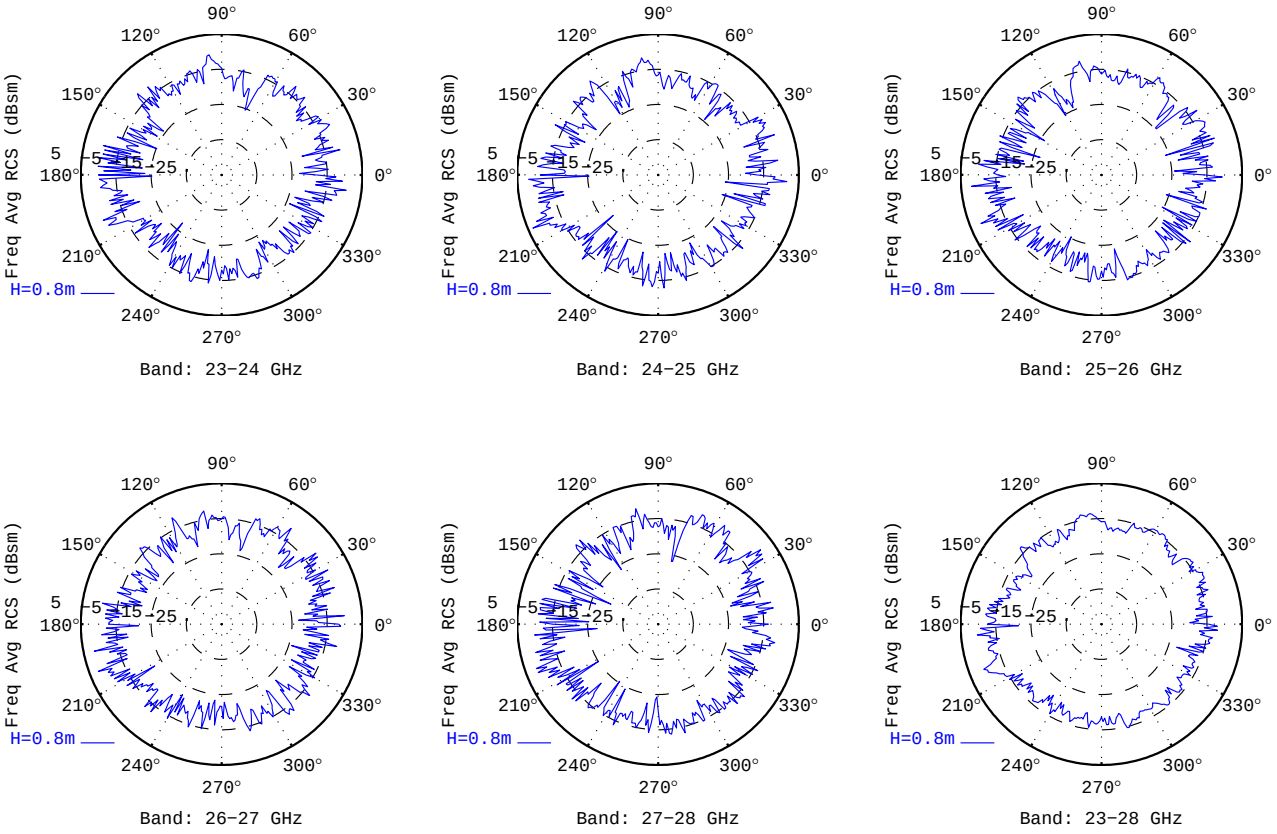

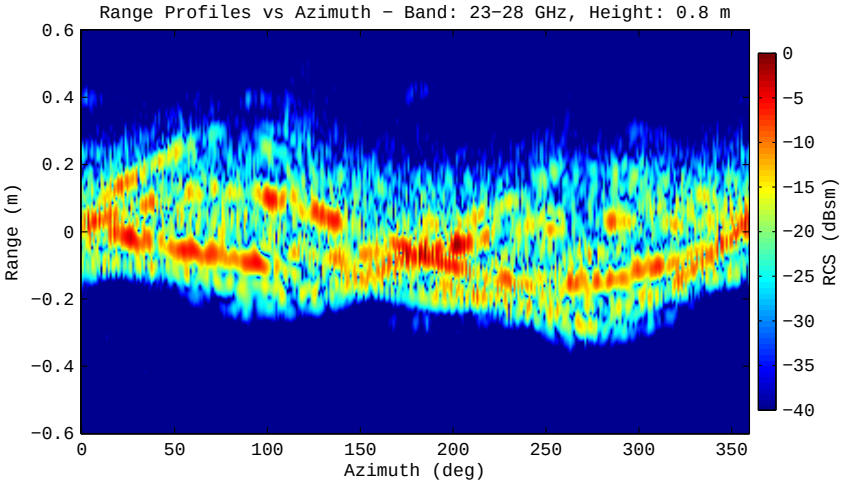

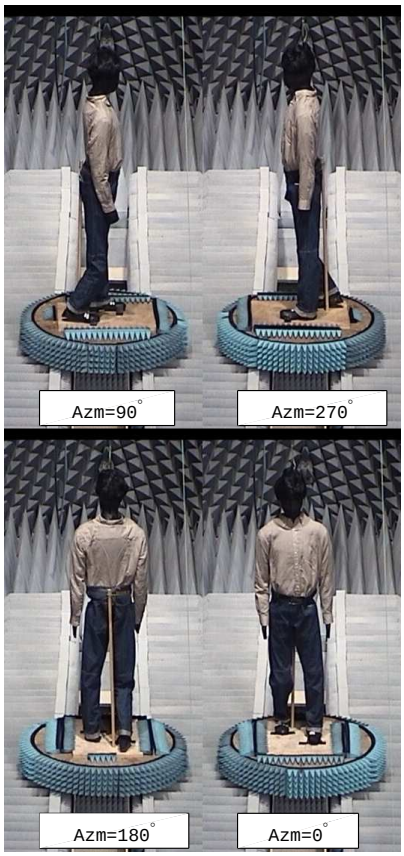

Dummy Type: IDIADA ISw Position

Frequency/Azimuth Average RCS (dBsm)

Band (GHz)	23–24	24–25	25–26	26–27	27–28	23–28
Height=0.8m	-5.67	-5.45	-6.02	-5.78	-5.32	-5.65

Figure C.3

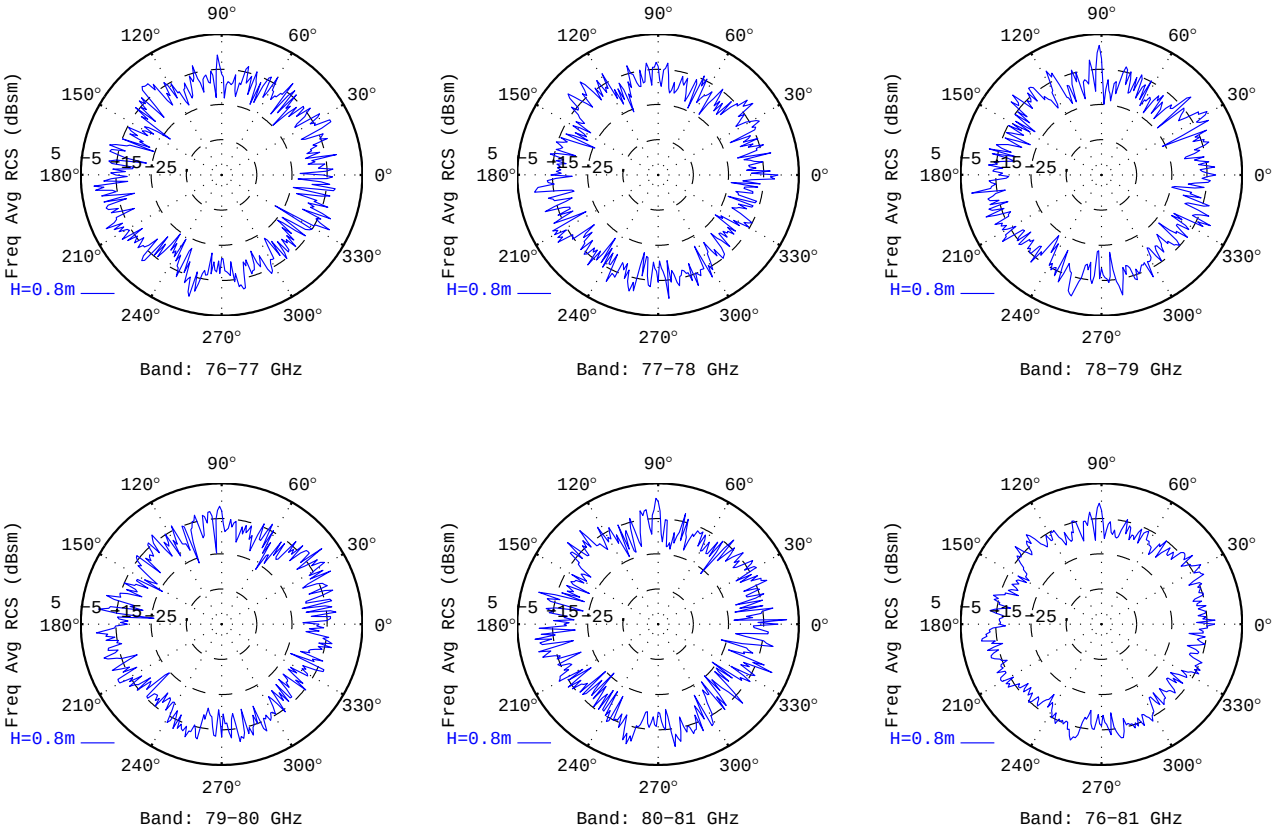

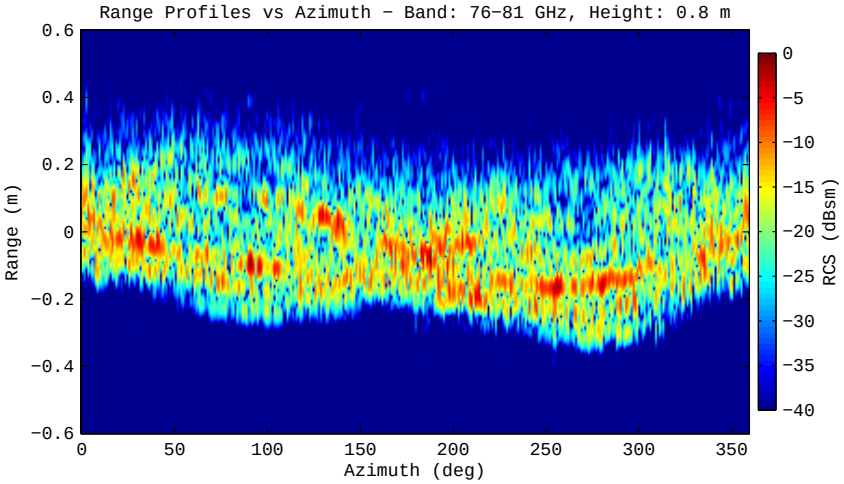

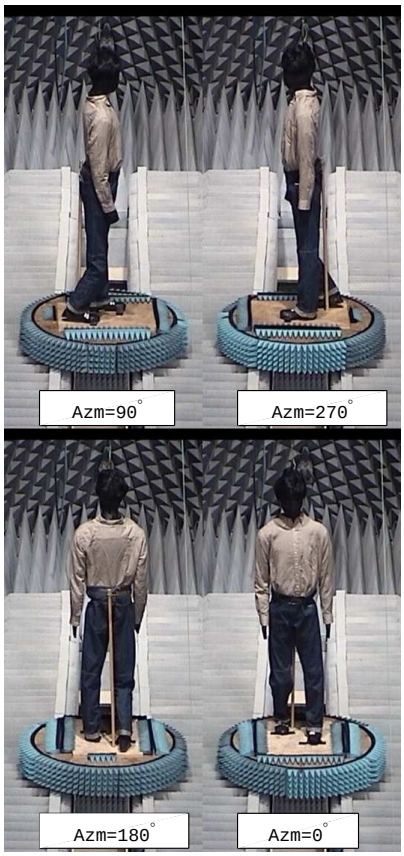

Dummy Type: IDIADA ISw Position

Frequency/Azimuth Average RCS (dBsm)

Band (GHz)	76–77	77–78	78–79	79–80	80–81	76–81
Height=0.8m	-5.55	-5.92	-5.59	-5.51	-5.63	-5.64

Figure C.4

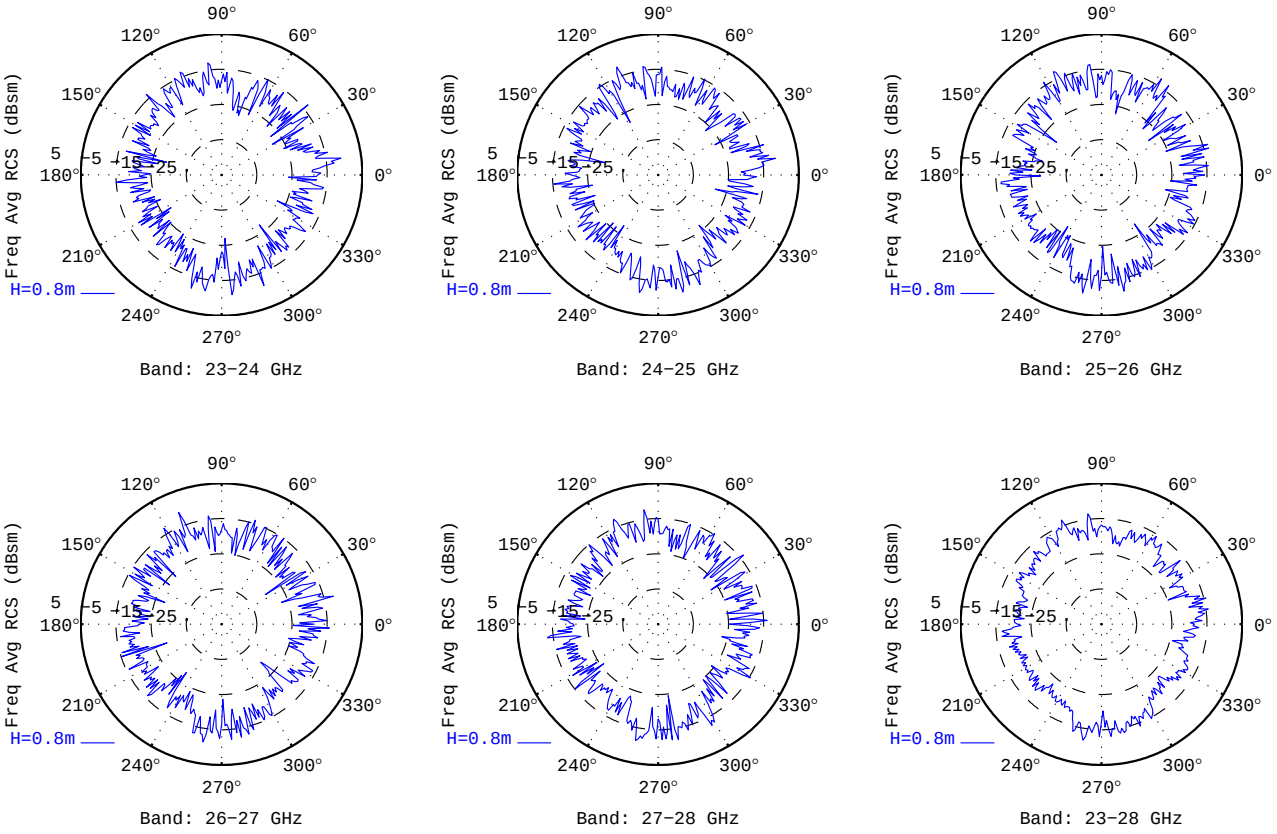

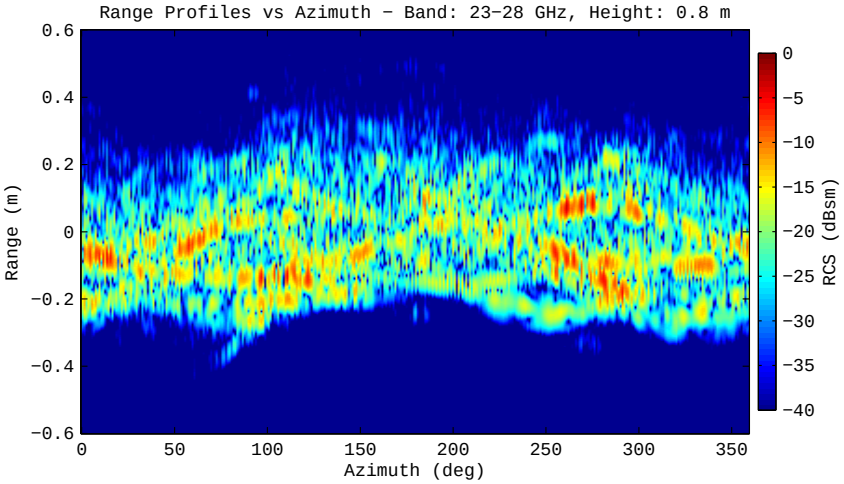

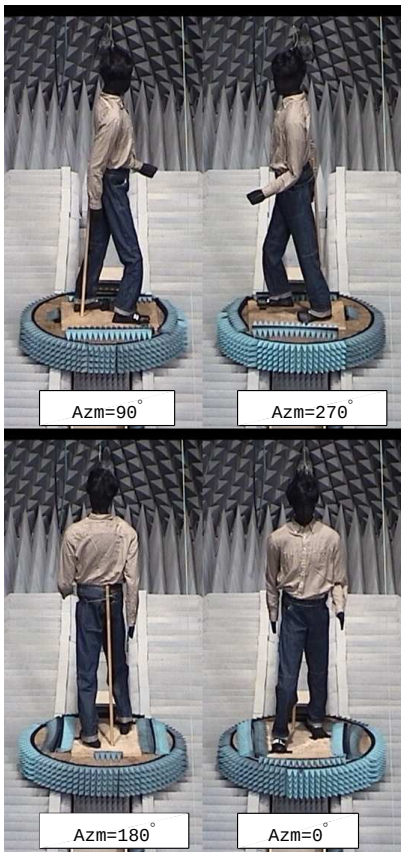

Dummy Type: IDIADA MS Position

Frequency/Azimuth Average RCS (dBsm)

Band (GHz)	23–24	24–25	25–26	26–27	27–28	23–28
Height=0.8m	-8.46	-8.13	-8.22	-8.20	-7.98	-8.19

Figure C.5

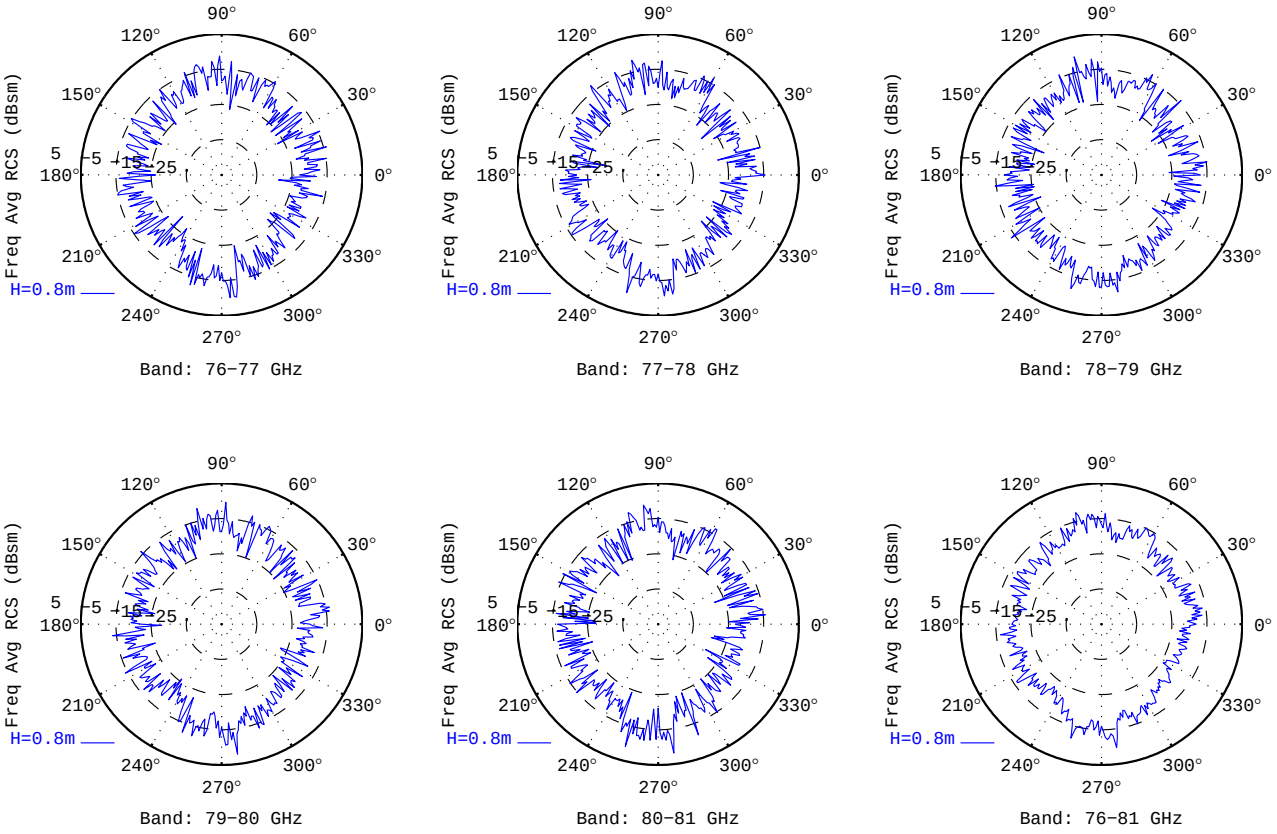

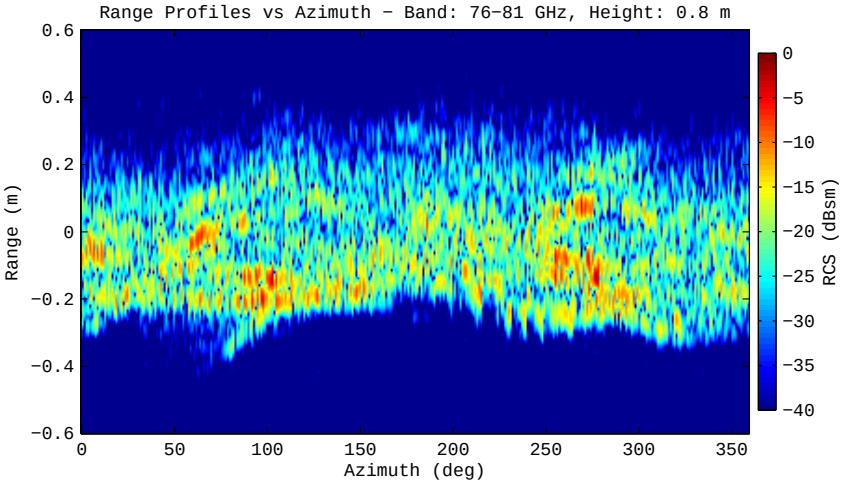

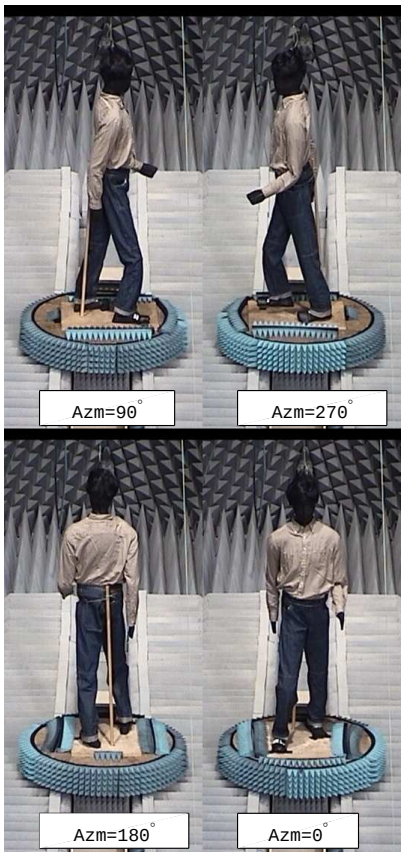

Dummy Type: IDIADA MS Position

Frequency/Azimuth Average RCS (dBsm)

Band (GHz)	76–77	77–78	78–79	79–80	80–81	76–81
Height=0.8m	-8.25	-8.57	-8.40	-7.88	-7.92	-8.20

Figure C.6

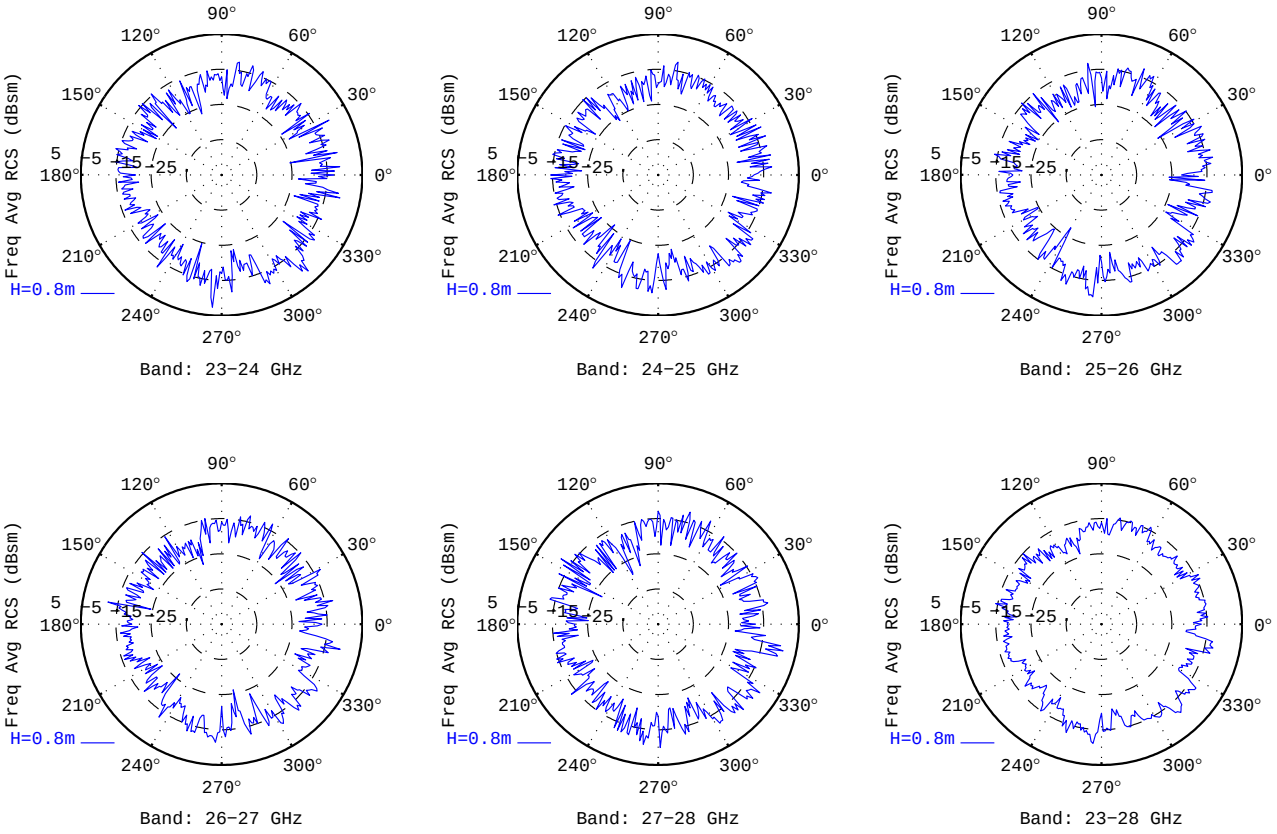

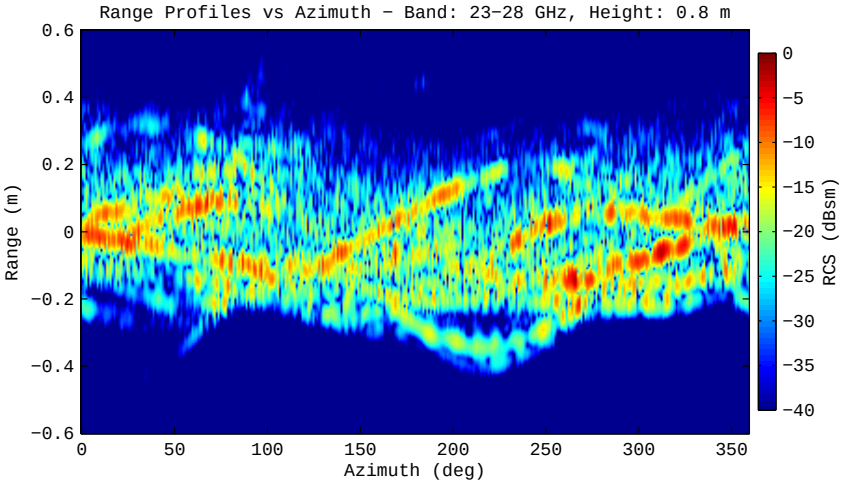

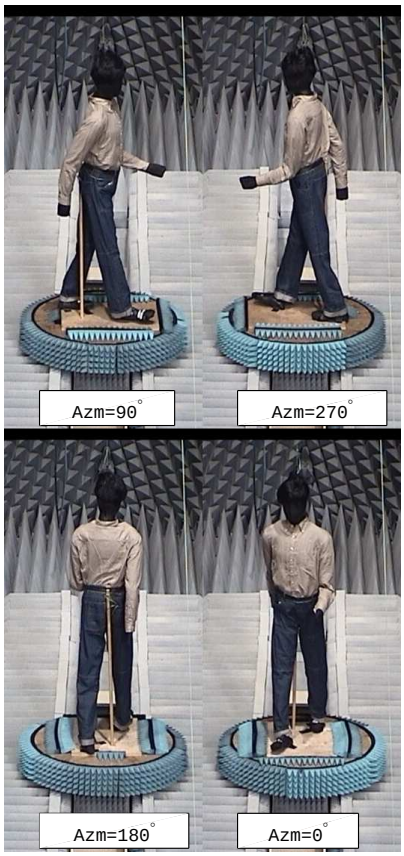

Dummy Type: IDIADA TSw Position

Frequency/Azimuth Average RCS (dBsm)

Band (GHz)	23–24	24–25	25–26	26–27	27–28	23–28
Height=0.8m	-6.42	-6.76	-6.94	-6.98	-6.30	-6.69

Figure C.7

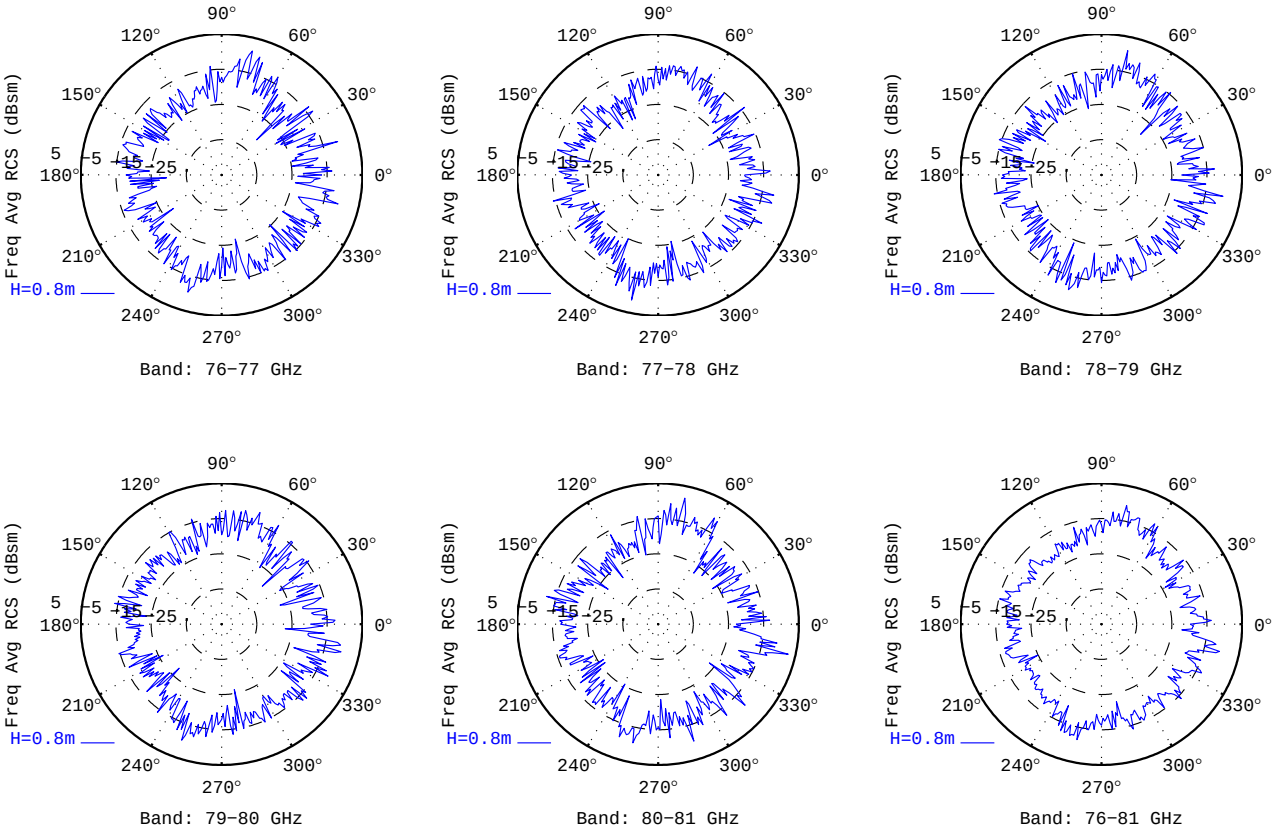

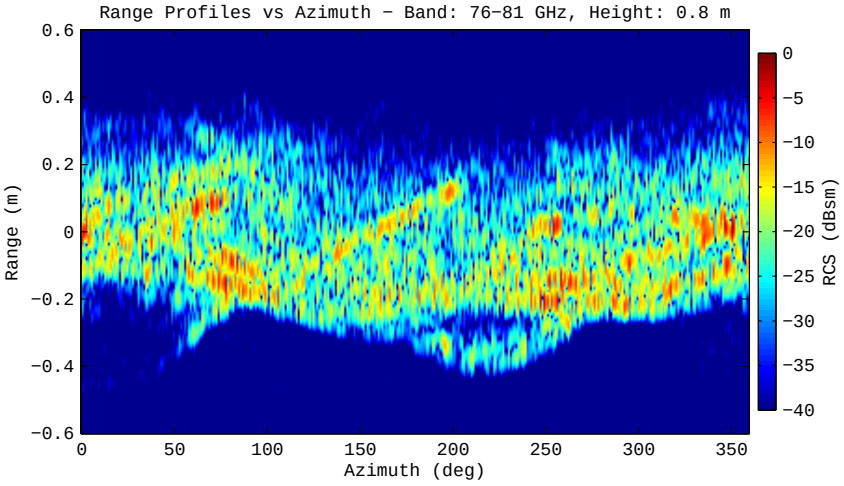

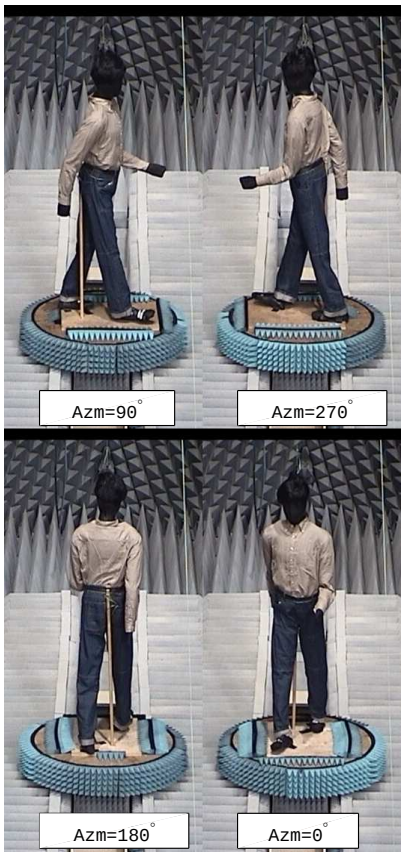

Dummy Type: IDIADA TSw Position

Frequency/Azimuth Average RCS (dBsm)

Band (GHz)	76–77	77–78	78–79	79–80	80–81	76–81
Height=0.8m	-7.62	-7.86	-7.48	-7.14	-7.01	-7.42

Figure C.8

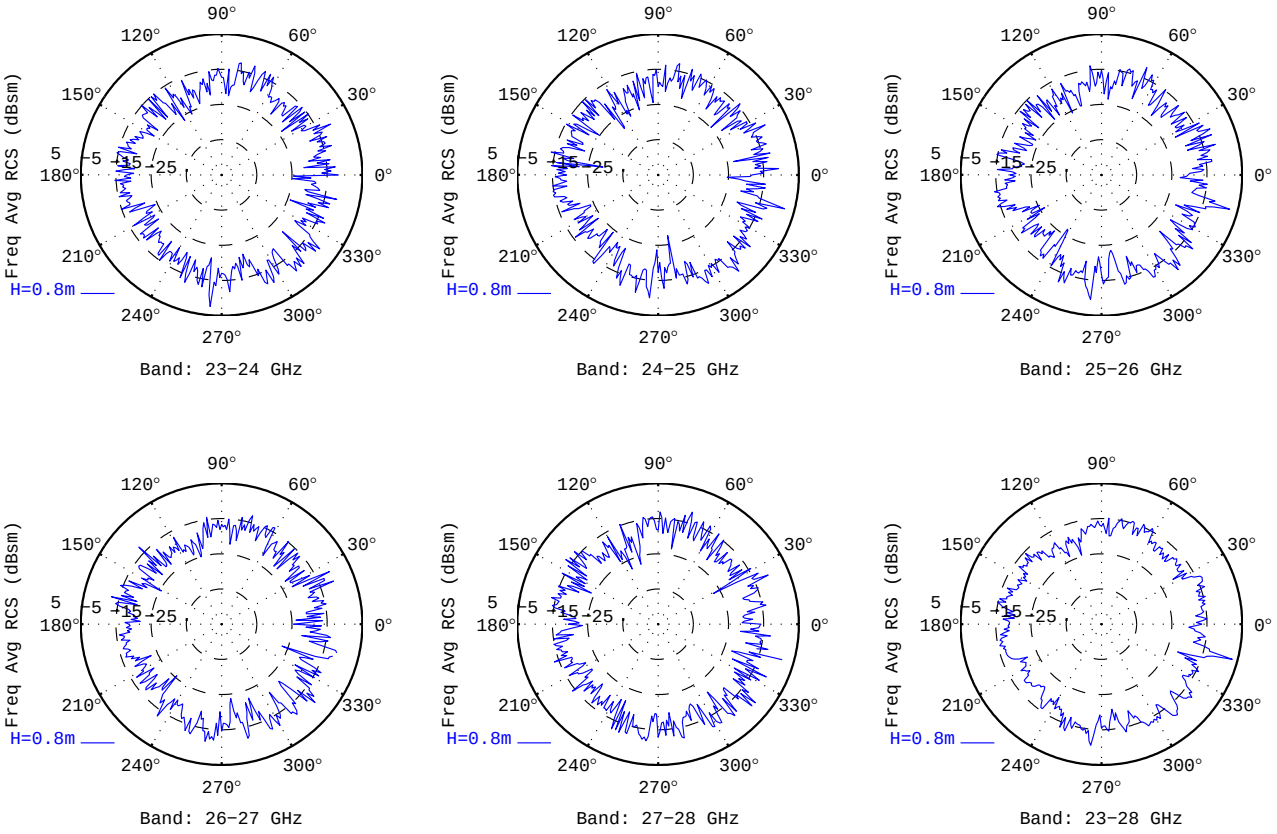

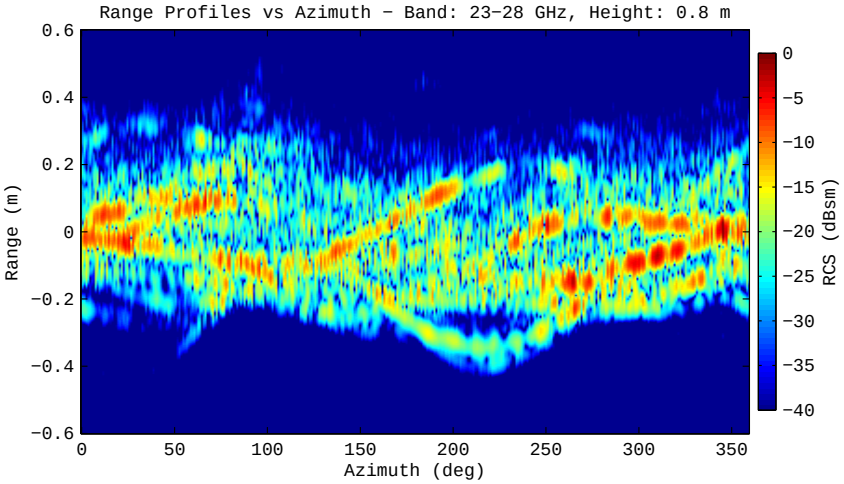

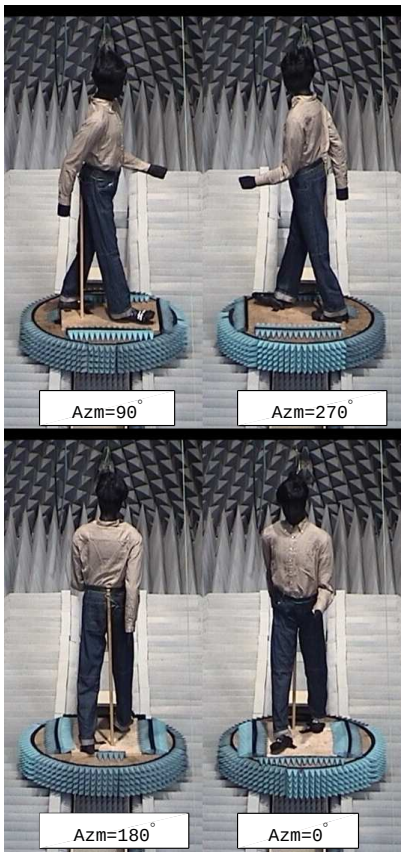

Dummy Type: IDIADA TSw Position

Frequency/Azimuth Average RCS (dBsm)

Band (GHz)	23–24	24–25	25–26	26–27	27–28	23–28
Height=0.8m	-6.41	-6.39	-6.68	-6.56	-6.09	-6.43

Figure C.9

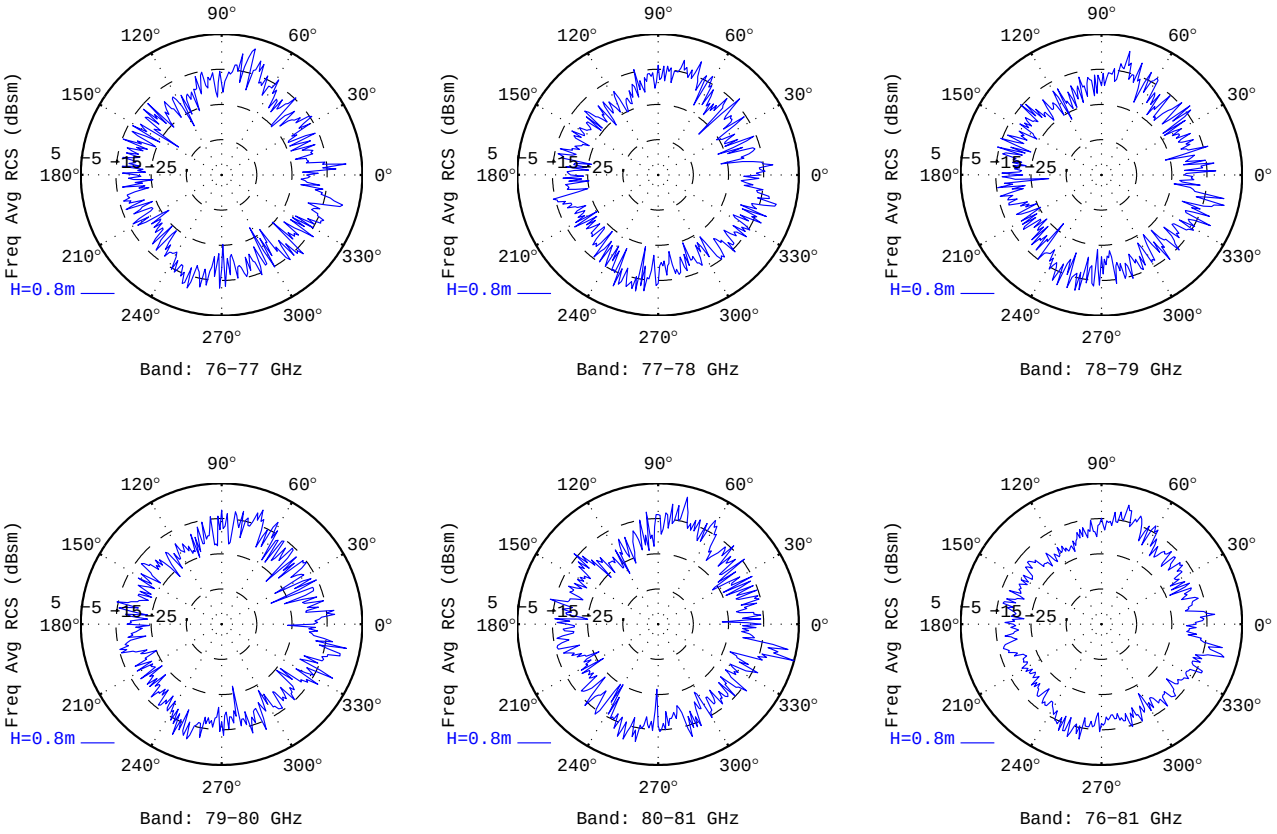

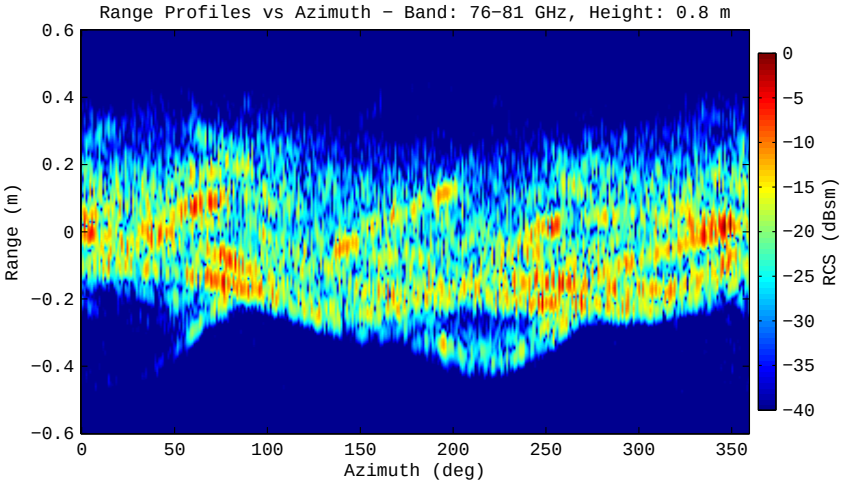

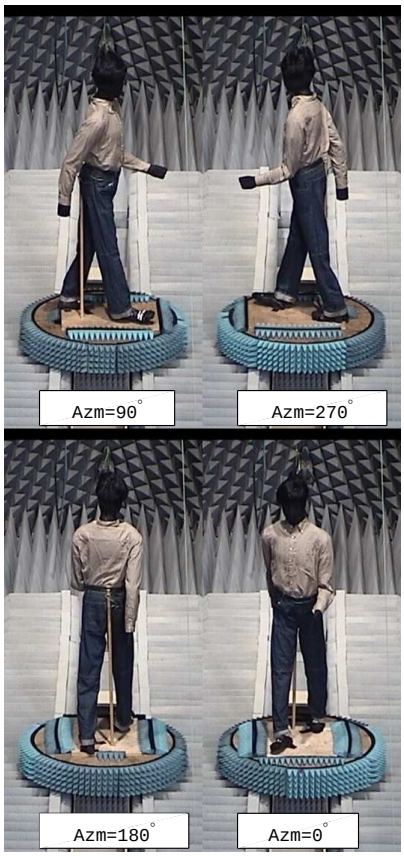

Dummy Type: IDIADA TSw Position

Frequency/Azimuth Average RCS (dBsm)

Band (GHz)	76–77	77–78	78–79	79–80	80–81	76–81
Height=0.8m	-7.30	-7.48	-7.44	-7.19	-6.82	-7.25

Figure C.10

D RCS Signatures of Pedestrians: Measurement Group III

The captions of the figures included in this annex is provided here due to formatting constraints. The complete list of captions is shown in Table D.1.

Table D.1: List of captions for the figures with the RCS signatures of measurement group III.

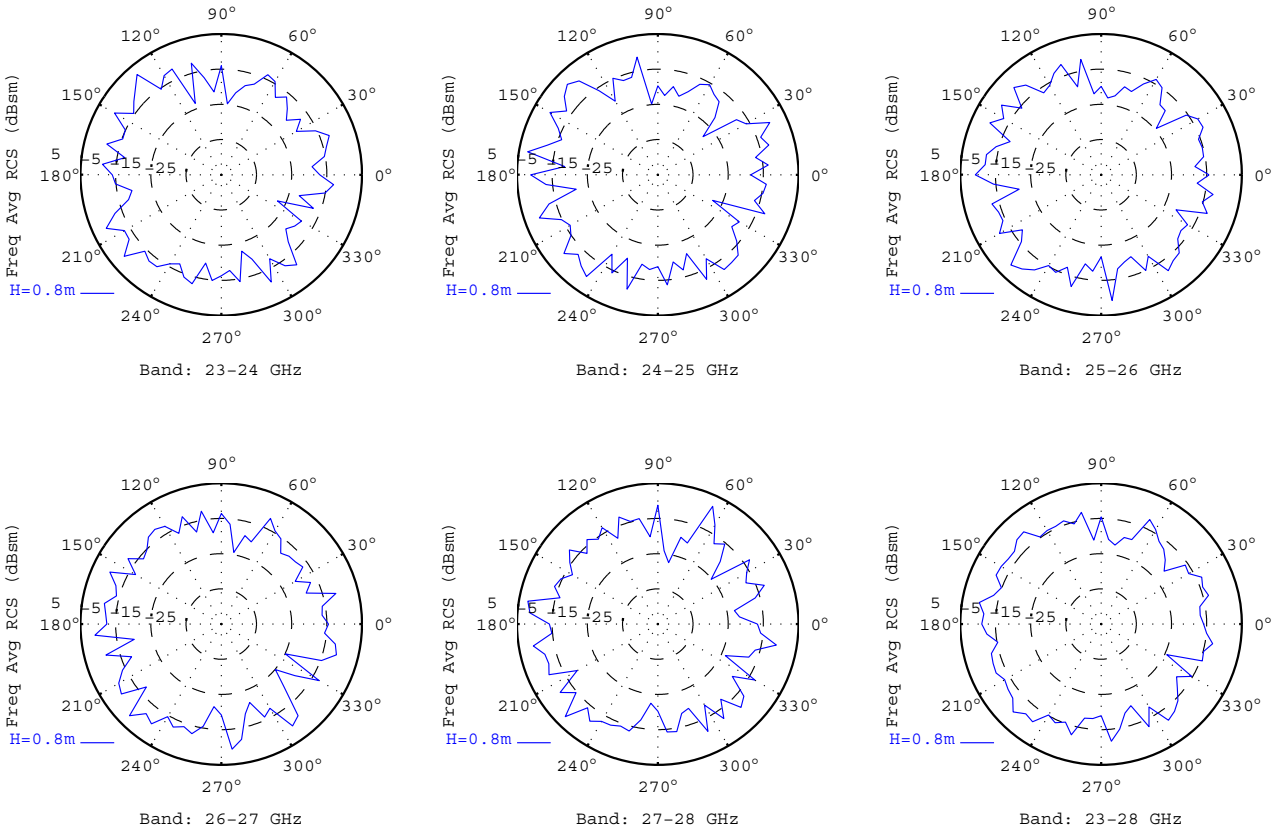

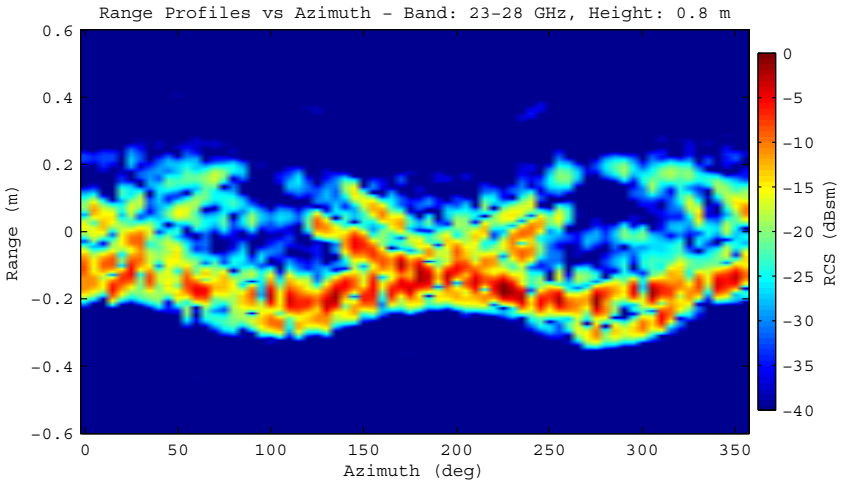

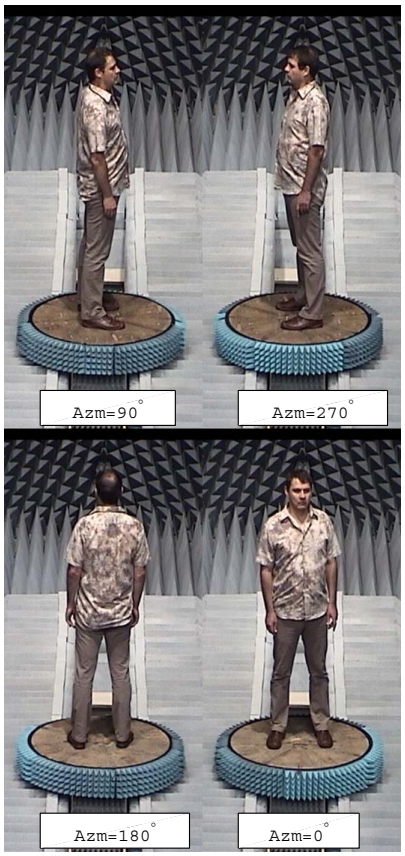

Adult#1 Shirt

Frequency/Azimuth Average RCS (dBsm)

Band (GHz)	23-24	24-25	25-26	26-27	27-28	23-28
Height=0.8m	-4.37	-3.89	-4.15	-3.75	-3.78	-3.98

Figure D.1

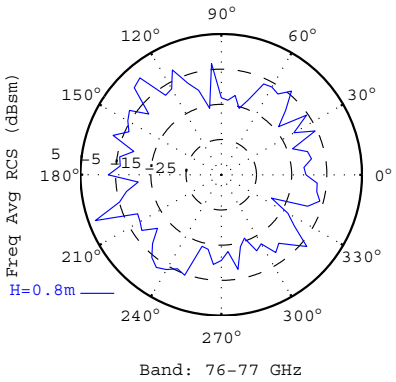

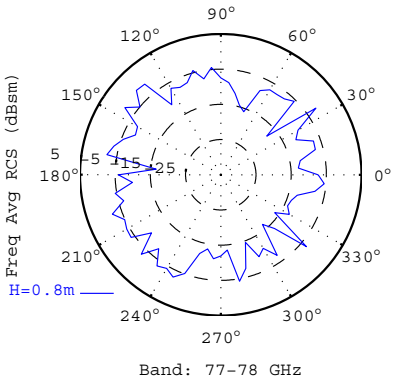

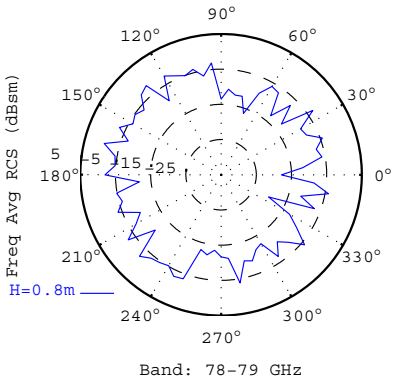

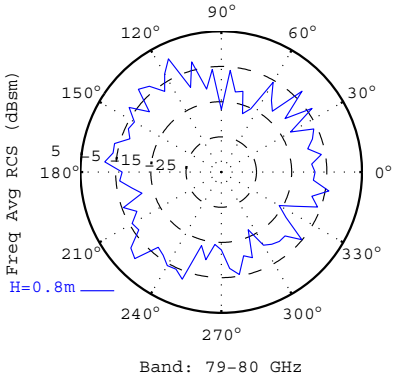

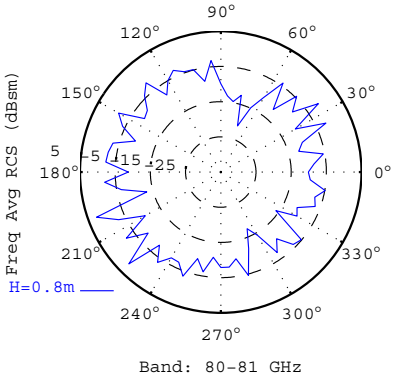

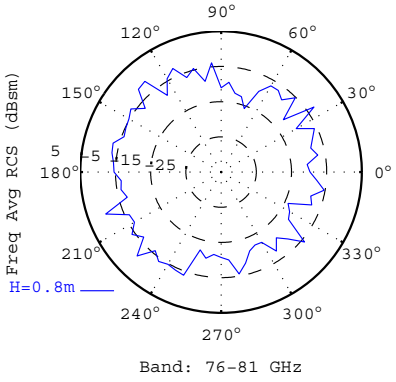

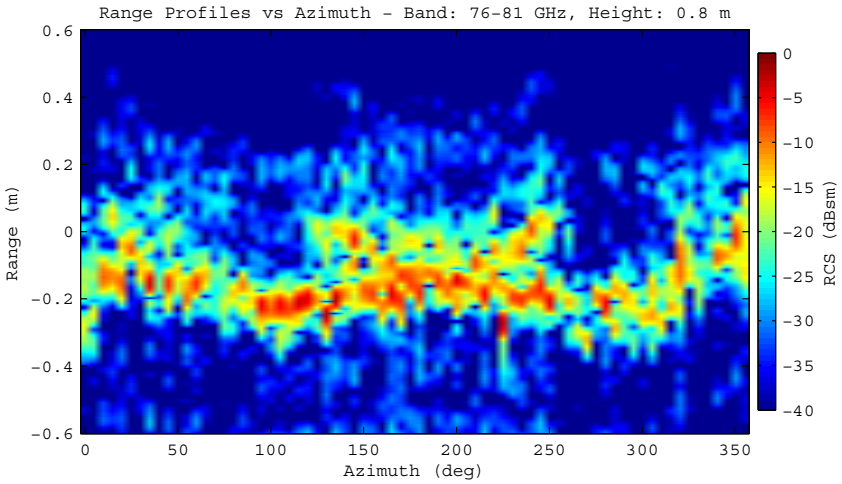

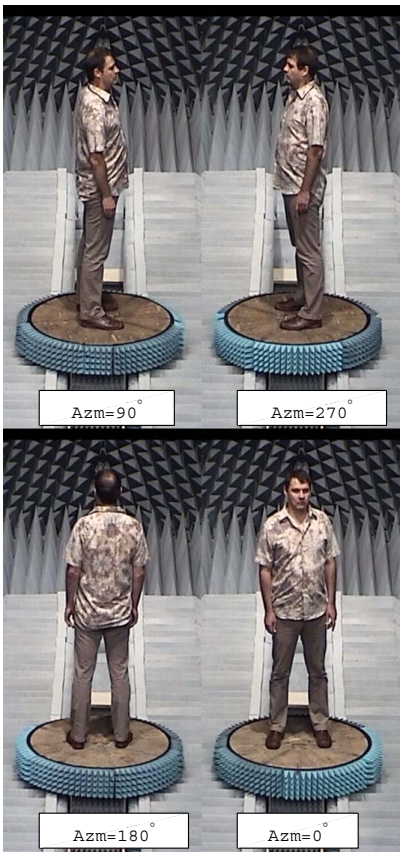

Adult#1 Shirt

Frequency/Azimuth Average RCS (dBsm)

Band (GHz)	76-77	77-78	78-79	79-80	80-81	76-81
Height=0.8m	-6.20	-6.45	-6.11	-6.12	-5.49	-6.07

Figure D.2

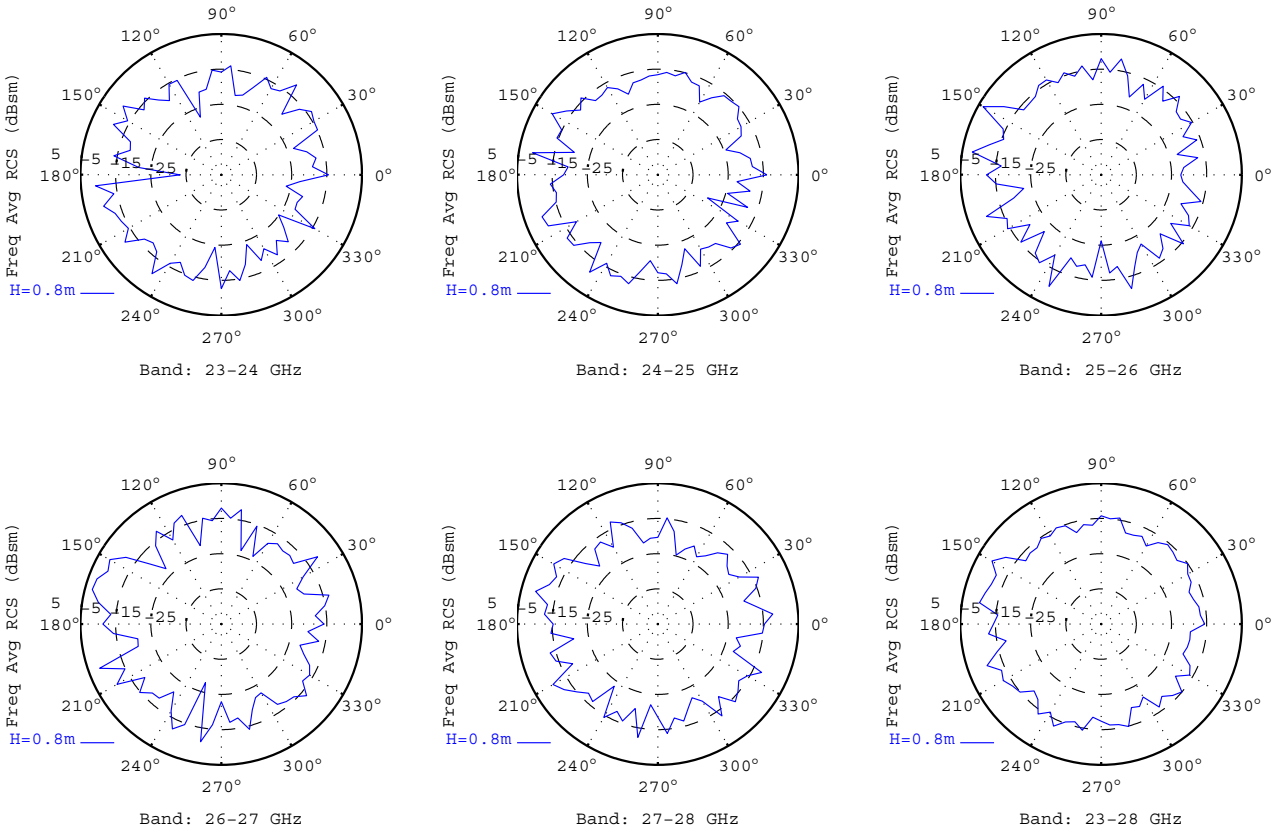

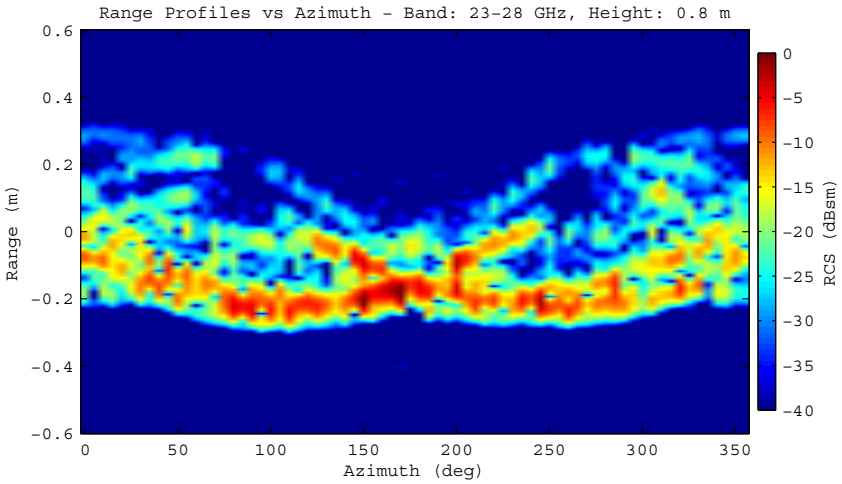

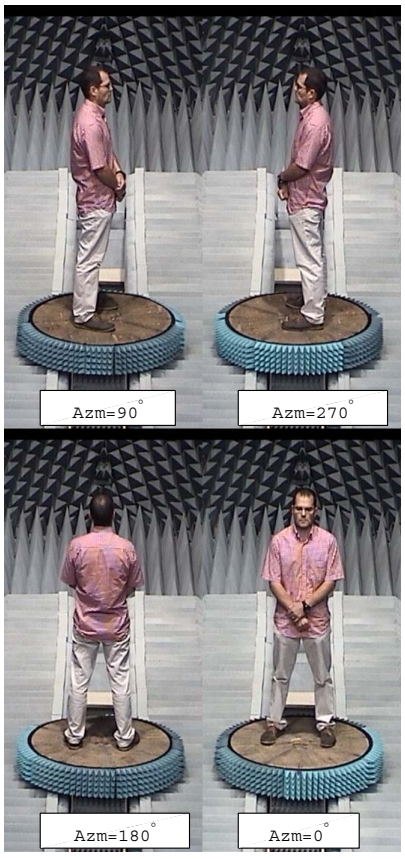

Adult#2 Shirt

Frequency/Azimuth Average RCS (dBsm)

Band (GHz)	23-24	24-25	25-26	26-27	27-28	23-28
Height=0.8m	-5.69	-5.77	-5.03	-4.29	-5.59	-5.22

Figure D.3

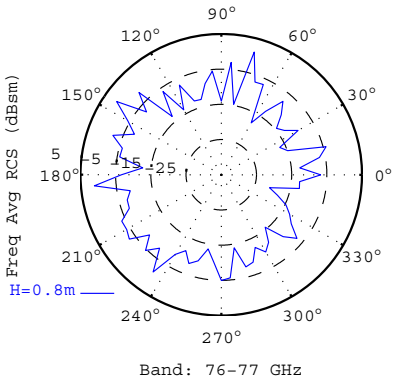

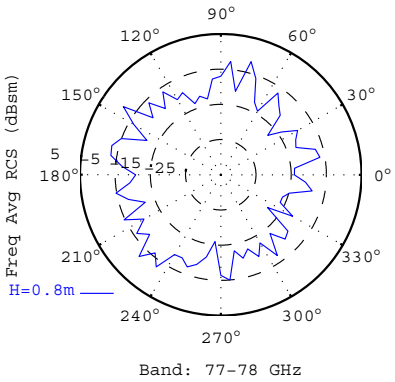

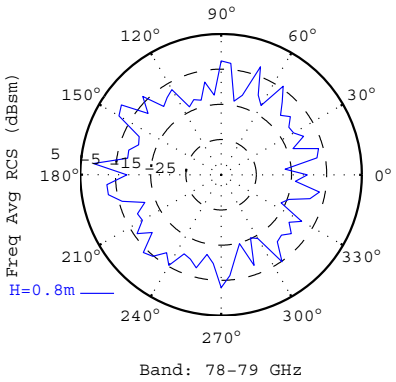

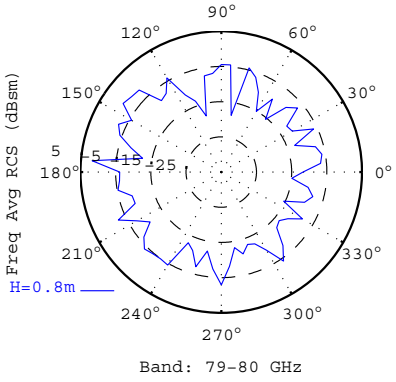

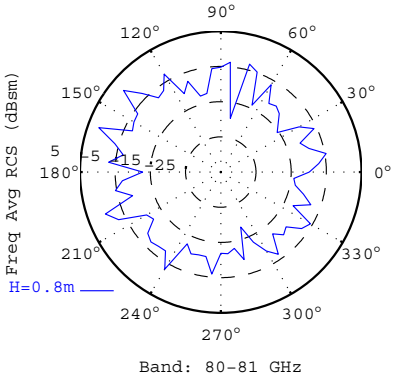

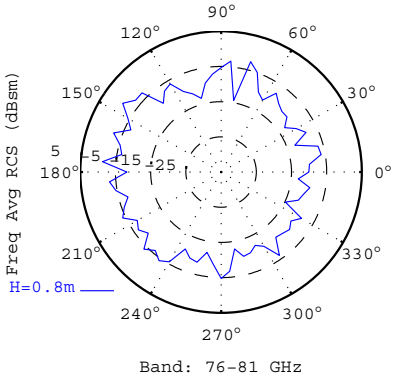

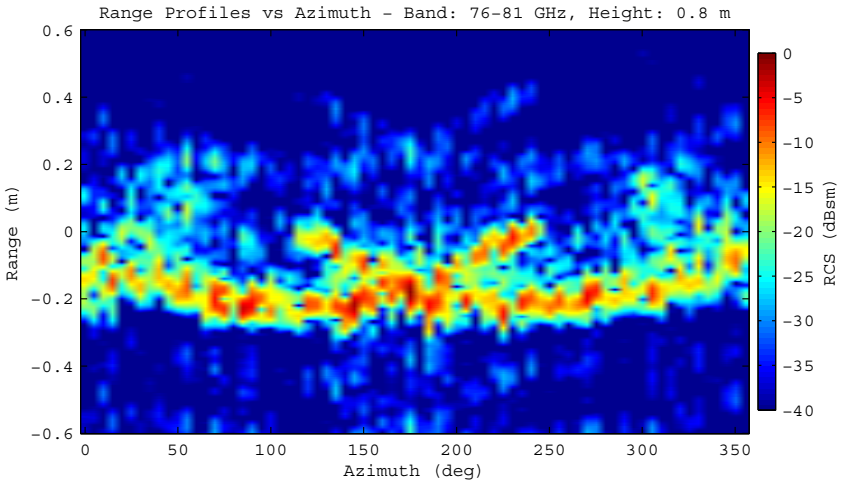

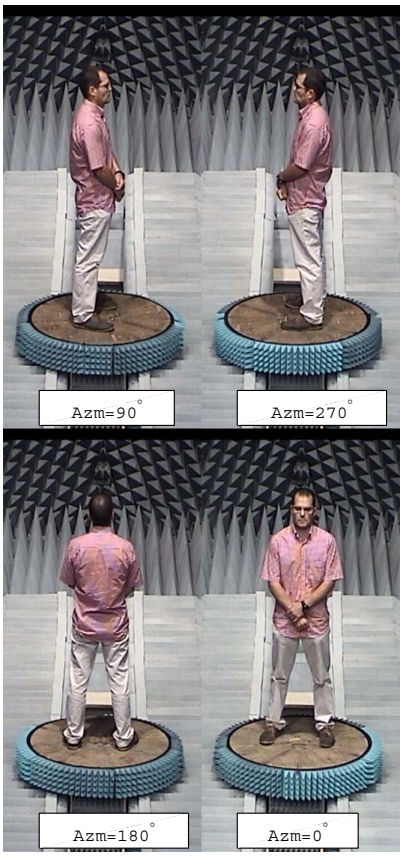

Adult#2 Shirt

Frequency/Azimuth Average RCS (dBsm)

Band (GHz)	76-77	77-78	78-79	79-80	80-81	76-81
Height=0.8m	-6.57	-7.70	-6.87	-6.62	-6.55	-6.86

Figure D.4

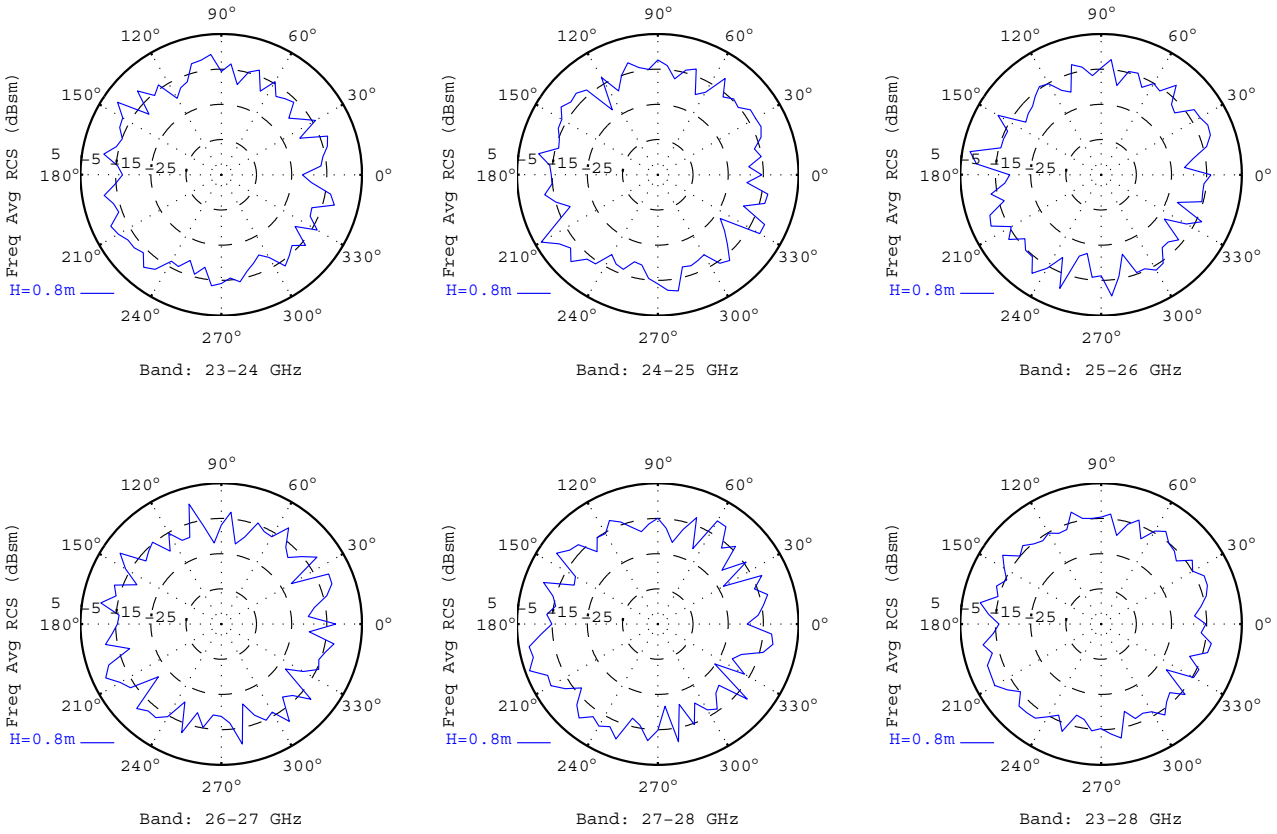

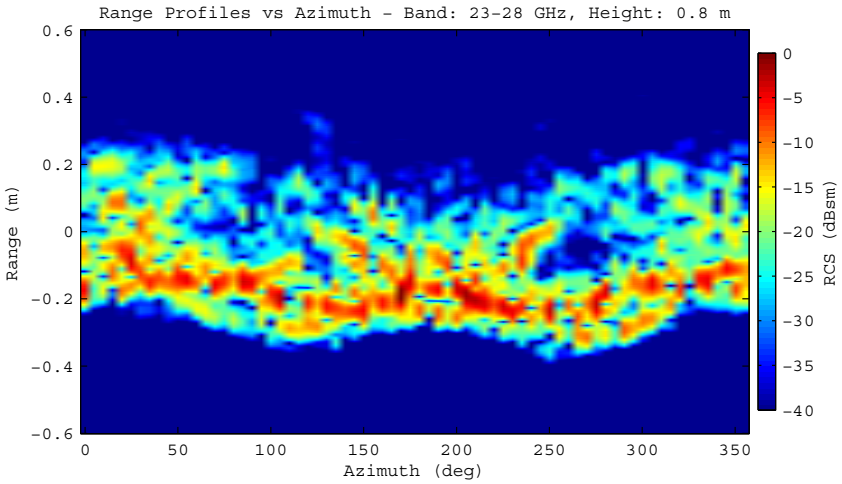

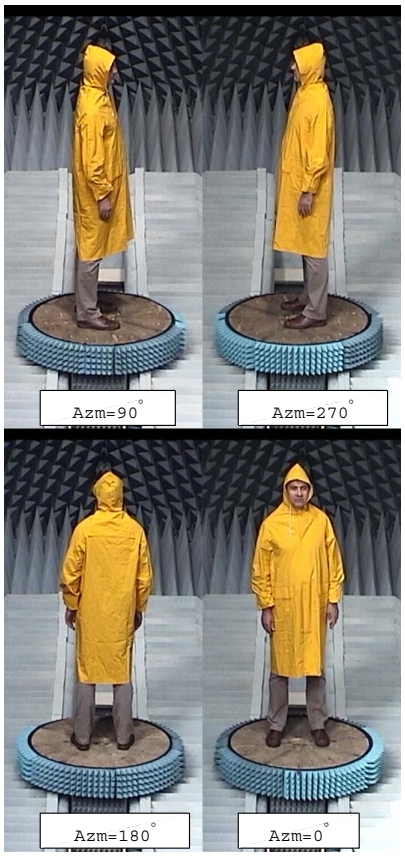

Adult#1 Thick Yellow Rain Coat

Frequency/Azimuth Average RCS (dBsm)

Band (GHz)	23-24	24-25	25-26	26-27	27-28	23-28
Height=0.8m	-4.31	-3.99	-4.37	-4.25	-3.49	-4.08

Figure D.5

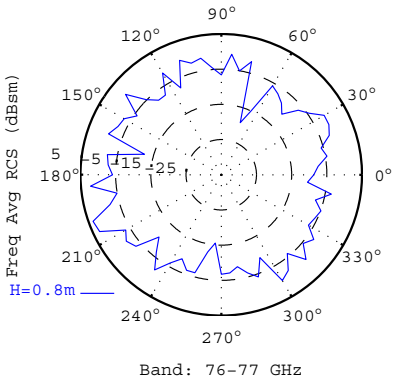

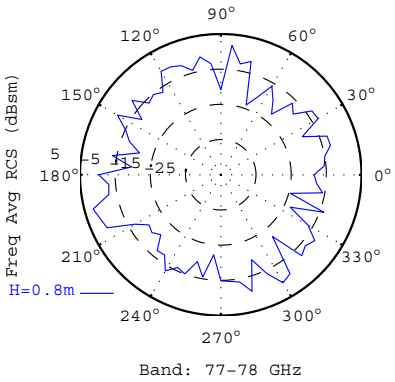

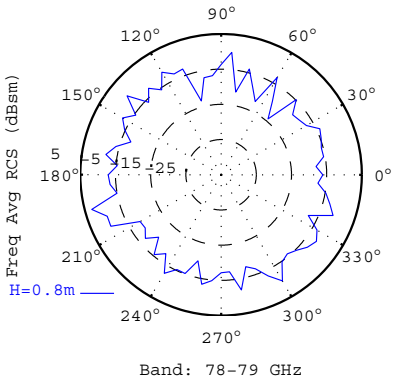

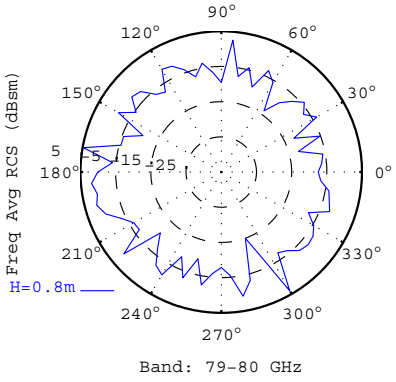

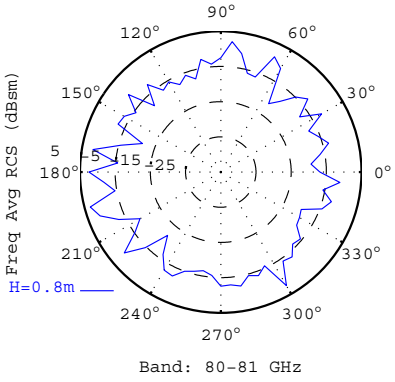

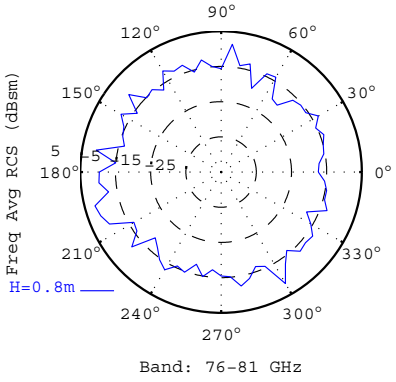

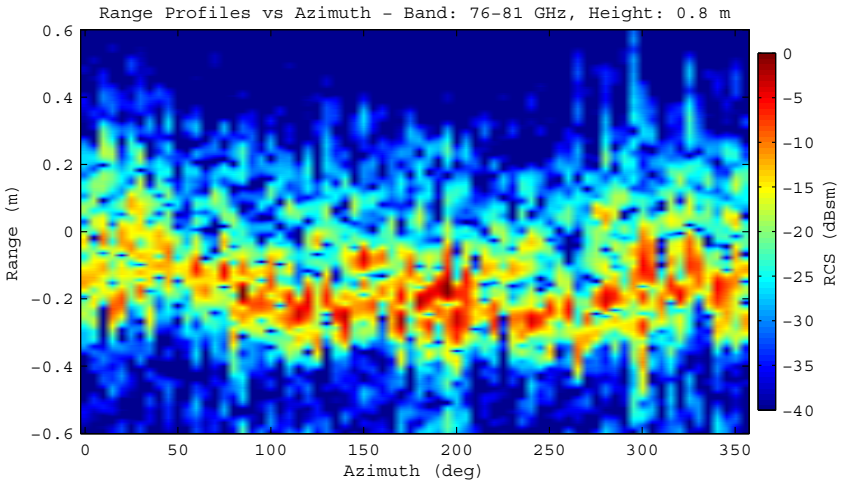

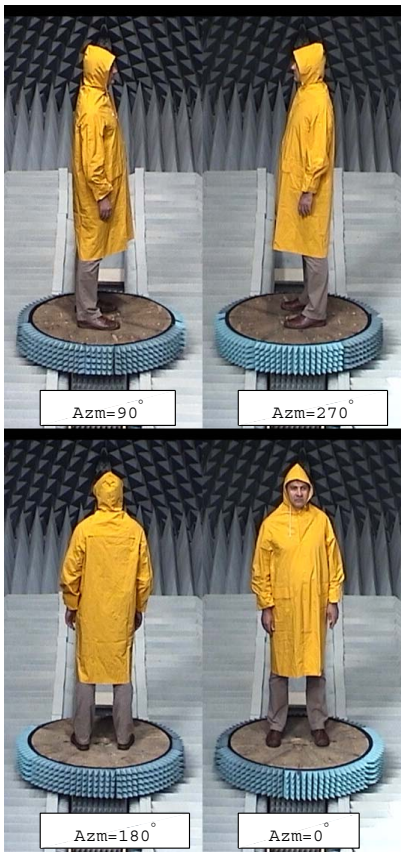

Adult#1 Thick Yellow Rain Coat

Frequency/Azimuth Average RCS (dBsm)

Band (GHz)	76-77	77-78	78-79	79-80	80-81	76-81
Height=0.8m	-3.50	-3.84	-4.16	-3.04	-3.07	-3.51

Figure D.6

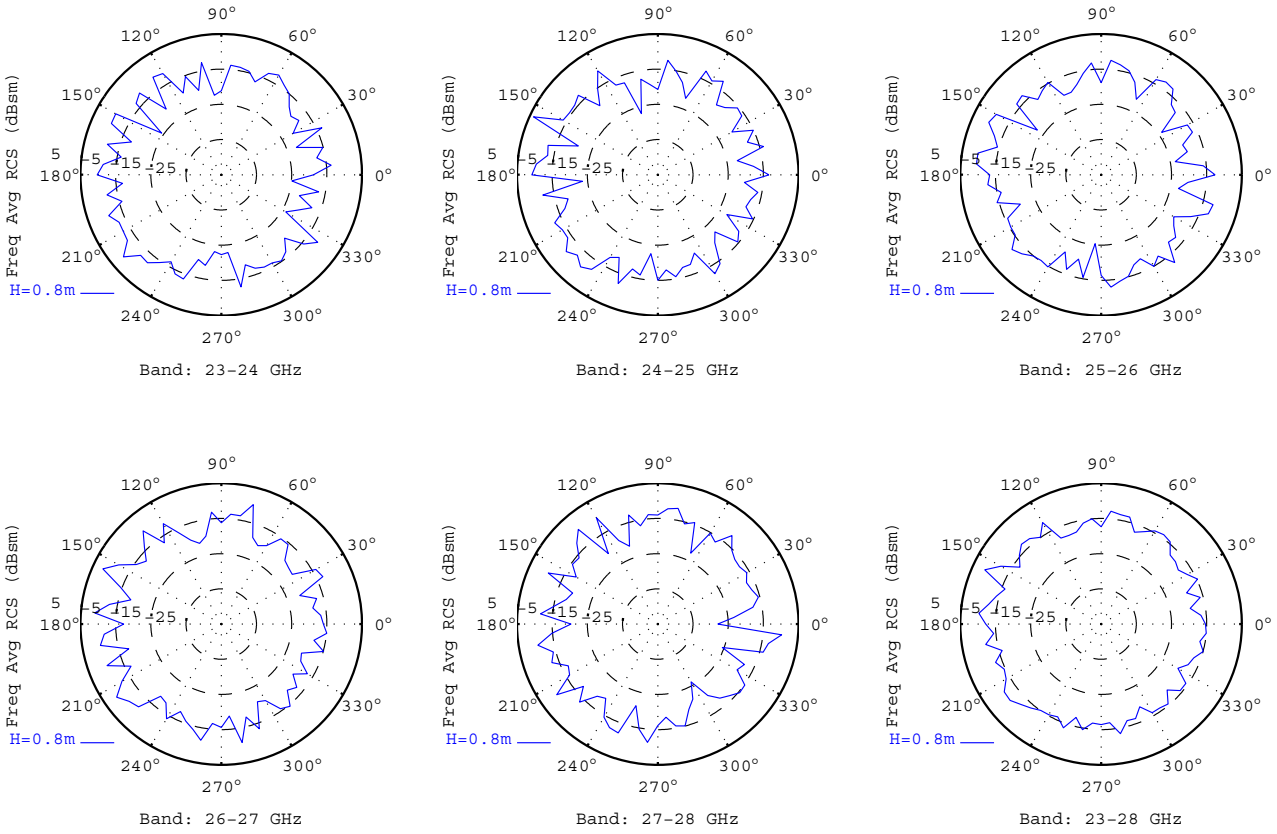

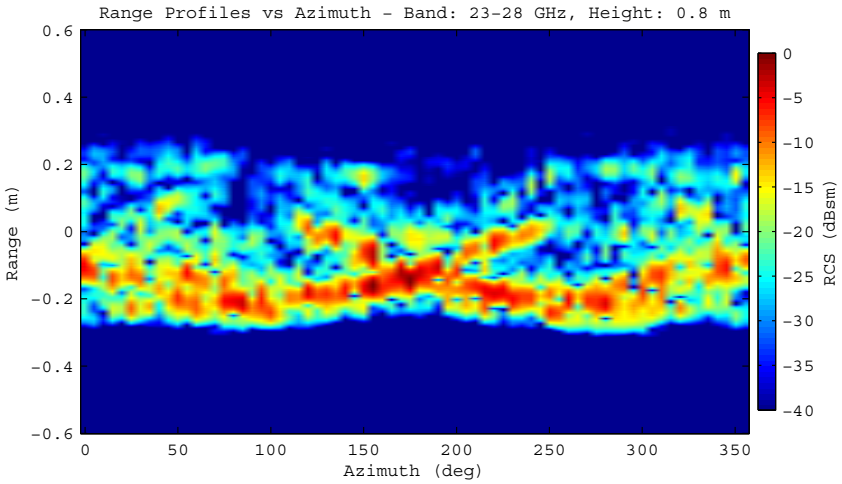

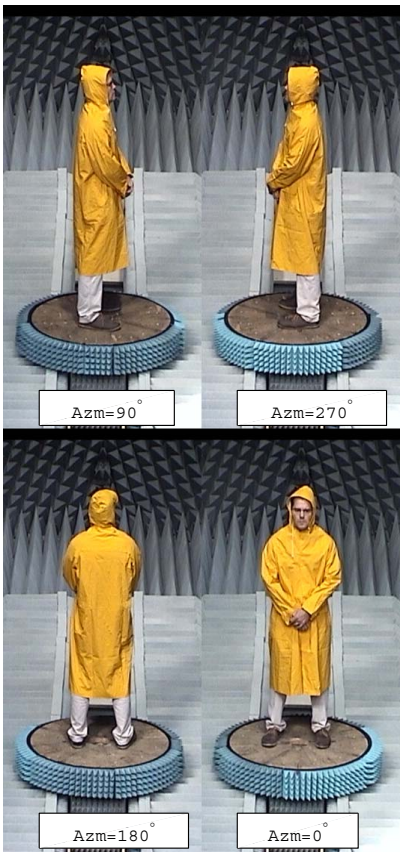

Adult#2 Thick Yellow Rain Coat

Frequency/Azimuth Average RCS (dBsm)

Band (GHz)	23-24	24-25	25-26	26-27	27-28	23-28
Height=0.8m	-4.55	-4.63	-4.90	-4.30	-4.73	-4.62

Figure D.7

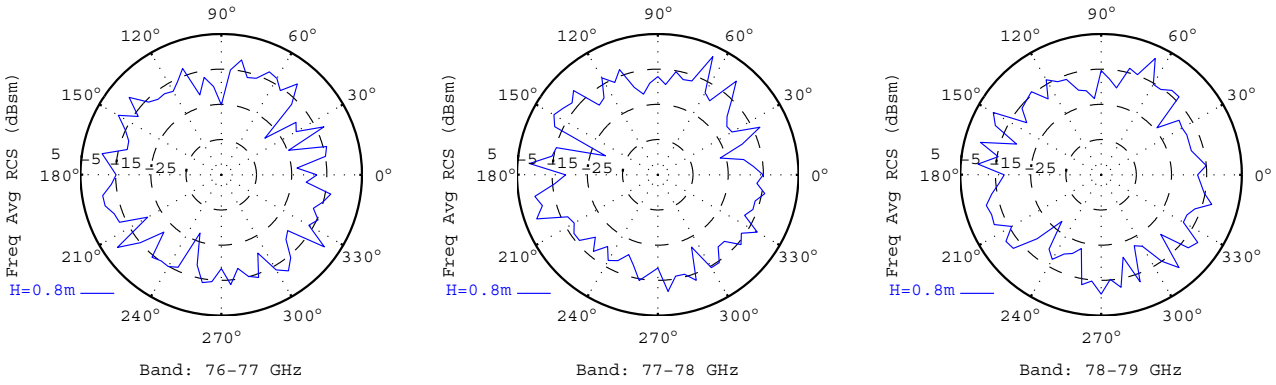

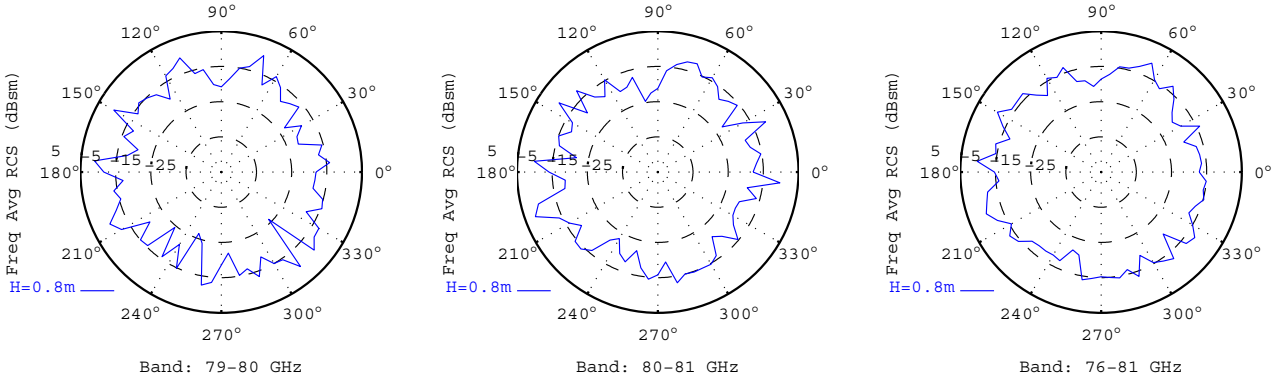

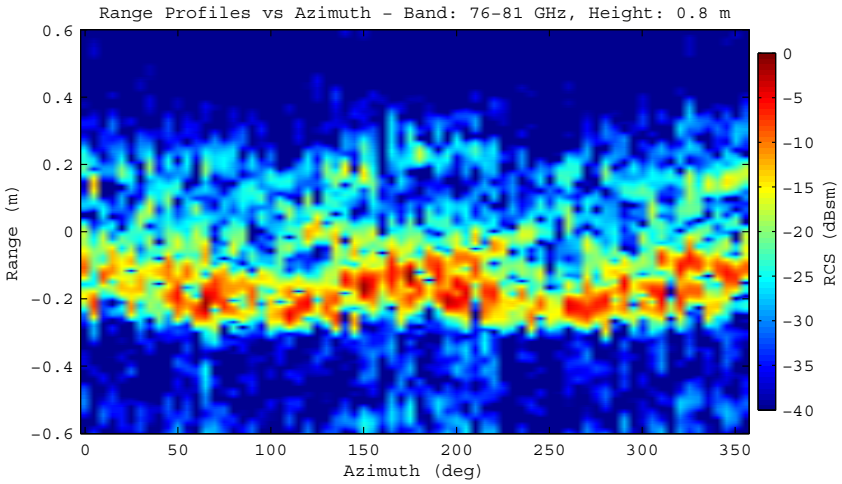

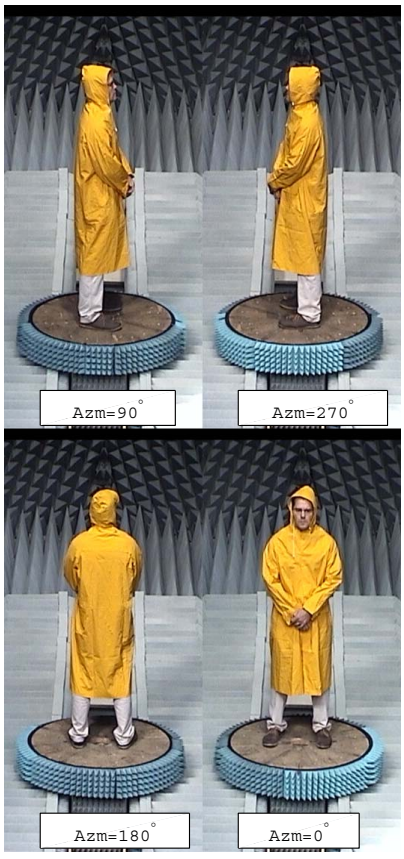

Adult#2 Thick Yellow Rain Coat

Frequency/Azimuth Average RCS (dBsm)

Band (GHz)	76-77	77-78	78-79	79-80	80-81	76-81
Height=0.8m	-4.66	-4.72	-4.64	-4.81	-5.35	-4.82

Figure D.8

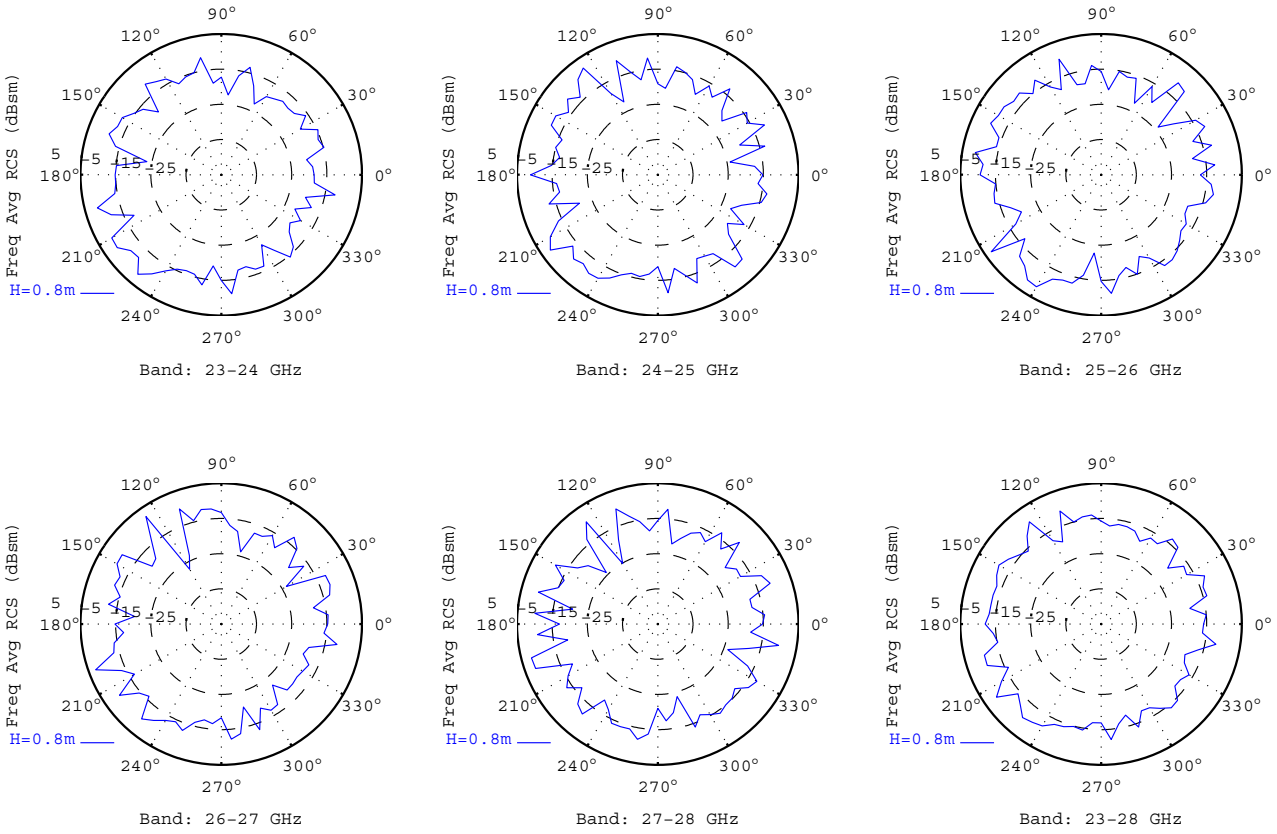

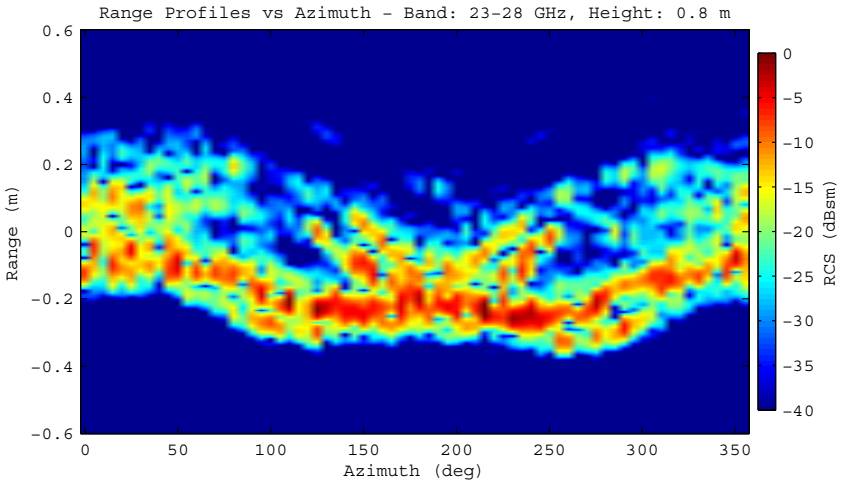

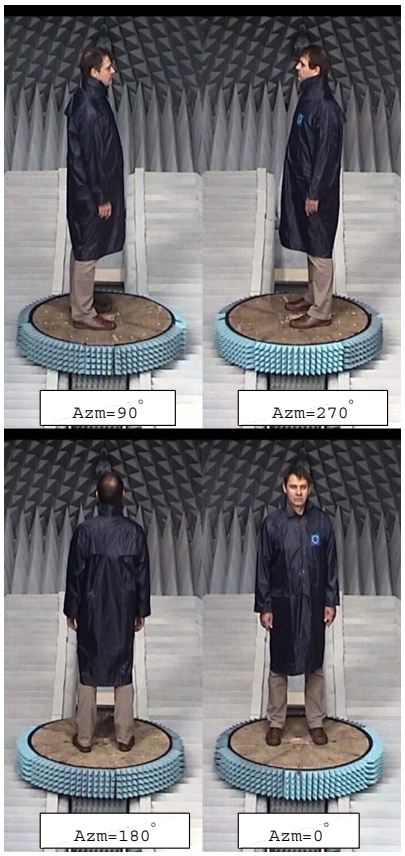

Adult#1 Thin Blue Rain Coat

Frequency/Azimuth Average RCS (dBsm)

Band (GHz)	23-24	24-25	25-26	26-27	27-28	23-28
Height=0.8m	-4.45	-3.82	-3.56	-4.15	-4.20	-4.01

Figure D.9

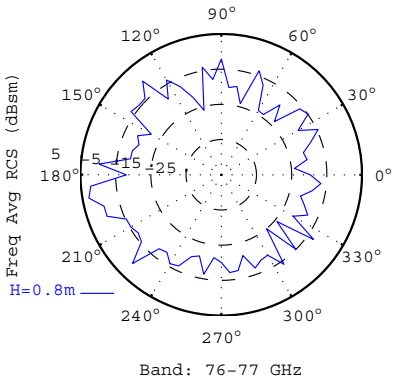

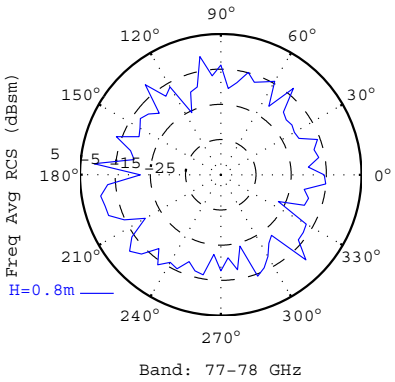

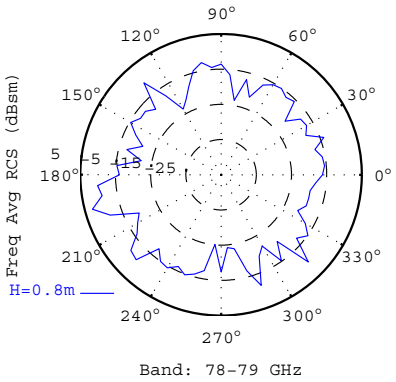

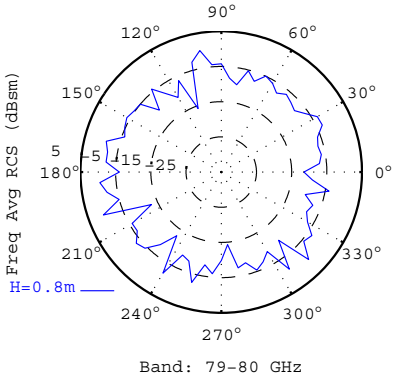

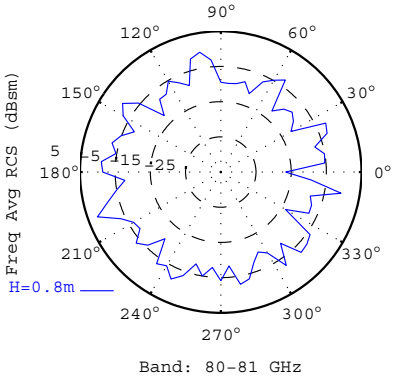

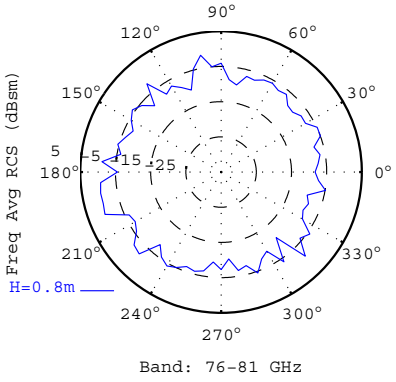

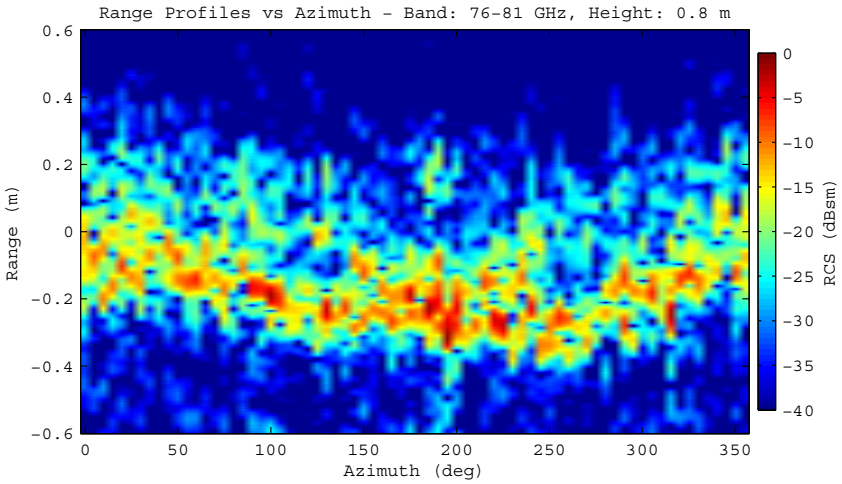

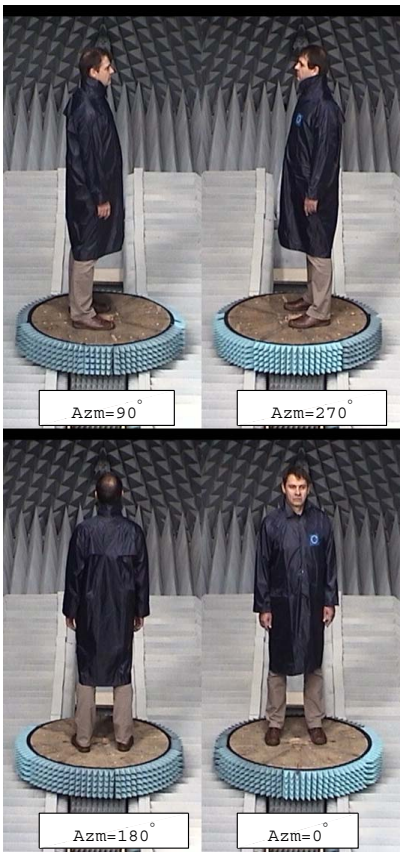

Adult#1 Thin Blue Rain Coat

Frequency/Azimuth Average RCS (dBsm)

Band (GHz)	76-77	77-78	78-79	79-80	80-81	76-81
Height=0.8m	-5.43	-5.71	-5.31	-4.99	-4.71	-5.22

Figure D.10

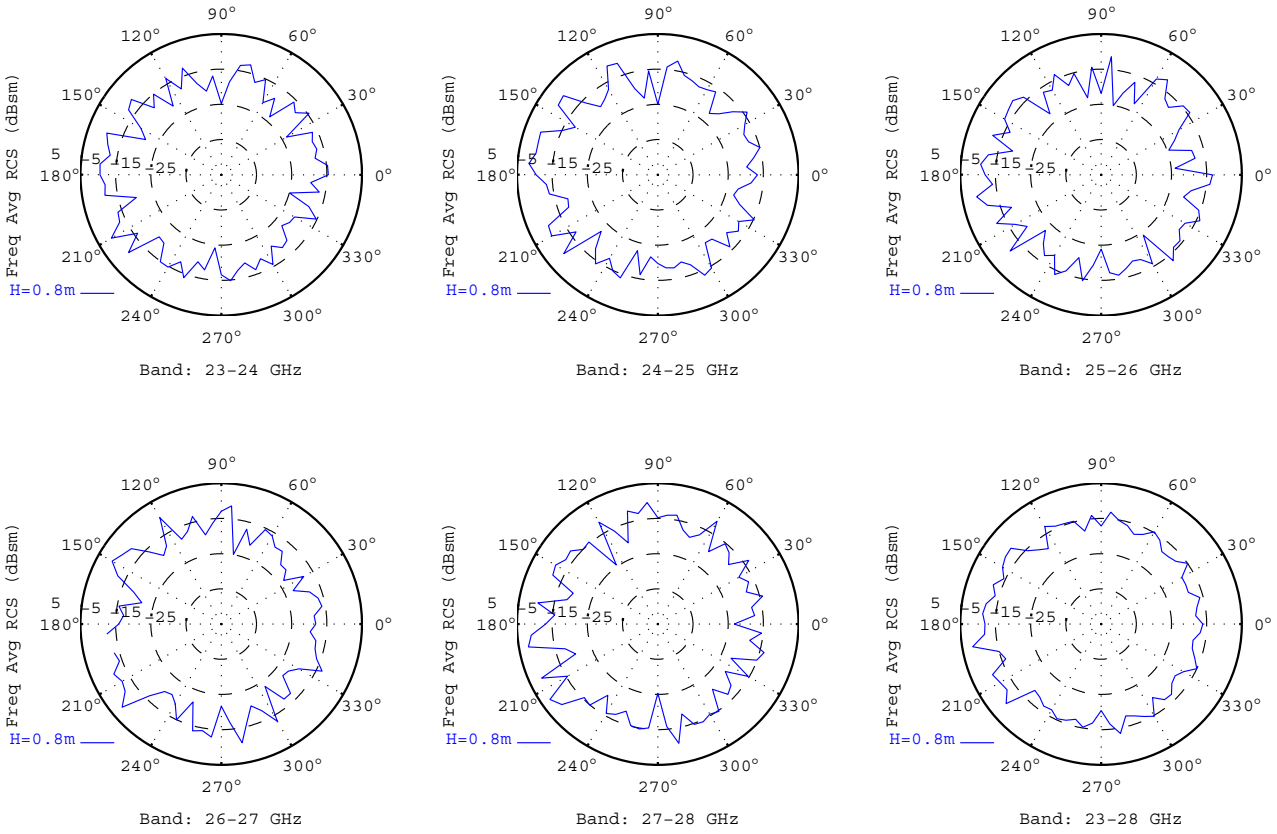

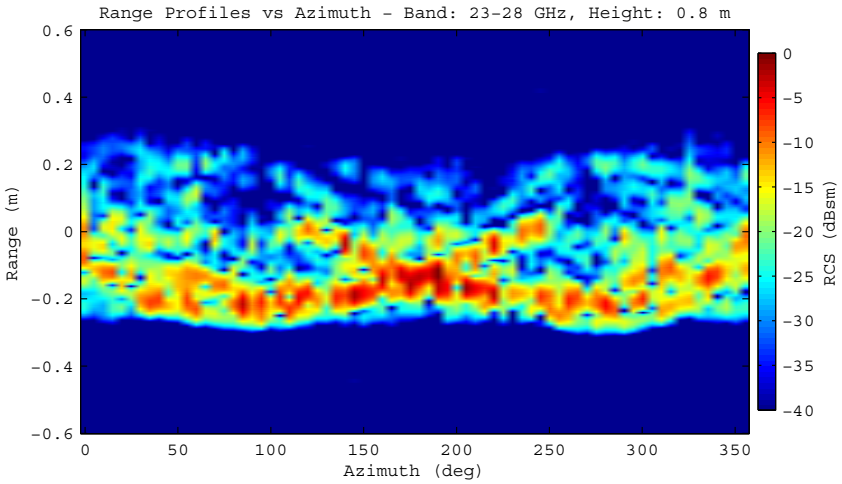

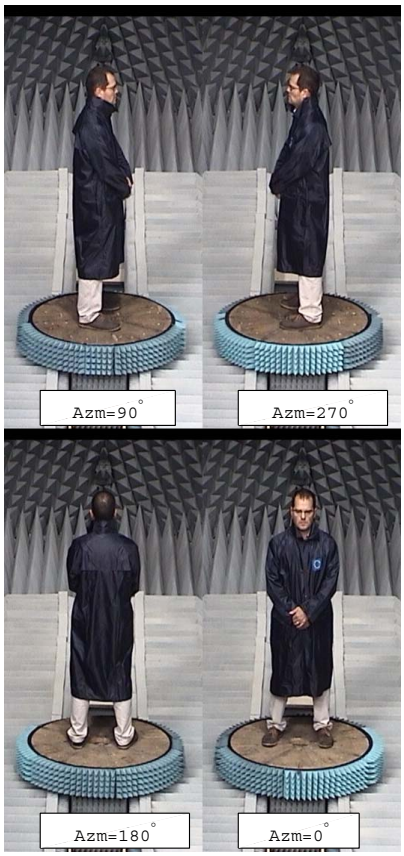

Adult#2 Thin Blue Rain Coat

Frequency/Azimuth Average RCS (dBsm)

Band (GHz)	23-24	24-25	25-26	26-27	27-28	23-28
Height=0.8m	-5.34	-4.78	-5.37	-4.51	-4.13	-4.81

Figure D.11

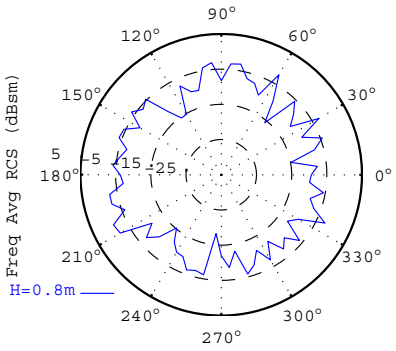

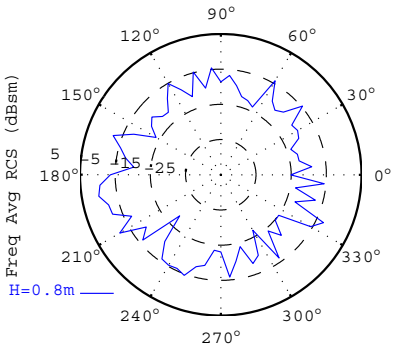

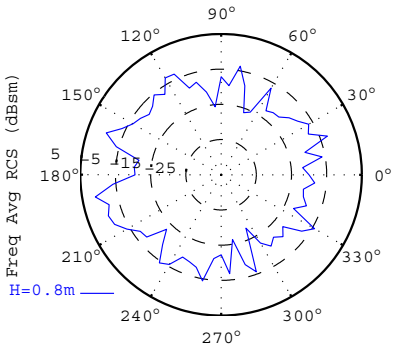

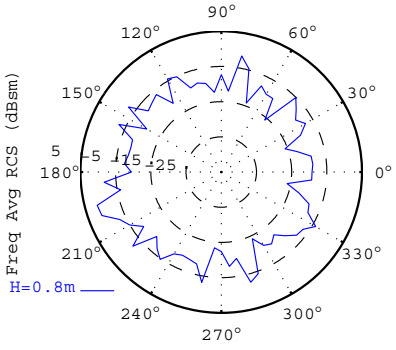

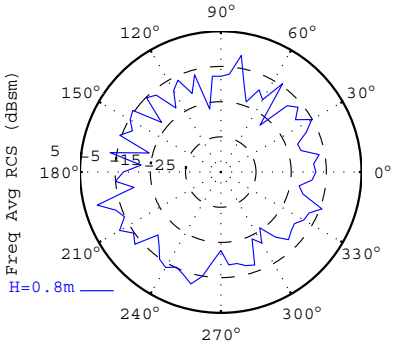

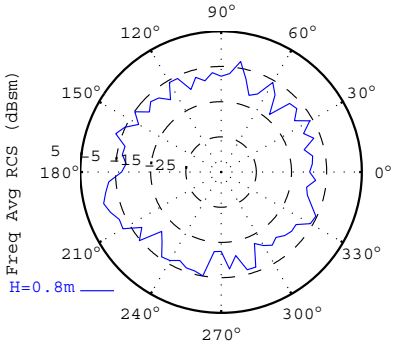

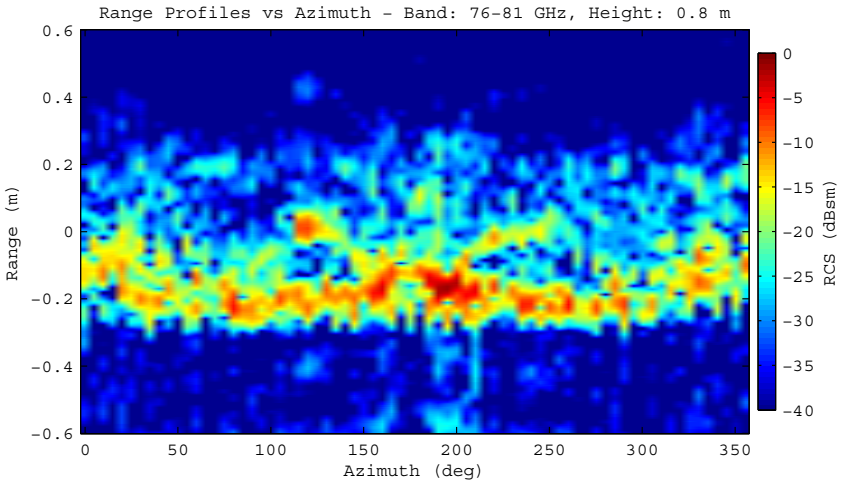

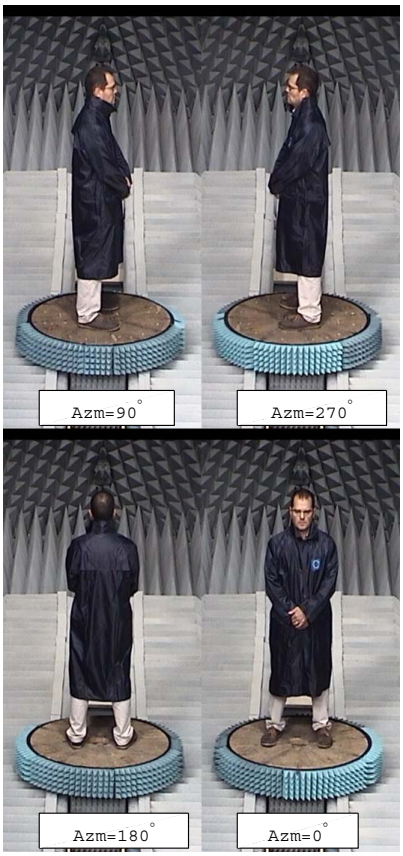

Adult#2 Thin Blue Rain Coat

Frequency/Azimuth Average RCS (dBsm)

Band (GHz)	76-77	77-78	78-79	79-80	80-81	76-81
Height=0.8m	-6.54	-7.01	-6.53	-6.37	-6.51	-6.59

Figure D.12

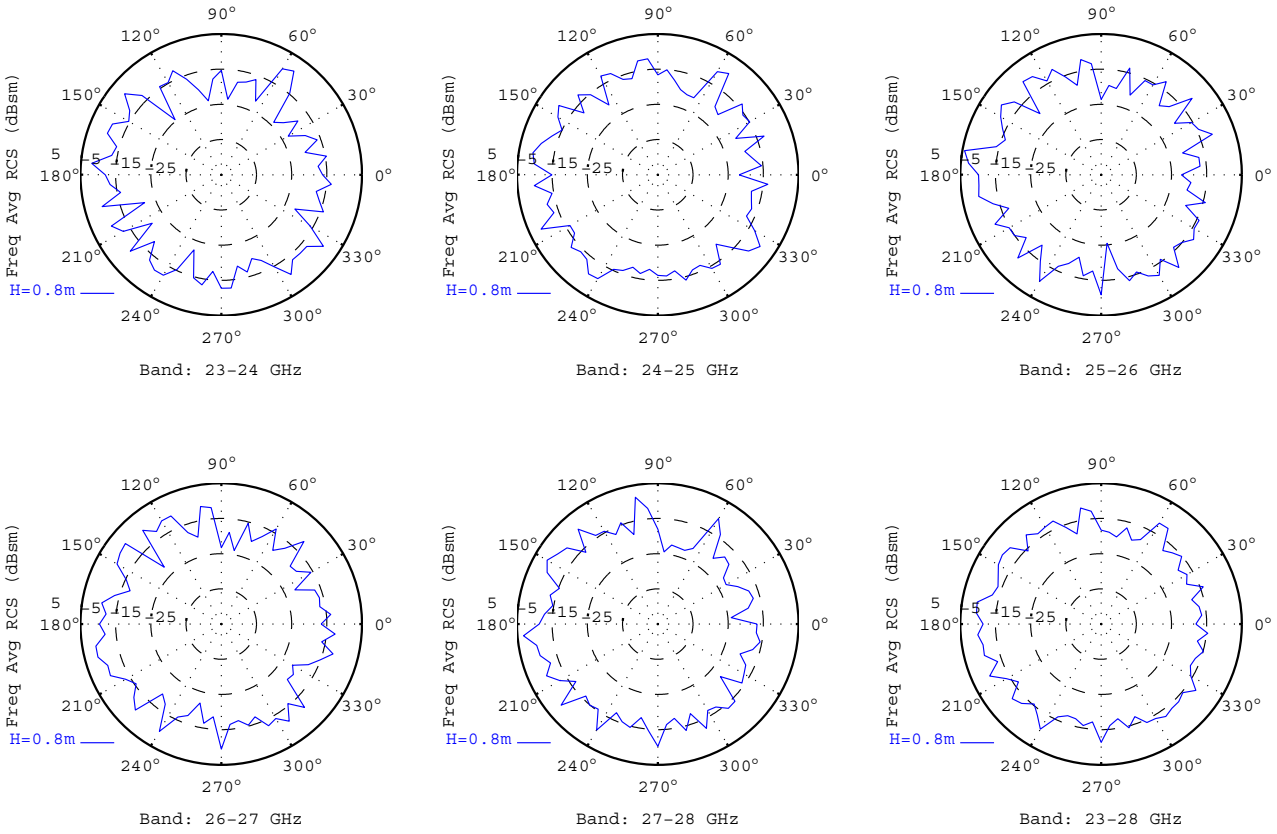

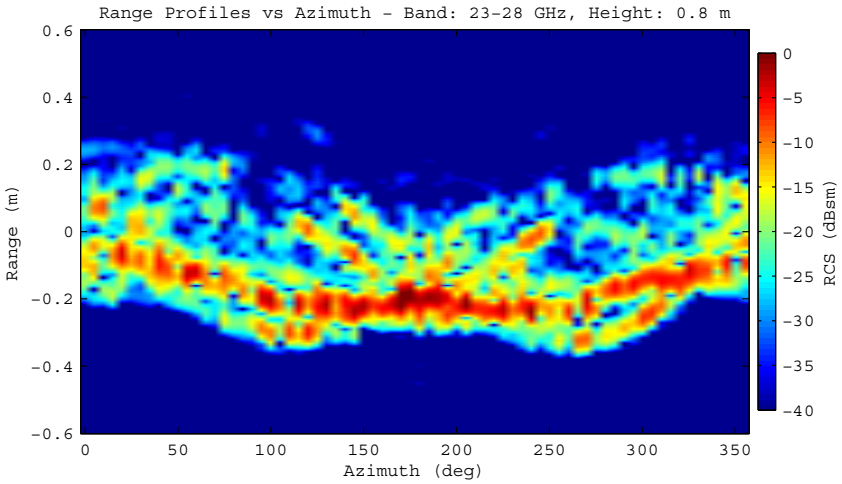

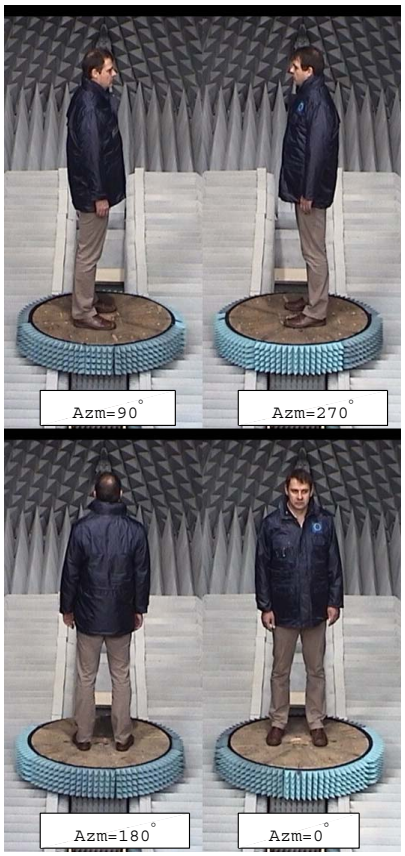

Adult#1 Winter Blue Coat

Frequency/Azimuth Average RCS (dBsm)

Band (GHz)	23-24	24-25	25-26	26-27	27-28	23-28
Height=0.8m	-4.05	-3.89	-3.56	-3.59	-3.78	-3.76

Figure D.13

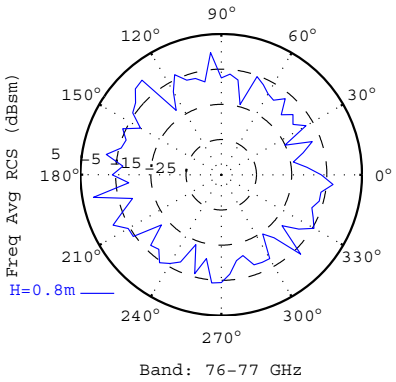

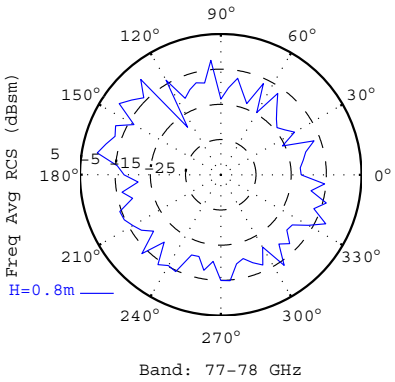

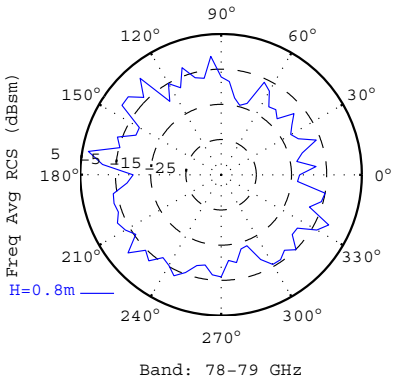

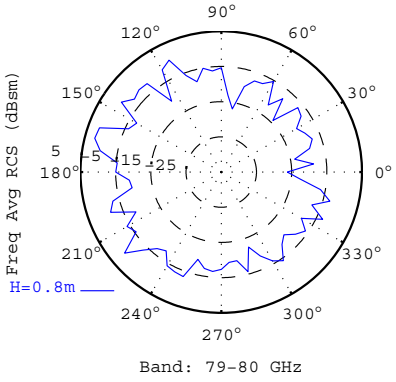

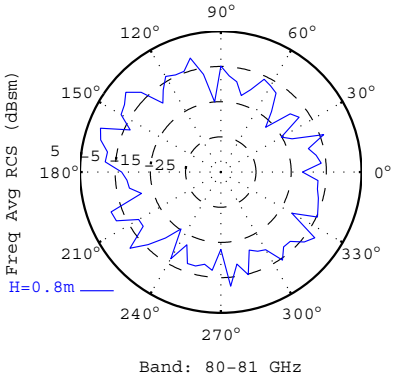

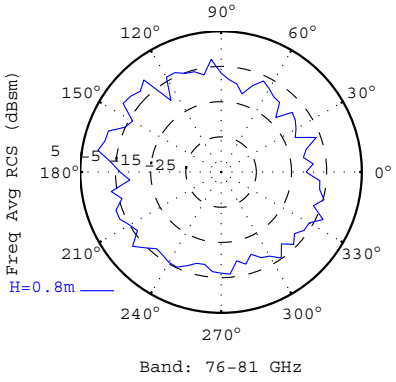

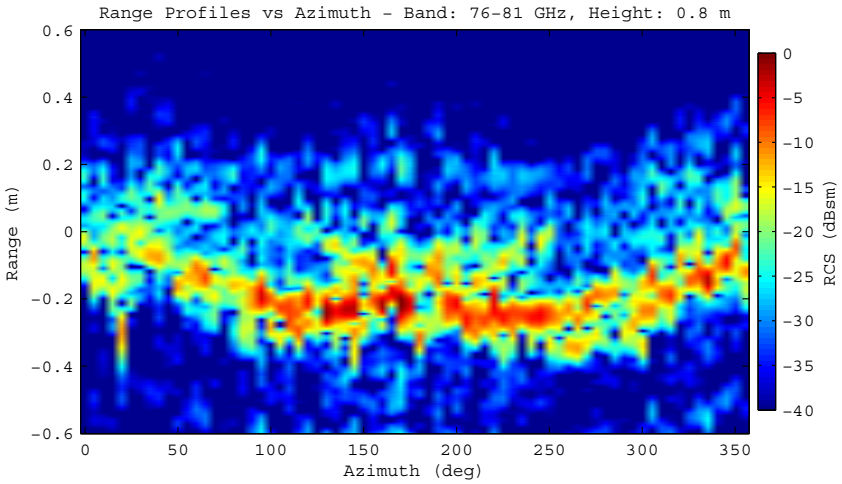

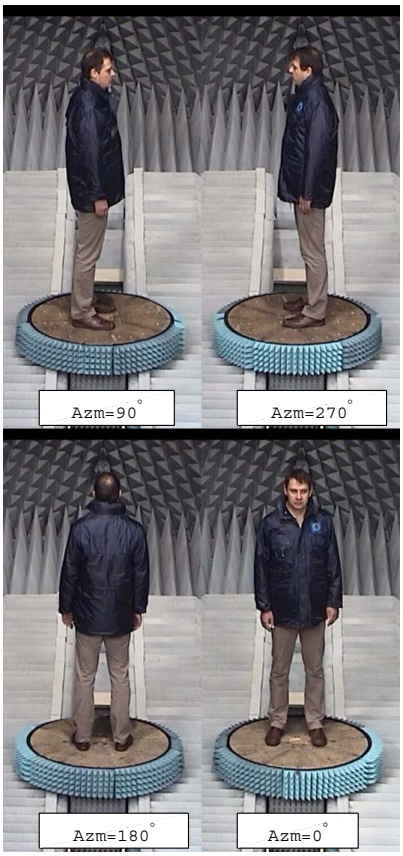

Adult#1 Winter Blue Coat

Frequency/Azimuth Average RCS (dBsm)

Band (GHz)	76-77	77-78	78-79	79-80	80-81	76-81
Height=0.8m	-5.69	-6.03	-5.15	-4.94	-5.43	-5.43

Figure D.14

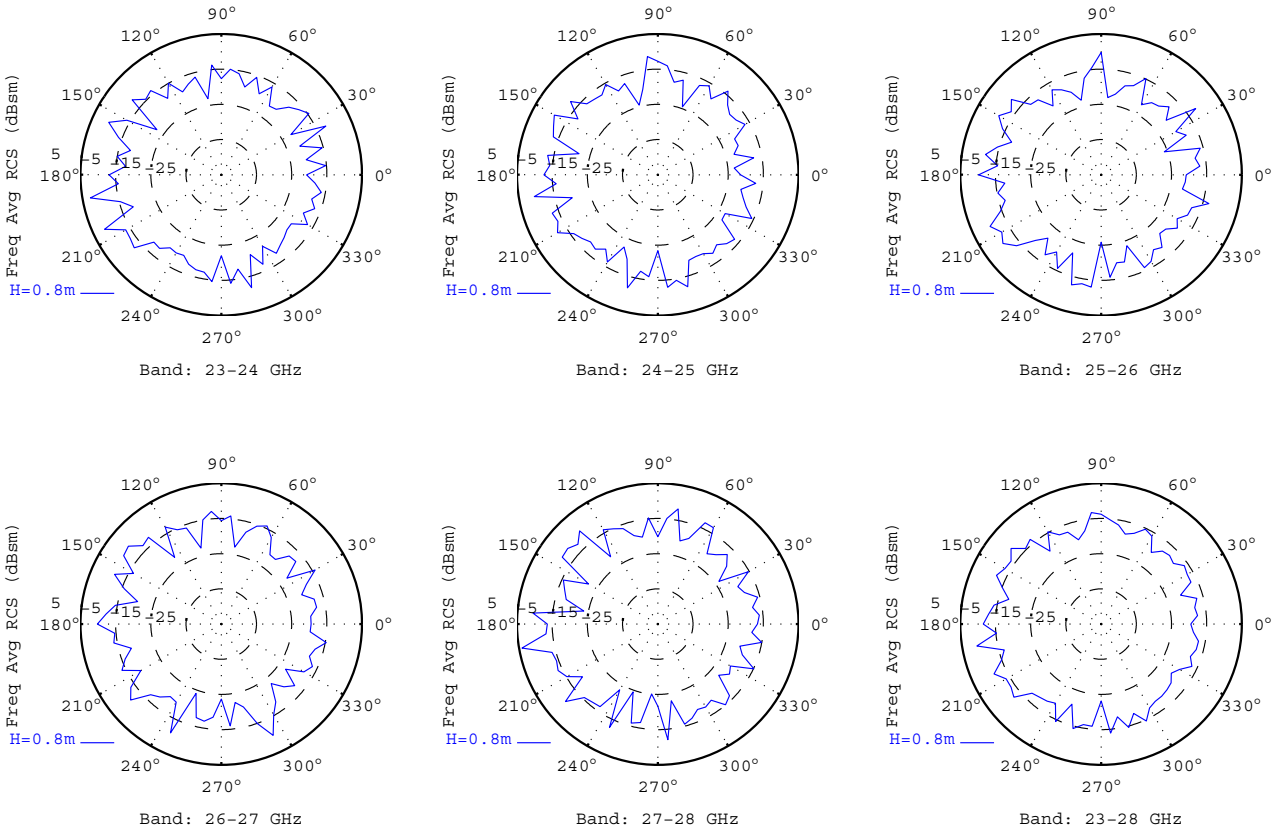

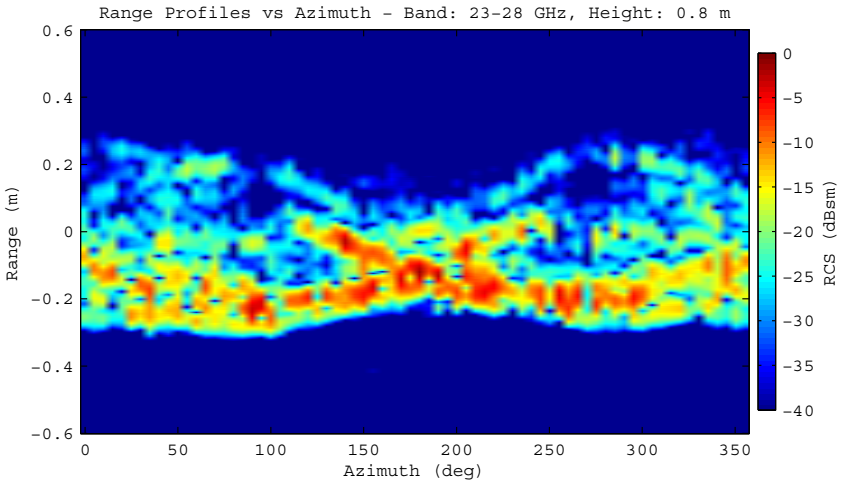

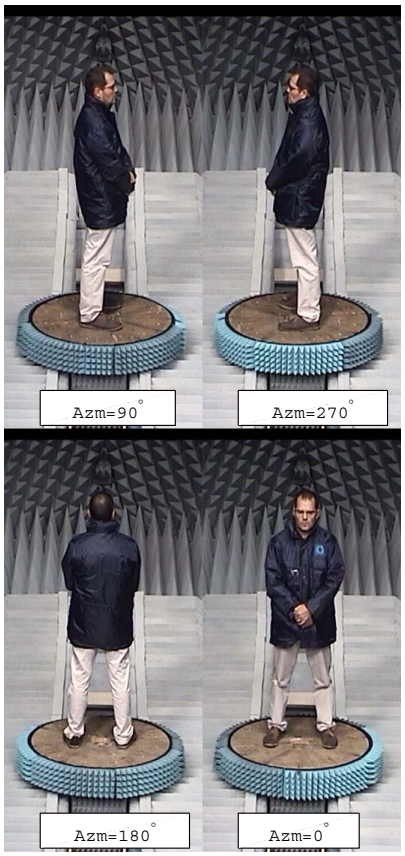

Adult#2 Winter Blue Coat

Frequency/Azimuth Average RCS (dBsm)

Band (GHz)	23-24	24-25	25-26	26-27	27-28	23-28
Height=0.8m	-5.53	-5.87	-5.85	-5.57	-5.18	-5.60

Figure D.15

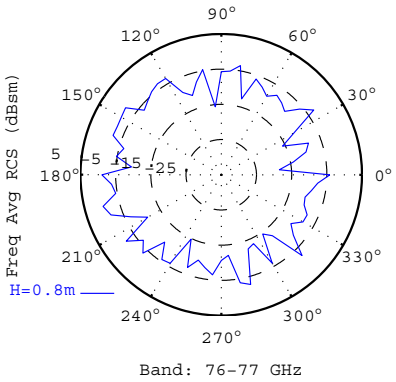

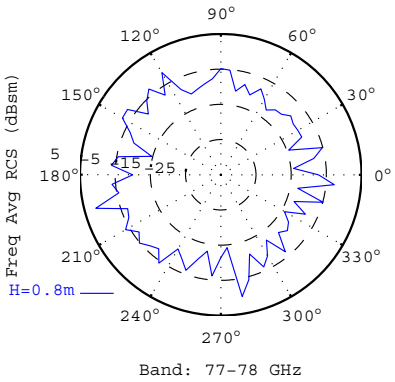

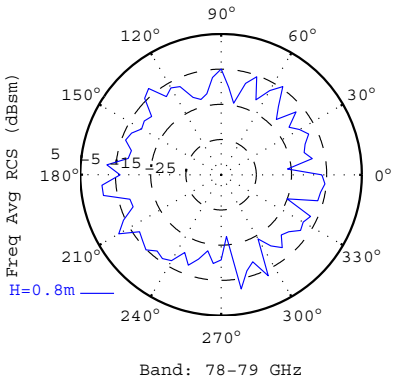

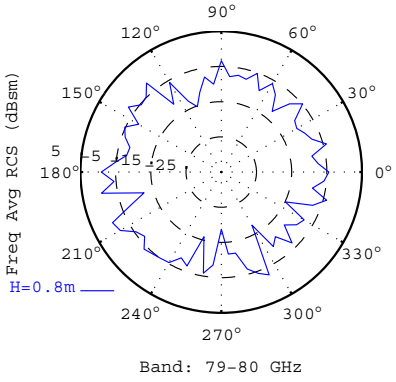

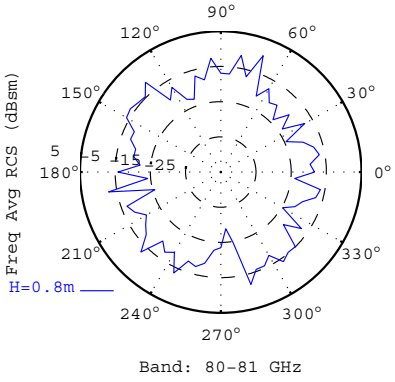

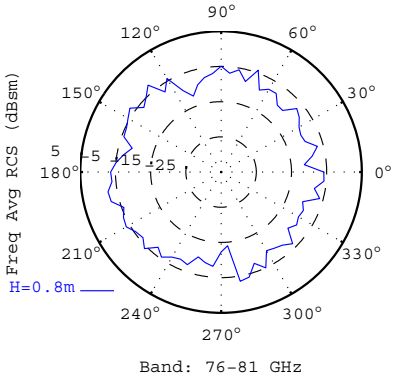

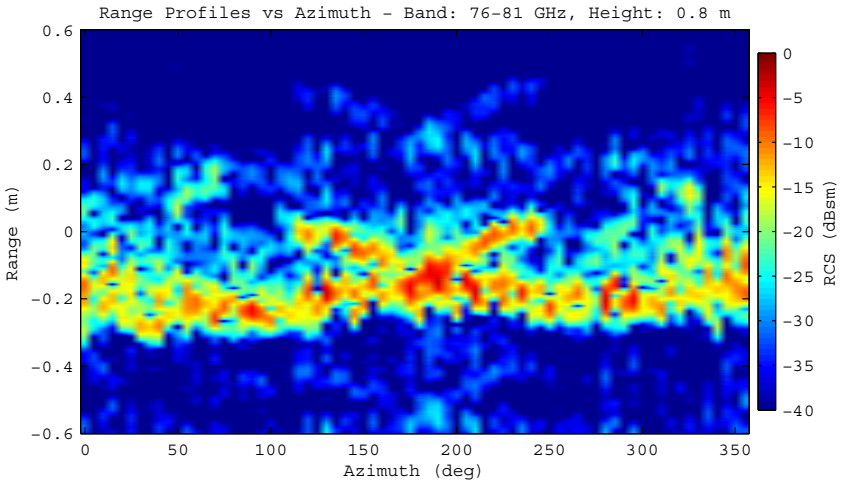

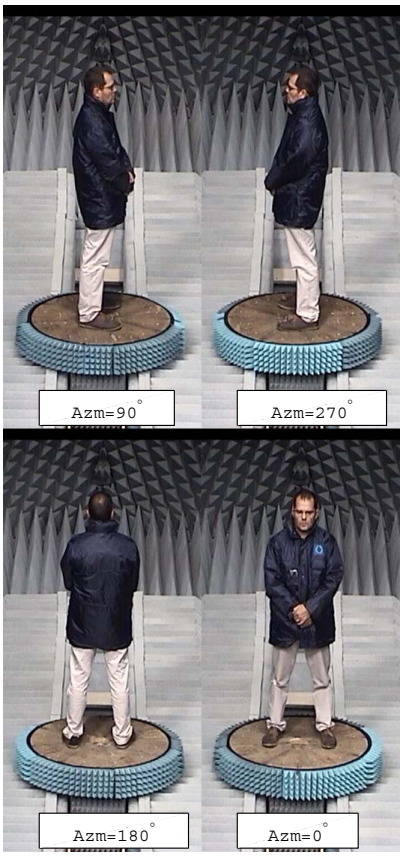

Adult#2 Winter Blue Coat

Frequency/Azimuth Average RCS (dBsm)

Band (GHz)	76-77	77-78	78-79	79-80	80-81	76-81
Height=0.8m	-5.90	-6.48	-6.86	-6.16	-6.80	-6.43

Figure D.16

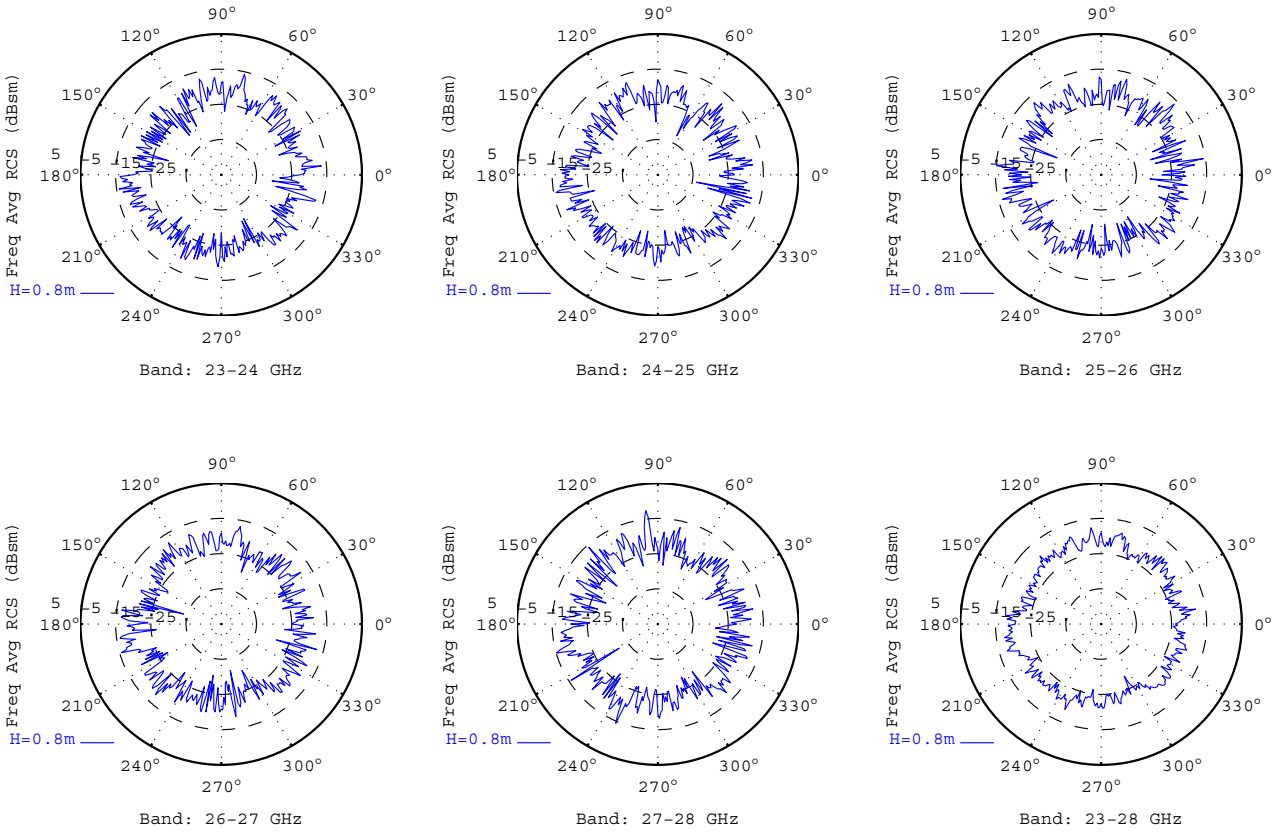

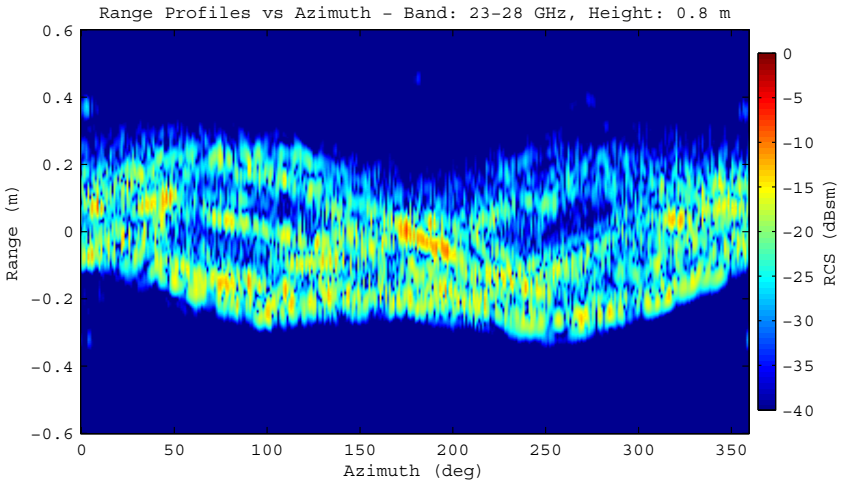

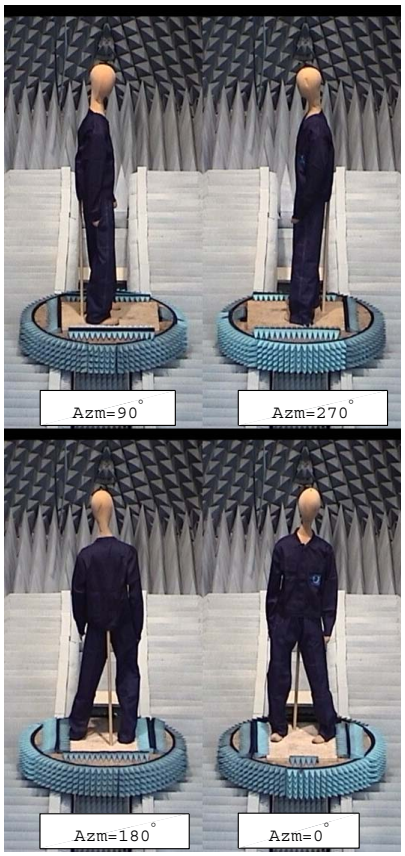

Dummy Type: KIT Dummy with Clothes

Frequency/Azimuth Average RCS (dBsm)

Band (GHz)	23-24	24-25	25-26	26-27	27-28	23-28
Height=0.8m	-11.60	-11.73	-11.67	-11.44	-11.19	-11.53

Figure D.17

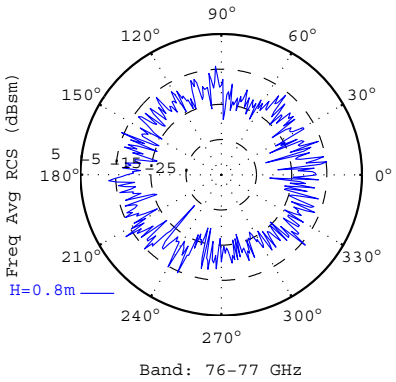

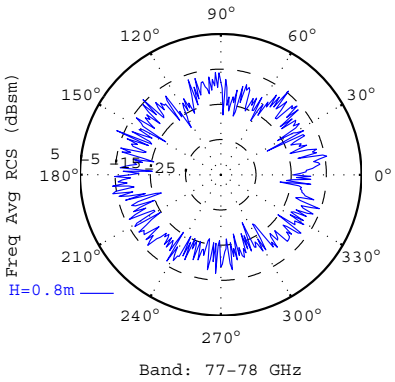

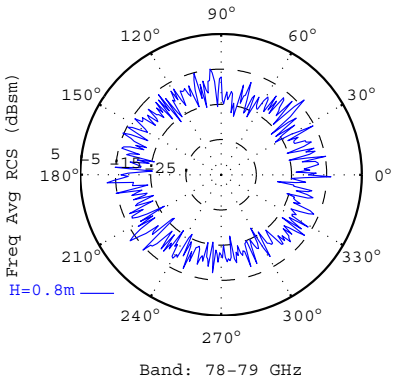

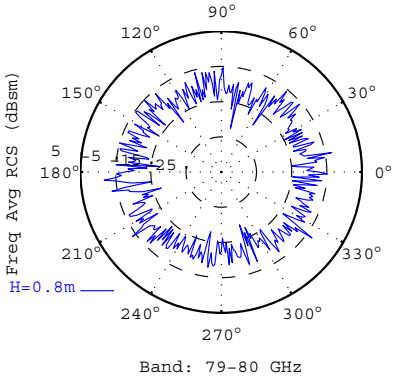

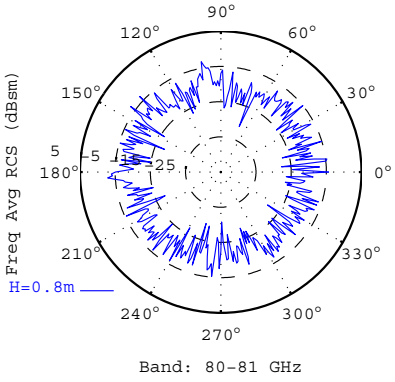

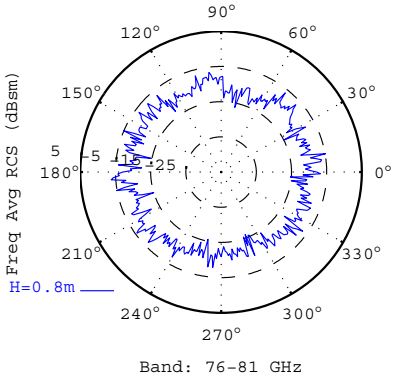

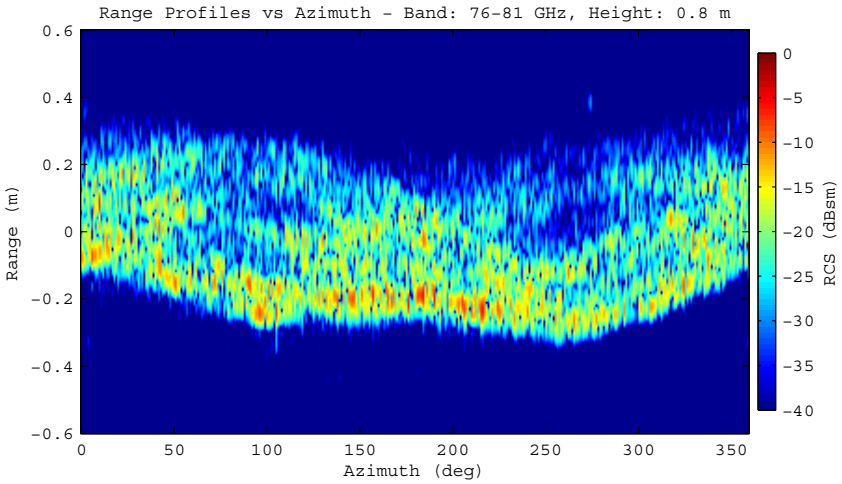

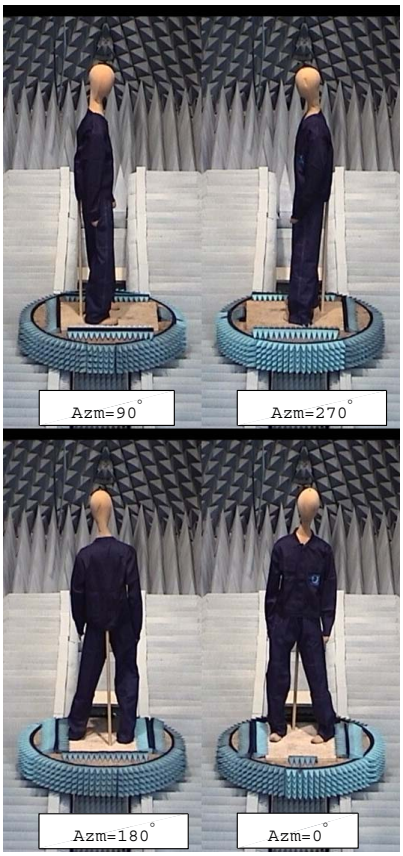

Dummy Type: KIT Dummy with Clothes

Frequency/Azimuth Average RCS (dBsm)

Band (GHz)	76-77	77-78	78-79	79-80	80-81	76-81
Height=0.8m	-9.93	-9.75	-9.64	-9.50	-9.35	-9.63

Figure D.18

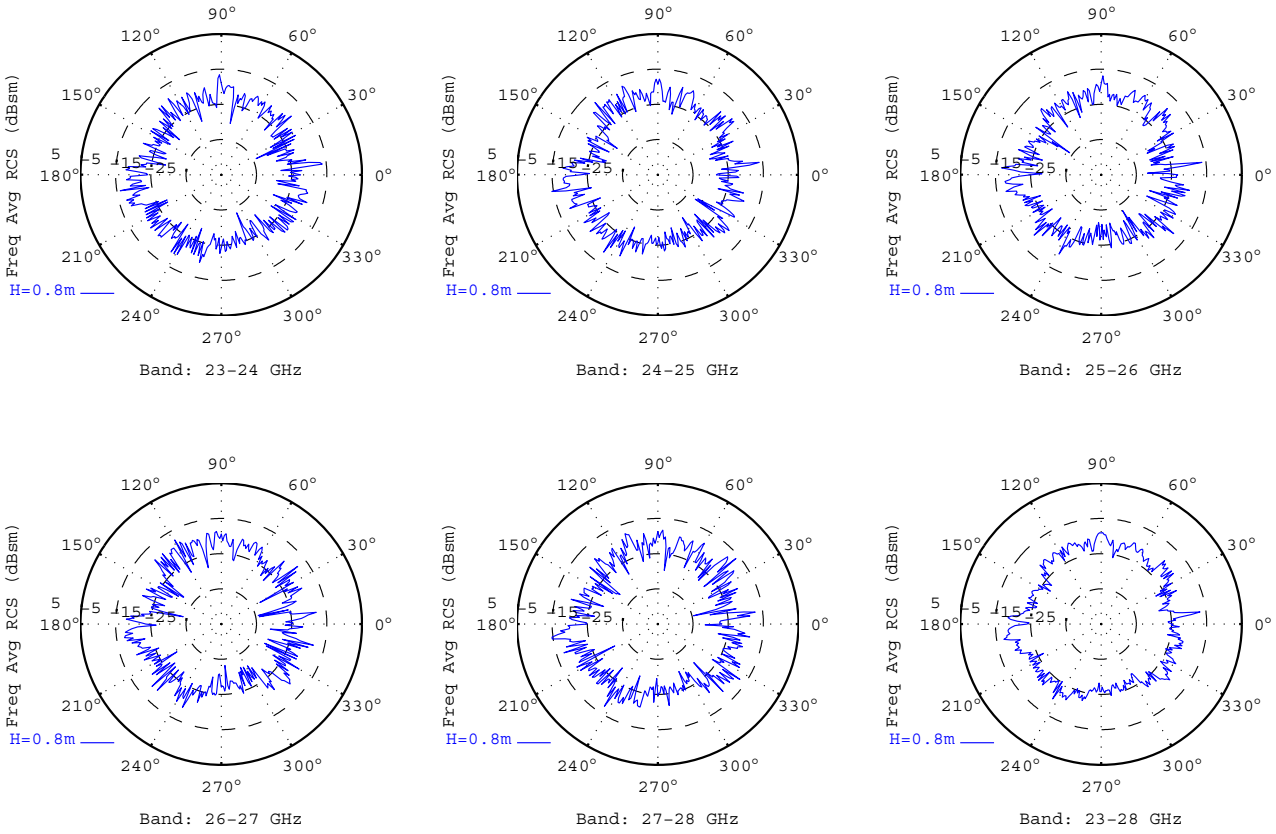

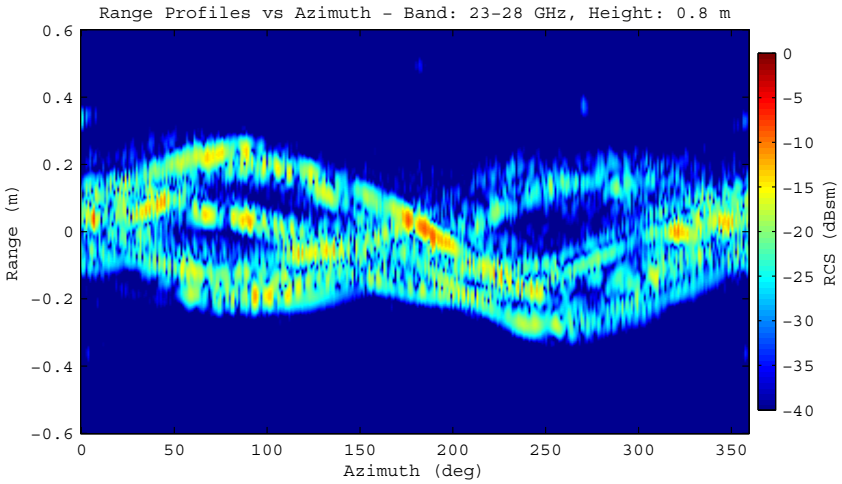

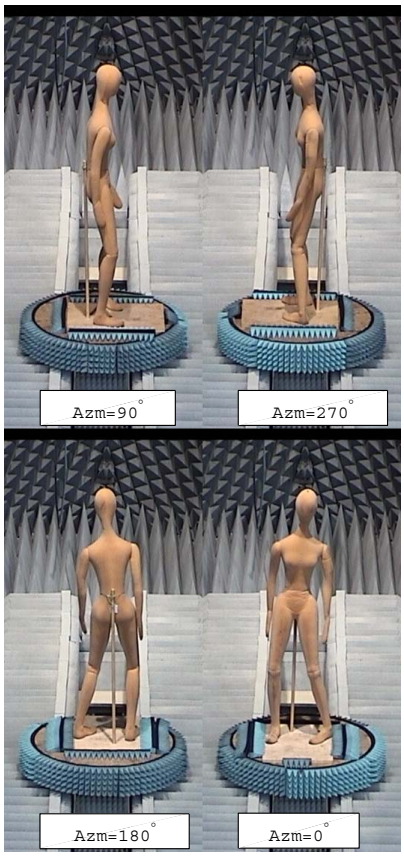

Dummy Type: KIT Dummy without Clothes

Frequency/Azimuth Average RCS (dBsm)

Band (GHz)	23-24	24-25	25-26	26-27	27-28	23-28
Height=0.8m	-12.56	-12.54	-12.96	-12.80	-12.07	-12.59

Figure D.19

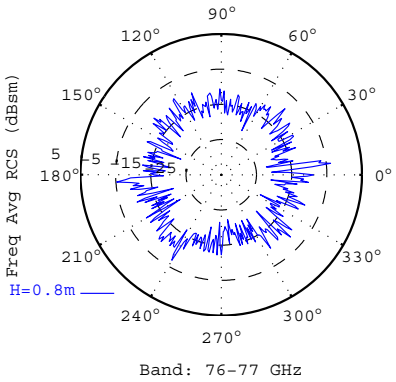

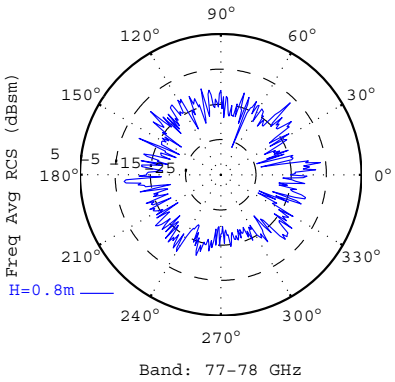

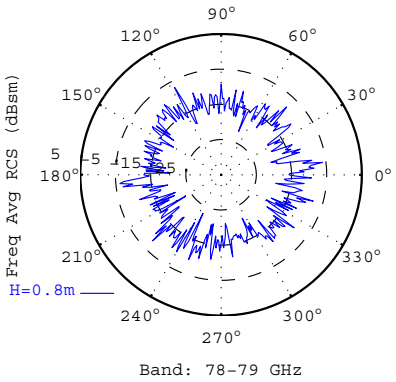

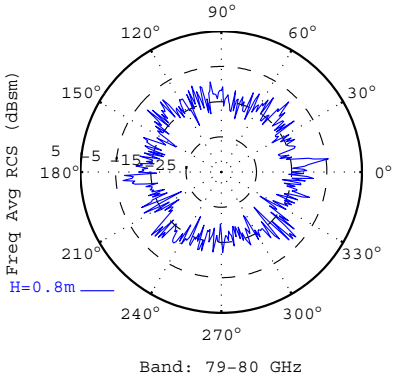

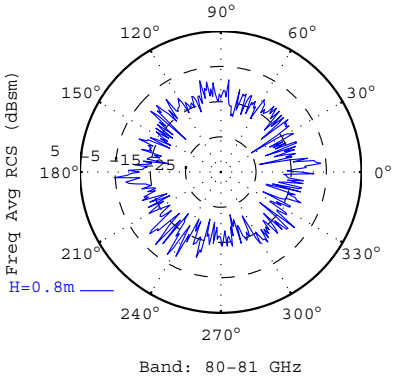

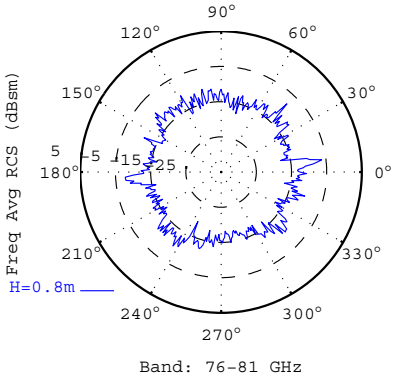

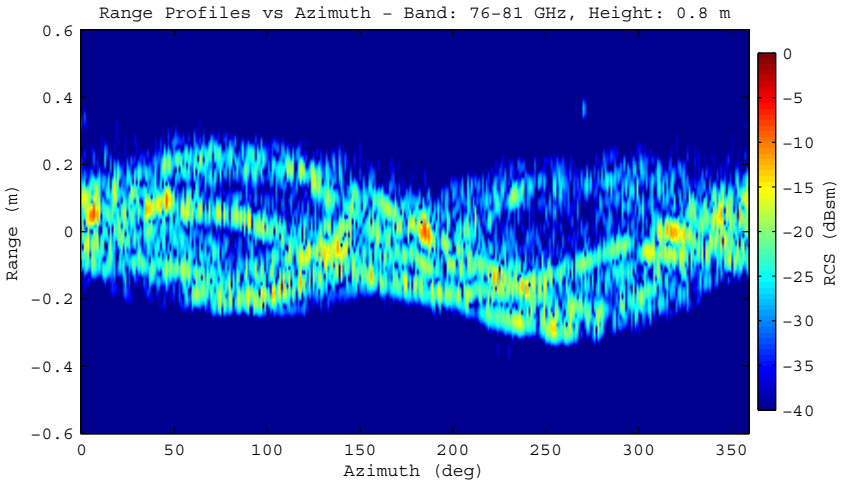

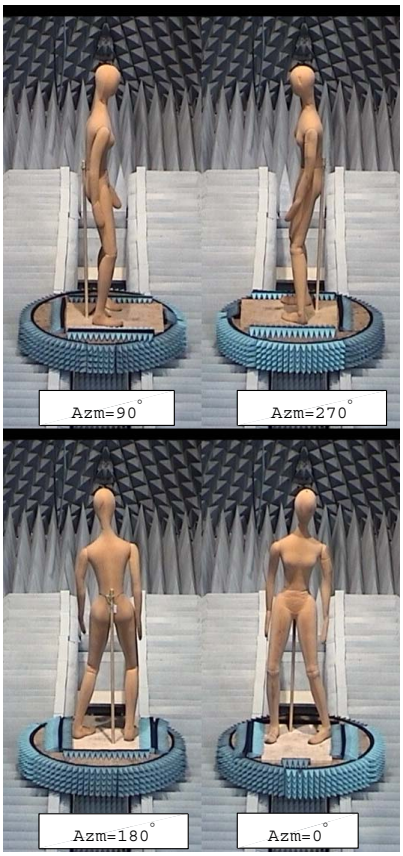

Dummy Type: KIT Dummy without Clothes

Frequency/Azimuth Average RCS (dBsm)

Band (GHz)	76-77	77-78	78-79	79-80	80-81	76-81
Height=0.8m	-13.55	-13.89	-13.53	-13.05	-13.13	-13.42

Figure D.20

Acknowledgements

The authors of this report are thankful to the partners of the ASPECSS and MOSARIM Projects for the support provided in this measurement campaign. In particular, we thank all those who provided the sample dummies that have been charecterized in the tests presented in this report.

We acknowledge the kind support of Messrs. Martin Kunert and Eugen Schubert, both from Robert Bosch GmbH, who assisted us with the planning and preparation of the measurement campaign.

We thank the support engineers from Agilent Technologies Italy, Messrs. Davide Beretta and Giancarlo De Chirico, who helped us with the installation of the PNA-X and its frequency extension for the RCS measurements in the E-band.

Special thanks for the support provided during the measurement campaign are also due to Messrs. Philippe Viaud, Marco Basso, Jorge Figueiredo-Morgado, and Martin Zürn, all in the Unit G06 of the Institute for the Protection and Security of the Citizen, EC Joint Research Centre.

References

[1] Final report of HEATCO: Developing Harmonised European Approaches for Transport Costing and Project Assessment [WWW], December 2006. European Commission FP6 Project.

[2] *Road Safety: Impact of New Technologies*. OECD Publishing, 2003.

[3] Towards a European road safety area: Policy orientations on road safety 2011-2020 (SEC(2010) 903) [PDF], July 2010. European Commission – Communication from the Commission to the European Parliament, the Council, the European Economic and Social Committee and the Committee of the Regions.

[4] Merrill I. Skolnik. *Radar Handbook, Third Edition*. McGraw-Hill, January 2008.

[5] M. Schneider. Automotive radar: Status and trends. In *Proceedings of the German Microwave Conference GeMIC 2005, Berlin, Germany*, pages 144–147, 2005.

[6] Vadim Issakov. *Microwave Circuits for 24 GHz Automotive Radar in Silicon-based Technologies*. Springer, August 2010.

[7] H.-L. Bloecher, A. Sailer, G. Rollmann, and J. Dickmann. 79 GHz UWB automotive short range radar: Spectrum allocation and technology trends. *Advances in Radio Science*, 7:61–65, 2009.

[8] J. Wenger. Automotive mm-wave radar: status and trends in system design and technology. In *Proc. IEE Colloquium Automotive Radar and Navigation Techniques (Ref. No. 1998/230)*, 1998.

[9] ECC Report 23: Compatibility of automotive collision warning short range radar operating at 24 GHz with FS, EESS and radio astronomy [PDF], May 2003.

[10] M. Younis, J. Maurer, J. Fortuny-Guasch, R. Schneider, W. Wiesbeck, and A. J. Gasiewski. Interference from 24-GHz automotive radars to passive microwave Earth remote sensing satellites. *IEEE Transactions on Geoscience and Remote Sensing*, 42(7):1387–1398, 2004.

[11] D16.1 Report on interference density increase by market penetration forecast, MOre Safety for All by Radar Interference Mitigation (MOSARIM) [WWW], September 2010. European Commission FP7 Project.

[12] Euro NCAP Autonomous Emergency Braking Fitment Results [WWW], 2012. European New Assessment Car Programme (Euro NCAP) Association.

[13] N. Yamada, Y. Tanaka, and K. Nishikawa. Radar cross section for pedestrian in 76 GHz band. In *Proc. European Microwave Conf*, volume 2, 2005.

[14] Federal Communications Commission 02–48A1: Revision of Part 15 of the Commission's Rules Regarding Ultra-Wideband Transmission Systems [PDF], February 2002.

[15] A. J. Sieber. The European Microwave Signature Laboratory. *EARSel Advances in Remote Sensing*, 2(1):195–204, January 1993.

[16] More Safety for All by Radar Interference Mitigation (MOSARIM) [WWW], January 2010. European Commission FP7 ICT Project.

[17] *Agilent Technologies N5256/7/8A Millimeter-Wave Modules Userś Guide [PDF]*.

[18] Commission Implementing Decision of 29 July 2011 amending Decision 2005/50/EC on the harmonization of the 24 GHz radio spectrum band for the time-limited by automotive short-range radar equipment in the Community (2011/485/EU) [PDF].

[19] Electromagnetic compatibility and Radio spectrum Matters (ERM); Short Range Devices; Road Transport and Traffic Telematics (RTTT); Radar equipment operating in the 76–77 GHz range; Part 1: Technical characteristics and test methods for radar equipment operating in the 76–77 GHz range (ETSI EN 301 091-1) [PDF].

[20] Electronic Communication Committee Decision of 19 March 2004 on the frequency band 77–81 GHz to be designated for the use of Automotive Short Range Radar (ECC/DEC/(04)03)) [PDF].

[21] Commission Decision of 8 July 2004 on the harmonisation of radio spectrum in the 79 GHz range for the use of automotive short-range radar equipment in the Community (2004/545/EC) [PDF].

[22] D. L. Mensa. Wideband radar cross section diagnostic measurements. *IEEE Transactions on Image Processing*, 33(3):206–214, September 1984.

[23] D. L. Mensa. *High Resolution Radar Cross Section Imaging*. Artech House, Norwood (MA), USA, 2nd edition, 1991.

[24] N. C. Currie. *Radar Reflectivity Measurement: Techniques and Applications*. Artech House, Norwood (MA), USA, 1989.

[25] Fawwaz T. Ulaby and Charles Elachi. *Radar Polarimetry for Geoscience Applications*. Artech House, Norwood (MA), USA, 1990.

[26] George T. Ruck, Donald E. Barrick, Clarence K. Kirchbaum, and William D. Stuart. *Radar Cross Section Handbook*, volume 1. Plenum Press, 1970.

[27] Assessment methodologies for forward looking Integrated Pedestrian and further extension to Cyclists Safety Systems (ASPECSS) [WWW], September 2011. European Commission FP7 ICT Project.

[28] C. E. Baum. The singularity expansion method. In Professor Leopold B. Felsen, editor, *Transient Electromagnetic Fields*, number 10 in Topics in Applied Physics, pages 129–179. Springer Berlin Heidelberg, January 1976.

[29] C.E. Baum, E.J. Rothwell, K.-M. Chen, and D.P. Nyquist. The singularity expansion method and its application to target identification. *Proceedings of the IEEE*, 79(10):1481 –1492, October 1991.

[30] J. Fortuny. *Efficient Algorithms for three-Dimensional Near-Field Synthetic Aperture Radar Imaging*. PhD thesis, Karlsruhe University, Karlsruhe, Germany [PDF], May 2001.

[31] D. L. Mensa, G. Heidbreder, and G. Wade. Aperture synthesis by object rotation in coherent imaging. *IEEE Transactions on Nuclear Science*, 27(2):989–998, April 1980.

[32] Victor C. Chen and Hao Ling. *Time-Frequency Transforms for Radar Imaging and Signal Analysis*. Artech House, 2002.

[33] Graeme E. Smith, Fauzia Ahmad, and Moeness G. Amin. Micro-doppler processing for ultra-wideband radar data. In *Proc. SPIE 8361, Radar Sensor Technology XVI, 83610L*, May 2012.

[34] Bijan G. Mobasseri and Moeness G. Amin. A time-frequency classifier for human gait recognition. In *Proc. SPIE 7306, Optics and Photonics in Global Homeland Security V and Biometric Technology for Human Identification VI, 730628*, May 2009.

[35] A. Ghaleb, L. Vignaud, and J.M. Nicolas. Micro-doppler analysis of wheels and pedestrians in ISAR imaging. *IET Signal Processing*, 2(3):301, 2008.

[36] Sandy Lovie. Box Plots. In *Encyclopedia of Statistics in Behavioral Science*. John Wiley & Sons, Ltd, 2005.

[37] F. J. Harris. On the use of windows for harmonic analysis with the discrete Fourier transform. *Proceedings of the IEEE*, 66(1):172–204, January 1978.

[38] L. Rabiner, R. Schafer, and C. Rader. The Chirp-Z transform algorithm. *IEEE Transactions on Audio and Electroacoustics*, 17(2):86–92, 1969.

[39] Jessica Rose and James G. Gamble, editors. *Human Walking*. Lippincott Williams & Wilkins, third edition, December 2005.

[40] J. A. Stratton. *Electromagnetic Theory*. McGraw-Hill, New York, USA, 1941.

[41] Constantine Balanis. *Advanced Engineering Electromagnetics*. Wiley, New York, USA, 1989.

[42] H. Weil, M. L. Barasch, and T. A. Kaplan. Studies in radar cross sections - X. Scattering of electromagnetic waves by spheres. Technical report, University of Michigan, Dept. of Electrical Engineering, 1956.

[43] M. Abramowitz and I. A. Stegun. *Handbook of Mathematical Functions*. Dover Publications Inc., New York, USA, 1970.

European Commission
EUR 25762 EN – Joint Research Centre – Institute for the Protection and Security of the Citizen

Title: **Radar Cross Section Measurements of Pedestrian Dummies and Humans in the 24/77 GHz Frequency Bands**

Authors: Joaquim Fortuny-Guasch, Jean-Marc Chareau

Luxembourg: Publications Office of the European Union

2013 – 109 pp. – 21.0 x 29.7 cm

EUR – Scientific and Technical Research series – ISSN 1931-9424 (online), ISSN 1018-5593 (print)

ISBN 978-92-79-28230-0
doi:10.2788/80844

Abstract

Road safety has become a major societal issue that should not be ignored. At present, a wide range of new technologies, including intelligent speed adaptation and collision avoidance systems, are being introduced to improve road safety levels and reduce these casualties. Among the various types of collision avoidance systems, automotive short-range radars (SRRs) are those most widely deployed. A recent Communication of the European Commission (i.e., SEC(2010) 903) has stated that a wide deployment of SRR systems could help to reach the EU's policy goal of halving the number of deaths on the road. In this context, it is very important to make sure that the SRR signatures of pedestrian dummies match those of humans with a high degree of accuracy. This report summarizes the results of an extensive series of radar cross section (RCS) laboratory measurements on pedestrian dummies and humans completed in August 2012 at the European Microwave Signature Laboratory of the EC Joint Research Centre. This measurement campaign has allowed the establishment of a reference library with the RCS signatures of pedestrian dummies and humans in the 24 GHz and 77 GHz bands, which are those currently allocated for automotive SRR systems. Results show for the first time that the observed global frequency/azimuth RCS averages in the two frequency bands are very close to each other. A significant impact of the pedestrian height on the observed RCS, particularly at 77 GHz, has also been noted. A first qualitative comparison of the RCS signatures between dummies and humans was also completed. and showed that the RCS averages of the available dummies are slightly below those of the humans. Finally, following a dedicated series of measurements, it has been observed that the impact of the clothing on the measured signatures is minimal except for those cases where some very thick clothes were worn.

LB-NA-25762-EN-N

As the Commission's in-house science service, the Joint Research Centre's mission is to provide EU policies with independent, evidence-based scientific and technical support throughout the whole policy cycle.

Working in close cooperation with policy Directorates-General, the JRC addresses key societal challenges while stimulating innovation through developing new standards, methods and tools, and sharing and transferring its know-how to the Member States and international community.

Key policy areas include: environment and climate change; energy and transport; agriculture and food security; health and consumer protection; information society and digital agenda; safety and security including nuclear; all supported through a cross-cutting and multi-disciplinary approach.

Publications Office

ISBN 978-92-79-28230-0